ROMA TRE
UNIVERSITÀ DEGLI STUDI

Scuola Dottorale in Ingegneria
Sezione di Ingegneria Meccanica e Industriale

XXVI Ciclo Dottorale

Higher Order Isogeometric BEM
for
High Accuracy Simulations in Acoustics

Dottorando:
Vincenzo Marchese

_____

Tutor:
Prof.Umberto Iemma

_____

Coordinatore:
Prof.Edoardo Bemporad

_____

Acknowledgments

> H: What are you doing?
> C: Being cool.
> H: You look more like you're bored.
> C: The world bores you when you're cool.

C and H

A PhD work is like a three–year long journey between theories that do not fit, simulations that do not work and results that do not match with the expected. During the journey one also encounters good news, everything falls into place and the many struggles resolve in finding the "perfect fit" with what one is expecting from his work.

This journey, for me, has begun some years ago, with my graduation. Back then, I thought I could stop travelling and try myself in the "outside" world, finding a job and settling for a less challenging but equally noble way of spending my days. My supervisor at that time looked me in the eyes and said: "You will get bored". I dismissed that remark with the presumption that only a just graduated young man can have.

In the years between my graduation and these last three years I have been bouncing between my day–to–day job and the many collaborations with the university and I have to say that while my work as an IT professional has put bread on my table, my "academic" work has fed vitamins to my mind and has satisfied the needs on the topmost layers of Maslov's pyramid.

So, part of my thanks after these many years (not just these latest three) goes to Prof.Luigi Morino because he was right: in the "outside" world, I got bored, after all.

The other, most sincere and heartfelt huge part of my thanks goes to my PhD supervisor, Prof.Umberto Iemma, who shared with me these years of work and laughs, years in which we managed, in my humble opinion, to accomplish many good things from a scientifically point of view and in which, most importantly, we developed a profound and long lasting friendship.

To M. and M.

Contents

Chapter 1

Introduction

C: I'm a genius, but I'm a misunderstood genius.
H: What's misunderstood about you?
C: Nobody thinks I'm a genius.

C and H

1.1 The Boundary Element Method

The Boundary Element Method is an established standard tool for solving many type of Boundary Value Problems (BVP), e.g. inviscid and viscous incompressible flow around solid bodies in subsonic and transonic regime, structural elasticity problems, heat conduction and acoustic scattering. The main advantages in using the BEM methodology are in the reduction of the dimensionality of the problem and in the ease of implementation on a cluster of parallel computing nodes.

The usual approach in BEM involves the partitioning of the domain into N_{el} finite elements, where the dependent and independent variables are approximated using suitable local basis functions. In a 0th order approximation, the variables are assumed as piecewise constants on the elements. Many 0th order implementations, both commercial and open source, of the solution of the acoustic problem with a BEM methodology can be found, among which: AcouSTO[23], released under the LGPL license and BEM acoustics [24], a Matlab toolbox released under the GPL license.

2

Low order approximations however, while easy to implement, has a low rate of convergence and an accuracy $O(h)$ where h is the size of the element. Although this approach is usually convenient with respect to the *field* methods, such as Finite Volumes Method (FV), Finite Differences Method (FD) or Finite Element Method (FE), especially when the far–field analysis is required (*i.e.*, aeroacoustics) in some specific applications the number of boundary elements required to capture a specific feature of the phenomenon may become extremely high.

This is the case, for example, of acoustic propagation and scattering problems, where the wave length of the perturbation at high frequencies can be orders of magnitude smaller than the characteristic length of the domain of interest, thus requiring a huge amount of boundary panels to correctly reproduce the scattering and interference effects.

Different modifications to the BEM method have been developed to reduce the computational effort due to the larger number of degrees of freedom. Although some of these are quite effective in low to medium accuracy problems (*i.e.*, the Fast Multipole Method [29]) it has been shown [10] that, for high accuracy applications, the approximations made in the algorithm could introduce artefacts in the solution that could lead to wrong analysis and design.

One of the possible approaches to deal with high demanding problems without losing in precision is the improvement of the accuracy of the local representation of the variables using higher–order functions. Among the published works on the subject, it is worth mentioning the use of third order polynomials based on Overhauser [13, 2] or Hermite splines [6, 11] elements, recently coupled with Coons patches [8]. The adoption of the above mentioned techniques increases the number of degrees–of–freedom. The classic cubic Hermite interpolation, for instance, implies the knowledge of the nodal values and of the derivative of the interpolated function. In a 3D interpolation, one must also take into account the nodal mixed derivatives along the curvilinear coordinates ξ and η on the surface. The higher accuracy of the solution however, allows to decrease the number of elements N_{el} required to capture the solution and a convenient trade off between number of degrees–of–freedom and number of elements can be found. For orders higher than

the third, the knowledge of higher derivatives in the discretisation nodes is needed, hence making the representation on a single panel being dependent on the nodal values on the adjacent panels due to the evaluation with a finite difference scheme of the aforesaid derivatives.

1.2 High Accuracy applications: Metamaterials

Recently, thanks to advanced fabrication techniques and increased performances in computational frameworks, a great attention has been directed to the so–called "metamaterials", term coined for the first time by Rodger Walser[9], who gave the following definition:

> *"macroscopic composites having a manmade, three–dimensional, periodic cellular architecture designed to produce an optimised combination, not available in nature, of two or more responses to specific excitation."*

A metamaterial is hence a structure expected to show one of more property "different" than those of its "constituents".

In the present work, we focus our attention on phononic crystals that are acoustic metamaterials designed to direct the sound waves by exploiting the 1D, 2D or 3D periodic (Figure 1.1) variations of the acoustic properties of the used material.
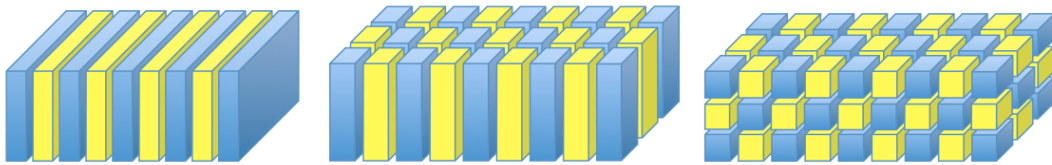

Figure 1.1: Periodic structures, from left to right: 1D, 2D and 3D

The peculiar property of phononic crystals is the exhibition of an acoustic band gap *i.e.*, a zone in the transmission spectra where the propagation of acoustic waves is forbidden. This is a phenomenon well known in physics, for instance in

semiconductors where electrons can occupy only certain specific energy bands or in photonics crystals that allow light only in certain frequency ranges thanks to the variation in the refractive index of the material. The same principle is applied in phononic crystal where the band gap is obtained by using a material with a periodic change of density or elasticity that cause periodic changes in the speed of sound or by spatial periodicity of the domain geometry. When an acoustic wave passes through these materials, constructive interference leads to the creation of a band gap while destructive interference to the creation of propagation bands. To allow for constructive interference to take place the material must be designed such as the path differences between the interfering waves is a multiple of their wavelength λ. This is obtained by designing the material with a lattice parameter a comparable with the wavelength λ. By changing the size of the unit periodic cells, that is by changing a, we can control the frequency of the band gap. The band gap width is controlled by the ratio of the densities and of the sound speed velocities in the material.

The position and width of the band gap also depends on the direction of the impinging wave. Some crystals form band gaps for waves propagating in any directions, others only for waves with certain angle of incidence.

An example of the sonic properties of phononic crystals is the kinematic sculpture of Eusebio Sempere, consisting of a periodic array of hollow stainless-steel cylinders, each 2.9 cm in diameter, arranged on a square 10×10 cm lattice, which exhibits a strong attenuation at $f = 1670$ Hz.

The most obvious application of such structures is sound manipulation in terms of perfect mirroring of waves or acoustic wave-guides forcing the acoustic wave in a specific area of the crystal and also having it go around sharp corners (Figure 5.2 and 5.3). In order to be effective in the human audible regime (20Hz–20kHz), the dimensions of a phononic structure are suitable for architectural purposes but impractical for portable uses (*i.e.*, headphones and speakers). This is not the case in the ultrasonic regime where phononic crystals can be much smaller (from centimetres to fraction of millimiters).

In particular, for ultrasonic waves, some studies [27, 28] have shown as appropriately designed structures can act as "perfect acoustic lenses" *i.e.*, lenses that overcome the diffraction limit of the material and allow to focus the acoustic waves on spots shorter than the wavelength of the impinging wave itself, representing a huge breakthrough for ultrasound techniques.

Moving further in the acoustic spectrum and reaching the hypersonic regime ($\lambda < 10\mu$m), periodic structures can have applications in light emitting devices, where the emission is due to the interaction between electrons and high–frequency phonons, and in thermal management where the thermal conductivity of metamaterials is mainly due to the phonons.

The simulation of these kind of structures, however, requires a high level of accuracy due to the complex interactions between the bodies in the periodic system and also, in some cases, to the high frequencies involved. The adoption of a boundary element method in the simulation allows to avoid the discretisation of the domain. The 0th BEM algorithm could be applied here but the number of structures and the frequencies involved make the number of elements and hence the required computational resources involved rapidly grow. As mentioned before and as shown by Rokhlin [29], the adoption of an approximated algorithm can reduce the number of the degrees of freedom but the introduced artefacts in the solution can completely disrupt the simulation due to the high level of accuracy required. The adoption of a not–approximated methodology of an order higher than 0th is hence recommended.

1.3 Present work

In the present work we developed five different not approximated BEM higher–order approaches for the solution of the 2D and 3D acoustic problem, validating them against analytical solution, where available, and performing a convergence analysis. The different approaches explored in this work are:

- 2D Hermite (*classic approach*)

- 2D Hermite Dual

- 3D Hermite Coons

- 3D Hermite Coons Dual (*preliminary implementation*)

- 2D Nurbs

We explored algorithms based mostly on Hermite splines. The presence of the nodal derivatives in the representation of the variables, has been taken into account both with a "classic approach", where those derivatives are expressed with a finite differences scheme in terms of the nodal values and with a so called "dual approach" where the same derivatives are considered as unknown of the problem and the linear system is completed by the tangential gradient of the integral equation.

The Hermite based higher order representations, also coupled with Coons patches to avoid the introduction of the mixed derivatives, although achieving a higher rate of convergence than $O(h)$, are limited to a single order.

In order to overcome the *single*–order limitation of the Hermite based BEM methods we also explored an approach based on Non Uniform Rational Basis–Splines (NURBS). By using a global representation of the variables based on NURBS, the order of the basis functions can be improved at runtime when needed by the specific application at hand. This is a consequence of the iterative definition of the NURBS, which makes possible the increase of the NURBS degree simply by changing an input parameter. The use of the NURBS for the representation of curves and surfaces is a common technique in the CAD community for

the modeling of complex geometries with strict requirements of smoothness and continuity between patches[20, 18]. Their use in the numerical solution of BIE is not new, although relatively recent. NURBS have been used to develop boundary element solutions of integral equations in elastostatics[21], in radiation and diffraction problems[14], and in potential aerodynamics[19]. As already mentioned, the peculiarity of this approach is in the use of the NURBS for the development of a global isogeometric approach aimed at the meshless numerical solution of the BVP. The control points used for the representation of the dependent variables are obtained through the h-refinement of the optimal NURBS representation of the geometry.

In the following chapters we will outline the underlying theory for the acoustic problem and for the BEM methodology, we will illustrate the above said approaches in detail and in Chapter 5 we will show how the high order methods described in this work are an effective tool to the simulation of these kind of phenomena.

Chapter 2

The Acoustic Problem

> This one's tricky. You have to use imaginary numbers, like eleventeen ...
>
> C and H

Under the assumptions of a homogenous and quiescent propagation medium, with adiabatic characteristics and with small perturbations of pressure p and density ρ_0, the acoustic wave equation reads:

$$\Delta p(\mathbf{x}, t) - \frac{1}{c_0^2} \frac{\partial^2}{\partial t^2} p(\mathbf{x}, t) = -q(\mathbf{x}, t) \tag{2.1}$$

being c_0 the speed of sound in the reference conditions and $q(\mathbf{x}, t)$ the acoustic sources. Applying a Laplace transformation we can write Eq.(2.1) in the frequency domain as:

$$\nabla^2 \tilde{p}(\mathbf{x}) - \kappa^2 \tilde{p}(\mathbf{x}) = -\tilde{q}(\mathbf{x}) \tag{2.2}$$

where the $\tilde{\bullet}$ indicates Laplace transformation and:

$$
\begin{aligned}
p(\mathbf{x}) & & \text{acoustic pressure,} \\
\omega &= 2\pi f & \text{angular frequency,} \\
f & & \text{frequency,} \\
s &= \alpha + j\,\omega & \text{Laplace variable,} \\
\kappa &= s/c_0 & \text{complex wave number.}
\end{aligned}
\tag{2.3}
$$

Eq.(2.2) can be also written, using the linearized Bernouilli's theorem, in terms of the velocity potential function φ, in the Laplace domain, to yield

$$\nabla^2 \tilde{\varphi}(\mathbf{x}) - \kappa^2 \tilde{\varphi}(\mathbf{x}) = 0, \qquad \text{for } \mathbf{x} \in \mathcal{V} \tag{2.4}$$

where the $\tilde{\bullet}$ indicates Laplace transformation and $\tilde{q}$ represents the acoustics sources present in the field.

Considering the fundamental solutions of the wave equation:

$$G(\mathbf{x}, \mathbf{y}, s) = \frac{1}{4} i H_2^0(kr) \qquad \text{for the 2D case} \tag{2.5}$$

$$G(\mathbf{x}, \mathbf{y}, s) = -\frac{e^{-s\theta}}{4\pi r} = G_0 e^{-s\theta} \quad \text{for the 3D case} \tag{2.6}$$

in which:

$$r = \|\mathbf{x} - \mathbf{y}\| \quad \text{norm of the distance,}$$
$$H_2^0(x) \qquad\qquad \text{Hankel function of the second kind,}$$
$$\theta = \frac{r}{c_0} \qquad\qquad \text{acoustic delay.} \tag{2.7}$$

and applying the Gauss theorem we arrive at the well known boundary integral formulation for the velocity potential:

$$E(\mathbf{y}) \tilde{\varphi}(\mathbf{y}) = \oint_{\mathcal{S}} \left(G \frac{\partial \tilde{\varphi}}{\partial n} - \tilde{\varphi} \frac{\partial G}{\partial n} \right) d\mathcal{S}(\mathbf{x}). \tag{2.8}$$

where the domain function $E(\mathbf{y})$ is

$$E(\mathbf{y}) = \begin{cases} 1 & \text{if } \mathbf{y} \in \mathcal{V}, \\ 1/2 & \text{if } \mathbf{y} \in \partial\mathcal{V}, \\ 0 & \text{if } \mathbf{y} \notin \mathcal{V}, \end{cases} \tag{2.9}$$

and $\mathcal{S} = \partial\mathcal{V}$ for internal problems, and $\mathcal{S} = \partial\mathcal{V} \backslash \mathcal{S}_\infty$ for external problems. Eq.(2.8) is the familiar KHIE:

$$E(\mathbf{y}) \tilde{\varphi}(\mathbf{y}) = \oint_{\mathcal{S}} \left(G \frac{\partial \tilde{\varphi}}{\partial n} - \tilde{\varphi} \frac{\partial G}{\partial n} \right) d\mathcal{S} \qquad\qquad \text{in 2D}$$

$$E(\mathbf{y}) \tilde{\varphi}(\mathbf{y}) = \oint_{\mathcal{S}} \left(G_0 \frac{\partial \tilde{\varphi}}{\partial n} - \tilde{\varphi} \frac{\partial G_0}{\partial n} + s\tilde{\varphi} G_0 \frac{\partial \theta}{\partial n} \right) e^{-s\theta} d\mathcal{S} \text{ in 3D.} \tag{2.10}$$

Chapter 3

BEM for Acoustics

> I propose we leave math to the machines and go play outside.
>
> C and H

The KHIE (2.10) is numerically solved through a Boundary Element Method (BEM). The boundary of the domain is partitioned into non-overlapping N_{el} panels, and we assume both geometrical and physical quantities to be represented by a linear combinations of n basis functions of order p, $N_{a,p}(\xi)$ having as coefficients the values $\tilde{f}_a$ of the function f in the nodal points of the discretization. This representation can be written, as:

$$f(\xi) = \sum_{a=1}^{n} N_{a,p}(\xi)\tilde{f}_a \tag{3.1}$$

Applying Eq.(3.1) to Eq.(2.10), and taking into account the discretization, we have[1]:

$$
\begin{aligned}
E(\mathbf{y})\,\varphi(\mathbf{y}) \;=\; & \sum_{a=1}^{n} \hat{\chi}_a \sum_{i=1}^{N_e} \int_{\mathcal{S}_i} G(\hat{\xi},\mathbf{y}) N_{a,p}(\hat{\xi}) J(\hat{\xi}) d\xi \\
& - \sum_{a=1}^{n} \hat{\varphi}_a \sum_{i=1}^{N_e} \int_{\mathcal{S}_i} \frac{\partial G(\hat{\xi},\mathbf{y})}{\partial n} N_{a,p}(\hat{\xi}) J(\hat{\xi}) d\xi
\end{aligned}
\tag{3.2}
$$

---

[1] the following treatment is written for the $2D$ case, the $3D$ formulation is similar with the addition of the coefficients due to the $\frac{\partial \theta}{\partial n}$ term

In which $J(\hat{\xi})$ is the jacobian of the transformation to an appropriate local curvilinear coordinate $\hat{\xi}$ defined on $\mathcal{S}_i$.

Eq.(3.2) can be written, collocating in the nodal points, in matrix form as:

$$\mathbf{E}\Phi = \mathbf{B}\Psi - \mathbf{C}\hat{\Phi} \qquad (3.3)$$

in which matrix $\mathbf{E} = 1/2\,\mathbf{I}$ and the elements of matrices $\mathbf{B}$ and $\mathbf{C}$ are:

$$
\begin{aligned}
B_{ij} &= \int_{\mathcal{S}_i} G(\hat{\xi},\mathbf{y}_j) N_{a,p}(\hat{\xi}) J(\hat{\xi}) d\xi \\
C_{ij} &= \int_{\mathcal{S}_i} \frac{\partial G(\hat{\xi},\mathbf{y}_j)}{\partial n} N_{a,p}(\hat{\xi}) J(\hat{\xi}) d\xi
\end{aligned}
\qquad (3.4)
$$

in which $\hat{\xi} \in [-1, 1]$.

Equation (3.3) can't be solved as a straightforward linear system because the coefficients of the linear combination (3.1), $\hat{\varphi}_a$ are not, generally speaking, the values of φ in the nodal points. If we can find a set of parameters ξ'_k such as:

$$\varphi(\xi'_k) = \sum_{a=1}^{n} N_{a,p}(\xi'_k) \hat{\varphi}_a \qquad (3.5)$$

in the nodal points of the discretisations, we can apply the representation (3.5) to the left hand side term of Eq.(3.3):

$$\mathbf{N}\hat{\Phi} = \mathbf{B}\Psi - \mathbf{C}\hat{\Phi} \qquad (3.6)$$

in which the matrix $\mathbf{N}$ is written as:

$$
\mathbf{N} = \begin{pmatrix}
N_{1,p}(\xi'_0) & N_{2,p}(\xi'_0) & \dots & N_{m,p}(\xi'_0) \\
N_{1,p}(\xi'_1) & N_{2,p}(\xi'_1) & \dots & N_{m,p}(\xi'_1) \\
\vdots & \vdots & \vdots & \vdots \\
N_{1,p}(\xi'_m) & N_{2,p}(\xi'_m) & \dots & N_{m,p}(\xi'_m)
\end{pmatrix}
\qquad (3.7)
$$

The solution of (4.15) is then:

$$\hat{\Phi} = (\mathbf{N} + \mathbf{C})^{-1} \mathbf{B}\hat{\Psi} \qquad (3.8)$$

We must note that the vector $\hat{\Phi}$ and $\hat{\Psi}$ are just coefficients of the representation (3.1) for φ and χ respectively and might not have a physical meaning.

3.1 Cubic Hermite

We assume the basis functions (or shape functions) to be the Hermite polynomials (Fig.3.1):

$$
\begin{aligned}
H_0(\xi) &= +2 - 3\xi + \xi^3 \\
H_1(\xi) &= +2 + 3\xi - \xi^3 \\
H_2(\xi) &= +1 - \xi - \xi^2 + \xi^3 \\
H_3(\xi) &= -1 - \xi + \xi^2 + \xi^3
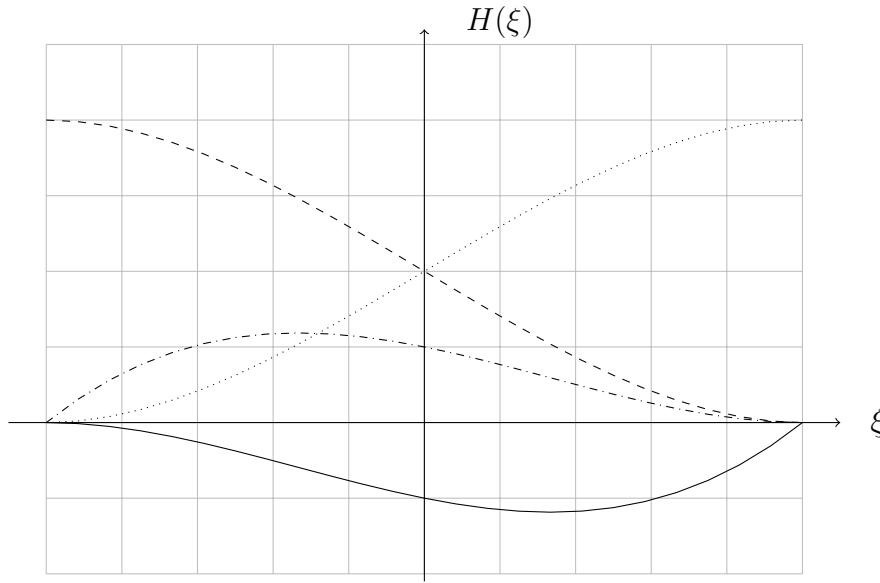\end{aligned} \tag{3.9}
$$

Figure 3.1: Hermite polynomials, $(--)\ H_0(\xi)$, $(\cdots)\ H_1(\xi)$, $(-\cdot-)\ H_2(\xi)$, $(-)$ $H_3(\xi)$

In this case, the representation (3.1) can be written as[2]

$$
f(\xi) = f_0 H_0(\xi) + f_1 H_1(\xi) + \left.\frac{\partial f}{\partial \xi}\right|_0 H_2(\xi) + \left.\frac{\partial f}{\partial \xi}\right|_1 H_3(\xi), \quad \xi \in [-1,1] \tag{3.10}
$$

in which $f_{0,1}$ and $\left.\frac{\partial f}{\partial \xi}\right|_{0,1}$ are the values of the function $f(\xi)$ and of its derivatives in $\xi = \pm 1$. We must note that, while Eq.(3.10) doesn't impose anything about the domain of the curvilinear coordinate ξ, in this case we are assuming it to be in the range $[-1,1]$ on a single panel, i.e. between two nodal points.

---

[2]for the sake of simplicity we drop the $\tilde{\bullet}$ on φ

3.1.1 The numerical solution

Applying representation (3.10) to Eq.(3.2) we have a linear system of equations in which the unknown are represented by the nodal values of $\phi(\xi_k)$ and $\frac{\partial \phi}{\partial \xi}\big|_k$ for each panel $i = 1, \ldots, N_{el}$:

$$
\begin{aligned}
E(\mathbf{y})\,\phi(\mathbf{y}) = \sum_{i=1}^{N_{el}} \Big(\quad & \chi_0^i \int_{\mathcal{S}_i} G(\xi,\mathbf{y})H_0(\xi)J(\xi)d\xi \\
+ \quad & \chi_1^i \int_{\mathcal{S}_i} G(\xi,\mathbf{y})H_1(\xi)J(\xi)d\xi \\
+ \quad & \frac{\partial \chi^i}{\partial \xi}\Big|_0 \int_{\mathcal{S}_i} G(\xi,\mathbf{y})H_2(\xi)J(\xi)d\xi \\
+ \quad & \frac{\partial \chi^i}{\partial \xi}\Big|_1 \int_{\mathcal{S}_i} G(\xi,\mathbf{y})H_3(\xi)J(\xi)d\xi \Big) \\
- \sum_{i=1}^{N_{el}} \Big(\quad & \varphi_0^i \int_{\mathcal{S}_i} \frac{\partial G(\xi,\mathbf{y})}{\partial n} H_0(\xi)J(\xi)d\xi \\
+ \quad & \varphi_1^i \int_{\mathcal{S}_i} \frac{\partial G(\xi,\mathbf{y})}{\partial n} H_1(\xi)J(\xi)d\xi \\
+ \quad & \frac{\partial \varphi^i}{\partial \xi}\Big|_0 \int_{\mathcal{S}_i} \frac{\partial G(\xi,\mathbf{y})}{\partial n} H_2(\xi)J(\xi)d\xi \\
+ \quad & \frac{\partial \varphi^i}{\partial \xi}\Big|_1 \int_{\mathcal{S}_i} \frac{\partial G(\xi,\mathbf{y})}{\partial n} H_3(\xi)J(\xi)d\xi \Big) \quad (3.11)
\end{aligned}
$$

In this case, $\hat{\varphi}_a$ and $\hat{\chi}_a$ happen to be the nodal values of φ and χ and of their derivatives but, generally speaking, the meaning of those vectors depends on the choice of the representation (3.1).

In order to obtain a system of $N_{el} + 1$ equation from Eq.(3.11) we can follow two different approaches described in the following sections.

3.1.2 Classic Cubic Hermite BEM

The classic methodology to obtain a linear system of equations from Eq.(3.11) involves the representation of the nodal derivatives with a finite difference schema.

We can apply, for instance, a two-points centred schema:

$$\frac{\partial \varphi}{\partial \xi}\bigg|_j = \frac{\varphi(\xi_{j+1}) - \varphi(\xi_{j-1})}{2} + O(h^2) \tag{3.12}$$

In this case the integral on the panel i contributes not only to the coefficients relative to its boundary nodal points but also to the nodal points involved in the derivative (3.12). As shown in Fig.(3.2), for instance, the element i will contribute to nodes k and $k+1$ as nodal values, to nodes $k-1$ and $k+1$ for the derivative in node k and to nodes k and $k+2$ for the derivative in node $k+1$. Eq.(3.11) can
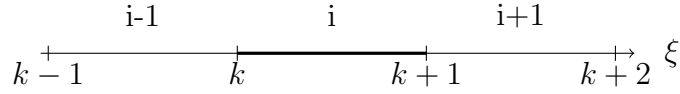

Figure 3.2: Element i on curvilinear coordinate ξ

hence be written as:

$$\mathbf{E}\Phi = \mathbf{B}\Psi + \mathbf{C}\Phi. \tag{3.13}$$

the solution of which is, once again, straightforward. It must be said that this approach is not innovative and has already been applied to both 3D [6] and 2D cases [11]. We include it here for the sake of completeness and to demonstrate the utility of this approach in high accuracy applications as described in Chapter 5.

3.1.2.1 Results and discussion

3.1.2.1.1 Planar wave on a 2D cylinder The above described approach has been tested on an acoustic scattering problem for which an analytical solution is known: a planar wave impinging on a 2D cylinder (see Appendix B). Indicating with $\mathbf{k}$ the wave vector, the incident field is given by $\varphi_i = \varphi_0 e^{i\mathbf{k}\cdot\mathbf{r}}$.

The validation has been performed for $f = 50$Hz, $f = 200$Hz and $f = 500$Hz by evaluating the scattering pressure at microphones collocated at $R = 20r$ where r is the radius of the cylinder. The agreement with the analytical solution is very good as shown in Figures 3.3, 3.4 and 3.5 in which the total scattering solution is plotted for the three analysed frequencies.
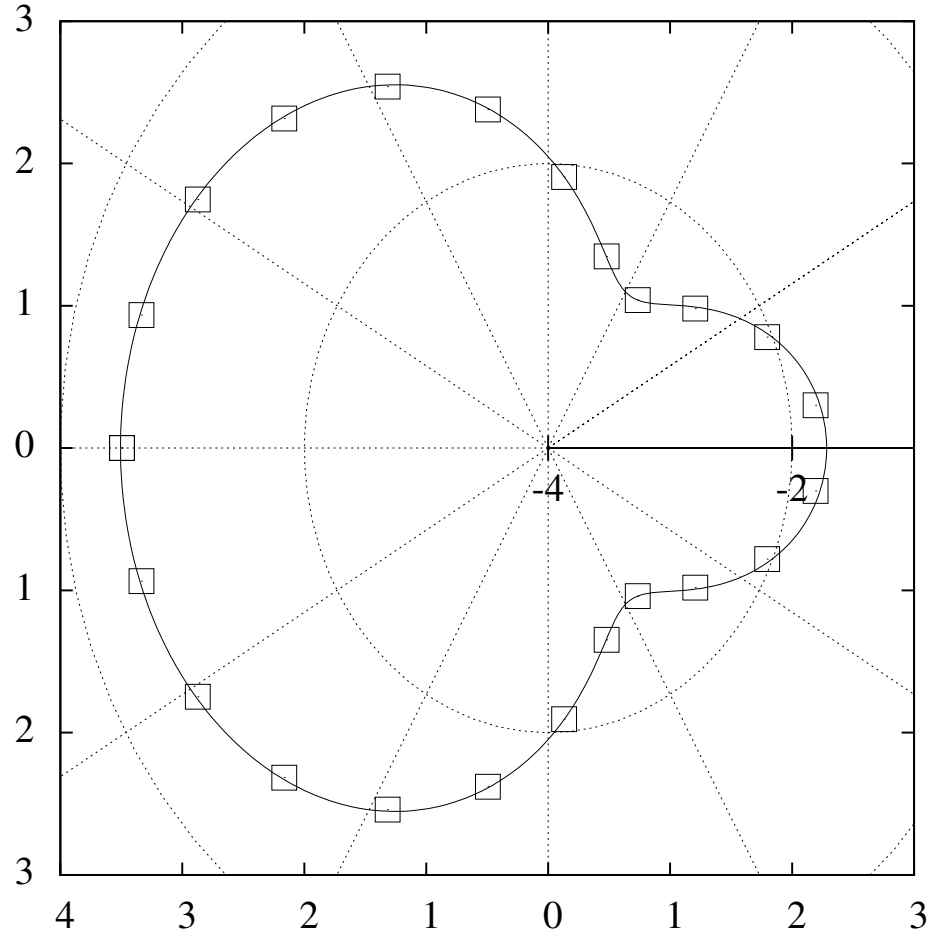
Figure 3.3: $2D$ Hermite: Planar wave on a $2D$ cylinder, Total scattering solution at $R = 20r$, $f = 50$Hz, $N_{el} = 16$, ($\square$) BEM, ($-$) Analytical
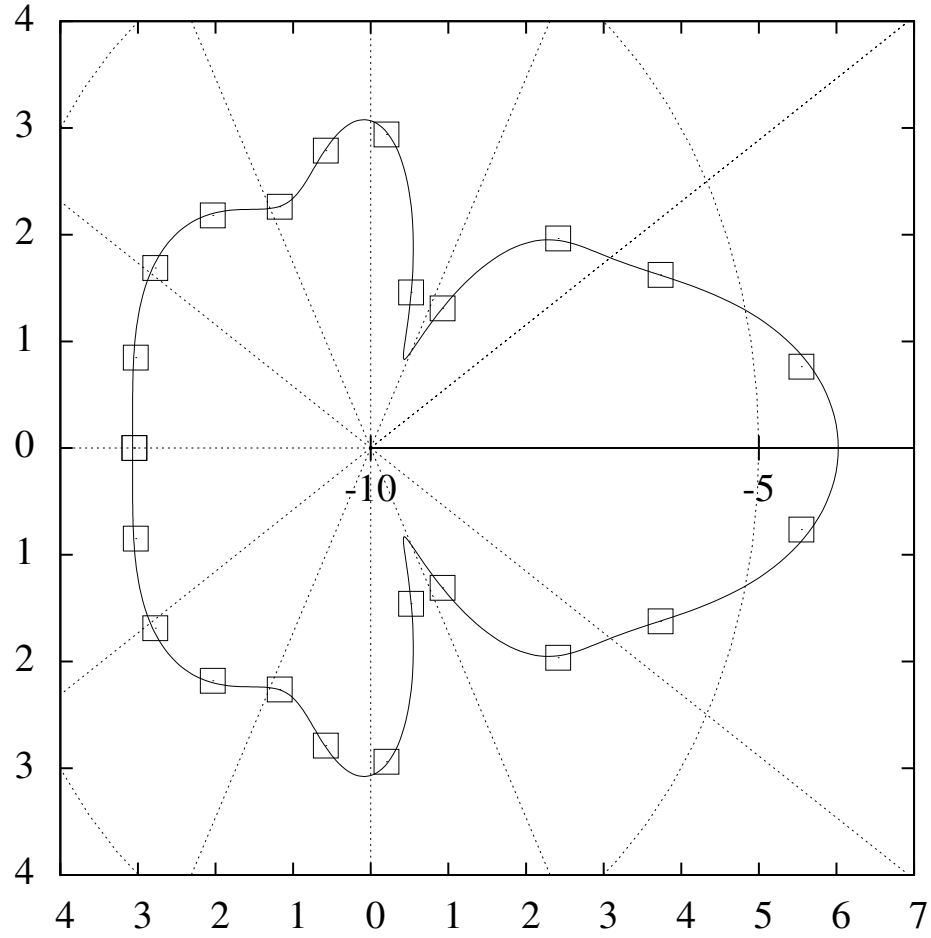
Figure 3.4: $2D$ Hermite: Planar wave on a $2D$ cylinder, Total scattering solution at $R = 20r$, $f = 200$Hz, $N_{el} = 32$, ($\square$) BEM, ($-$) Analytical
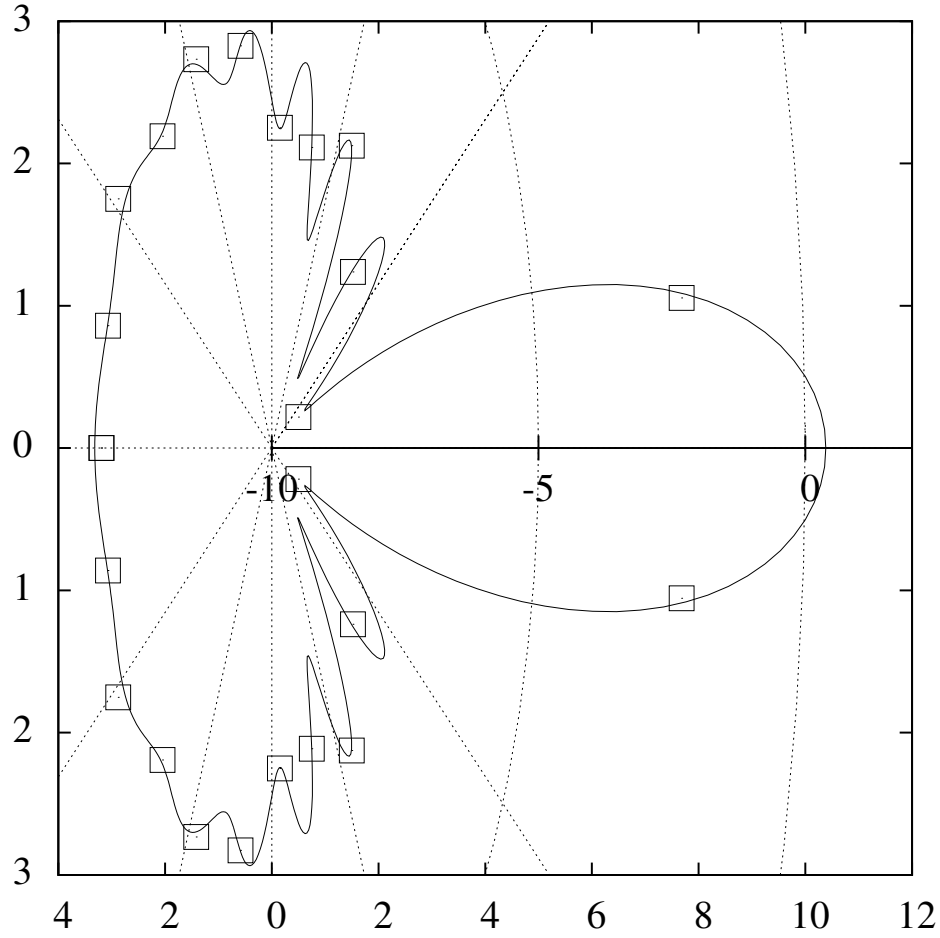
Figure 3.5: $2D$ Hermite: Planar wave on a $2D$ cylinder, Total scattering solution at $R = 20r$, $f = 500$Hz, $N_{el} = 64$, ($\square$) BEM, ($-$) Analytical

3.1.2.1.2 Numerical convergence analysis In order to evaluate the rate of convergence of the solution, an analysis has been performed on the same test case for the same three frequencies by evaluating both the Lebesgue norm of order 2 of the local relative difference $\|(\varphi_s - \varphi_a)/\varphi_a\|$, being φ_s the scattering solution on the surface:

$$\epsilon = \sqrt{\int_{\mathcal{S}} \left\| \frac{\varphi_s - \varphi_a}{\varphi_a} \right\|^2 d\mathcal{S}} \tag{3.14}$$

in which φ_a is the analytical solution and the relative error of the maximum value of φ_s, $\|\max(\varphi_s)-\max(\varphi_a)\|$ evaluated on the surface of the cylinder. The results, *i.e.*, the above described metrics plotted on a log–log scale against $1/N_{el}$ with N_{el} being the number of elements of the discretisation to the surface, are reported in figure 3.6,3.7 and 3.8 showing a convergence rate always > 1.
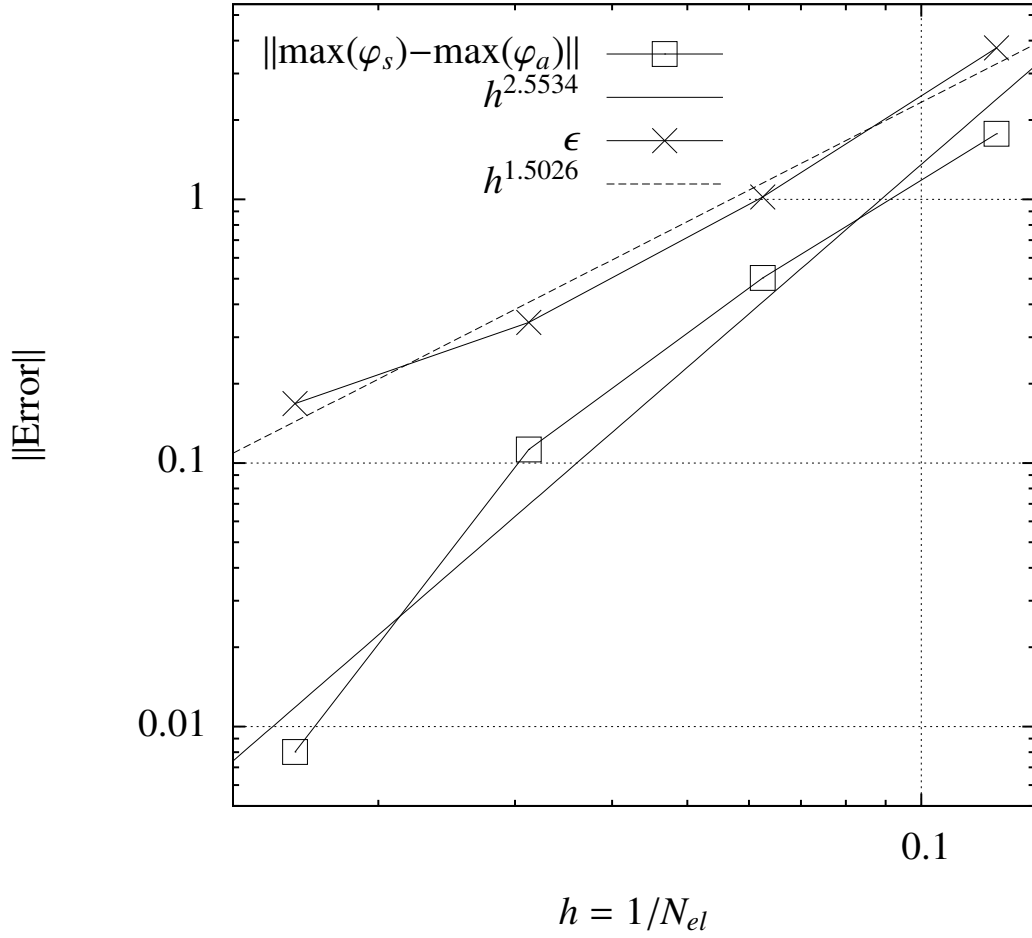

Figure 3.6: *2D* Hermite: Convergence analysis at $f = 50\text{Hz}$, ($\square$) $\|\max(\varphi_s)-\max(\varphi_a)\|$, (—) $x^{2.5534}$, ($\times$) ϵ , (- - -) $x^{1.5026}$
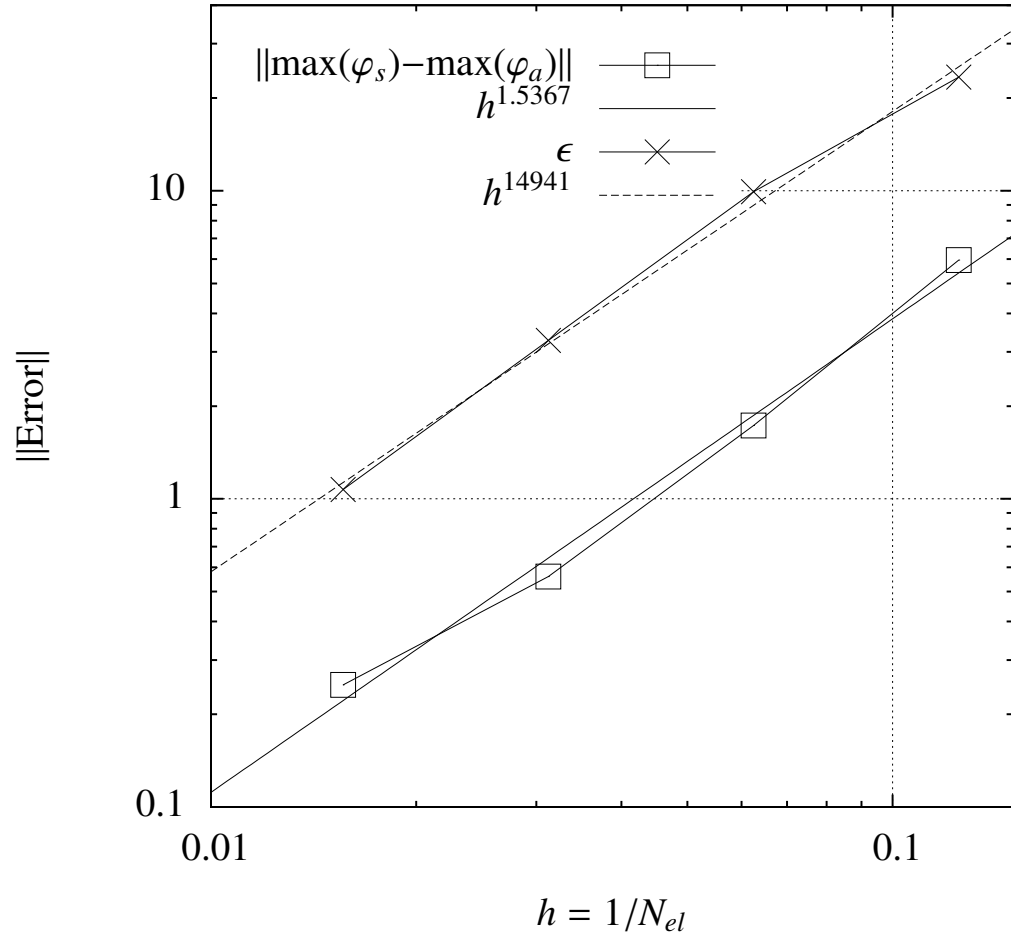
Figure 3.7: 2D Hermite: Convergence analysis at $f = 200$Hz, ($\square$) $\|\max(\varphi_s) - \max(\varphi_a)\|$, (—) $x^{1.5367}$, ($\times$) ϵ , (- - -) $x^{1.4941}$
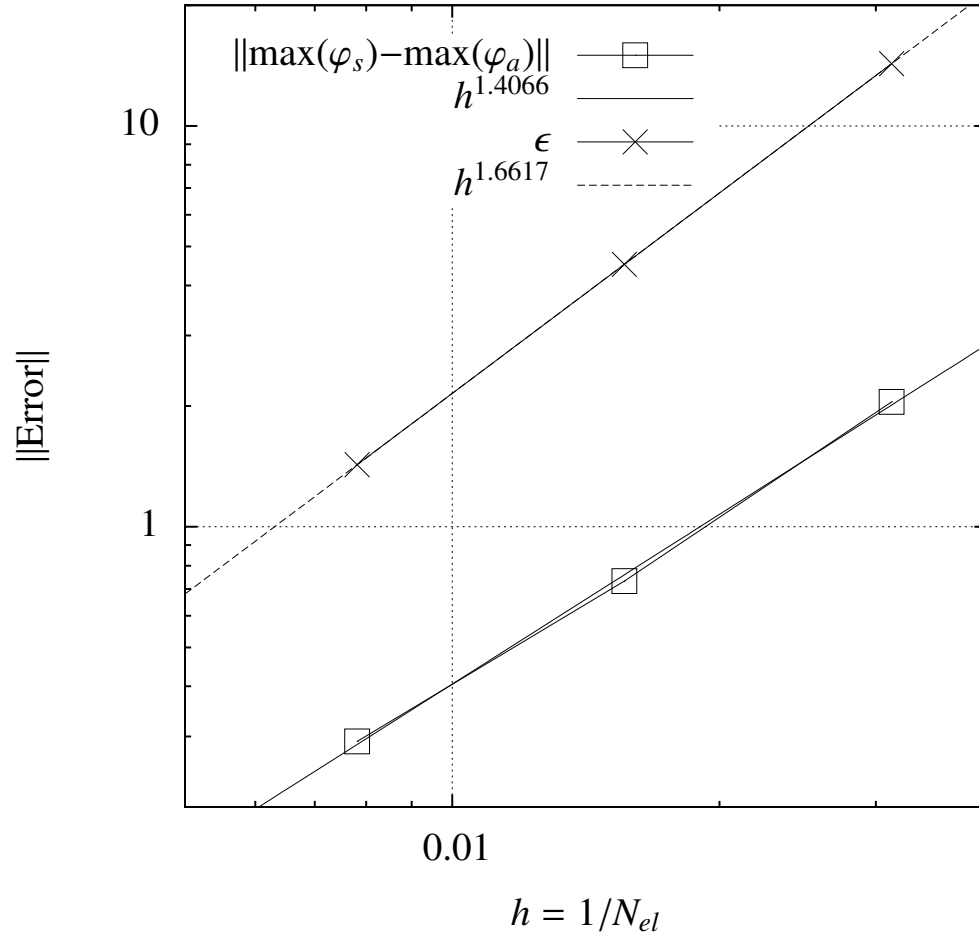
Figure 3.8: $2D$ Hermite: Convergence analysis at $f = 500$Hz, ($\square$) $\|\max(\varphi_s) - \max(\varphi_a)\|$, (——) $x^{1.4066}$, ($\times$) ϵ , (- - -) $x^{1.6617}$

The convergence rates are reported in Table 3.1.

Table 3.1: 2D Hermite: Convergence Rate at $f = 50$Hz, $f = 200$Hz and $f = 500$Hz

Method	$f = 50$Hz	$f = 200$Hz	$f = 500$Hz
$\|\max(\varphi_s) - \max(\varphi_a)\|$	2.5534	1.5367	1.4066
ϵ	1.5026	1.4941	1.6617

3.1.3 Dual BEM

Another approach is to consider the nodal derivatives of φ as unknown. In this case, in order to have a system of $2(N_{el+1})$ equations we can consider the gradient of Eq. (2.8):

$$E(\mathbf{y})\,\nabla_t^* \varphi(\mathbf{y}) = \nabla_t^* \oint_{\mathcal{S}} \left(G\frac{\partial \tilde{\varphi}}{\partial n} - \varphi\frac{\partial G}{\partial n} \right) d\mathcal{S}(\mathbf{x}). \tag{3.15}$$

which, after the discretization and the projection on the covariant base $\mathbf{g_1}$, becomes:

$$
\begin{aligned}
E(\mathbf{y})\frac{\partial \varphi(\mathbf{y})}{\partial \xi} = \sum_{i=1}^{N_{el}} \Big(&\chi_0^i \int_{\mathcal{S}_i} \frac{\partial G(\xi,\mathbf{y})}{\partial \xi} H_{00}(\xi) J(\xi) d\xi \\
+ \quad &\chi_1^i \int_{\mathcal{S}_i} \frac{\partial G(\xi,\mathbf{y})}{\partial \xi} H_{10}(\xi) J(\xi) d\xi \\
+ \quad &\frac{\partial \chi^i}{\partial \xi}\Big|_0 \int_{s_i} \frac{\partial G(\xi,\mathbf{y})}{\partial \xi} H_{01}(\xi) J(\xi) d\xi \\
+ \quad &\frac{\partial \chi^i}{\partial \xi}\Big|_1 \int_{s_i} \frac{\partial G(\xi,\mathbf{y})}{\partial \xi} H_{11}(\xi) J(\xi) d\xi \Big) \\
- \sum_{i=1}^{N_{el}} \Big(&\varphi_0^i \int_{\mathcal{S}_i} \frac{\partial G(\xi,\mathbf{y})}{\partial n \partial \xi} H_{00}(\xi) J(\xi) d\xi \\
+ \quad &\varphi_1^i \int_{\mathcal{S}_i} \frac{\partial G(\xi,\mathbf{y})}{\partial n \partial \xi} H_{10}(\xi) J(\xi) d\xi \\
+ \quad &\frac{\partial \varphi^i}{\partial \xi}\Big|_0 \int_{s_i} \frac{\partial G(\xi,\mathbf{y})}{\partial n \partial \xi} H_{01}(\xi) J(\xi) d\xi \\
+ \quad &\frac{\partial \varphi^i}{\partial \xi}\Big|_1 \int_{s_i} \frac{\partial G(\xi,\mathbf{y})}{\partial n \partial \xi} H_{11}(\xi) J(\xi) d\xi \Big) \tag{3.16}
\end{aligned}
$$

We now have a system of $2(N_{el+1})$:

$$E\widehat{\Phi} = \mathbf{B}\widehat{\Psi} - \mathbf{C}\widehat{\Phi} \tag{3.17}$$

in which:

$$
\widehat{\Phi} = \begin{pmatrix} \varphi \\ \varphi \\ \vdots \\ \varphi \\ \overline{\hspace{1cm}} \\ \left.\frac{\partial \varphi}{\partial \xi}\right|_0 \\ \left.\frac{\partial \varphi}{\partial \xi}\right|_1 \\ \vdots \\ \left.\frac{\partial \varphi}{\partial \xi}\right|_n \end{pmatrix}
\qquad
\widehat{\Psi} = \begin{pmatrix} \chi_0 \\ \chi_1 \\ \vdots \\ \chi_n \\ \overline{\hspace{1cm}} \\ \left.\frac{\partial \chi}{\partial \xi}\right|_0 \\ \left.\frac{\partial \chi}{\partial \xi}\right|_1 \\ \vdots \\ \left.\frac{\partial \chi}{\partial \xi}\right|_n \end{pmatrix}
\tag{3.18}
$$

The matrices $\mathbf{B}$ and $\mathbf{C}$ elements are given by the integrals of the kernels and of their derivative, in particular if we write:

$$
B0_{ij} = \int_{\mathcal{S}_i} G(\xi, \mathbf{y}_j) H(\xi) J(\xi) d\xi
$$

$$
B1_{ij} = \int_{\mathcal{S}_i} G(\xi, \mathbf{y}_j) H'(\xi) J(\xi) d\xi
$$

$$
B2_{ij} = \int_{\mathcal{S}_i} \frac{\partial G(\xi, \mathbf{y}_j)}{\partial \xi} H(\xi) J(\xi) d\xi
$$

$$
B3_{ij} = \int_{\mathcal{S}_i} \frac{\partial G(\xi, \mathbf{y}_j)}{\partial \xi} H'(\xi) J(\xi) d\xi
$$

$$
C0_{ij} = \int_{\mathcal{S}_i} \frac{\partial G(\xi, \mathbf{y}_j)}{\partial n} H(\xi) J(\xi) d\xi
$$

$$
C1_{ij} = \int_{\mathcal{S}_i} \frac{\partial G(\xi, \mathbf{y}_j)}{\partial n} H'\xi) J(\xi) d\xi
$$

$$
C2_{ij} = \int_{s_i} \frac{\partial G(\xi, \mathbf{y}_j)}{\partial n \partial \xi} H(\xi) J(\xi) d\xi
$$

$$
C3_{ij} = \int_{s_i} \frac{\partial G(\xi, \mathbf{y}_j)}{\partial n \partial \xi} H'(\xi) J(\xi) d\xi.
\tag{3.19}
$$

being $H(\xi)$ and $H'(\xi)$ the Hermite polynomials for the nodal values and the derivatives respectively, we have the following partitions for the matrices $\mathbf{B}$ and $\mathbf{C}$:

$$
\mathbf{B} = \left[\begin{array}{c|c} \mathbf{B0} & \mathbf{B1} \\ \hline \mathbf{B2} & \mathbf{B3} \end{array} \right]
\qquad
\mathbf{C} = \left[\begin{array}{c|c} \mathbf{C0} & \mathbf{C1} \\ \hline \mathbf{C2} & \mathbf{C3} \end{array} \right]
\tag{3.20}
$$

Solving system (3.17) gives us, as a result, the values of φ and of its derivative in the collocation points.

3.1.3.1 Results and discussion

3.1.3.1.1 Planar wave on a 2D cylinder The same analysis as in the finite difference approach has been performed for the Hermite Dual approach. In Figures 3.9, 3.10 and 3.11 we reported the total scattering solution at $R = 20r$ for $f = 50$Hz, $f = 200$Hz and $f = 500$Hz respectively. The results are again in good agreement with the analytical solution.
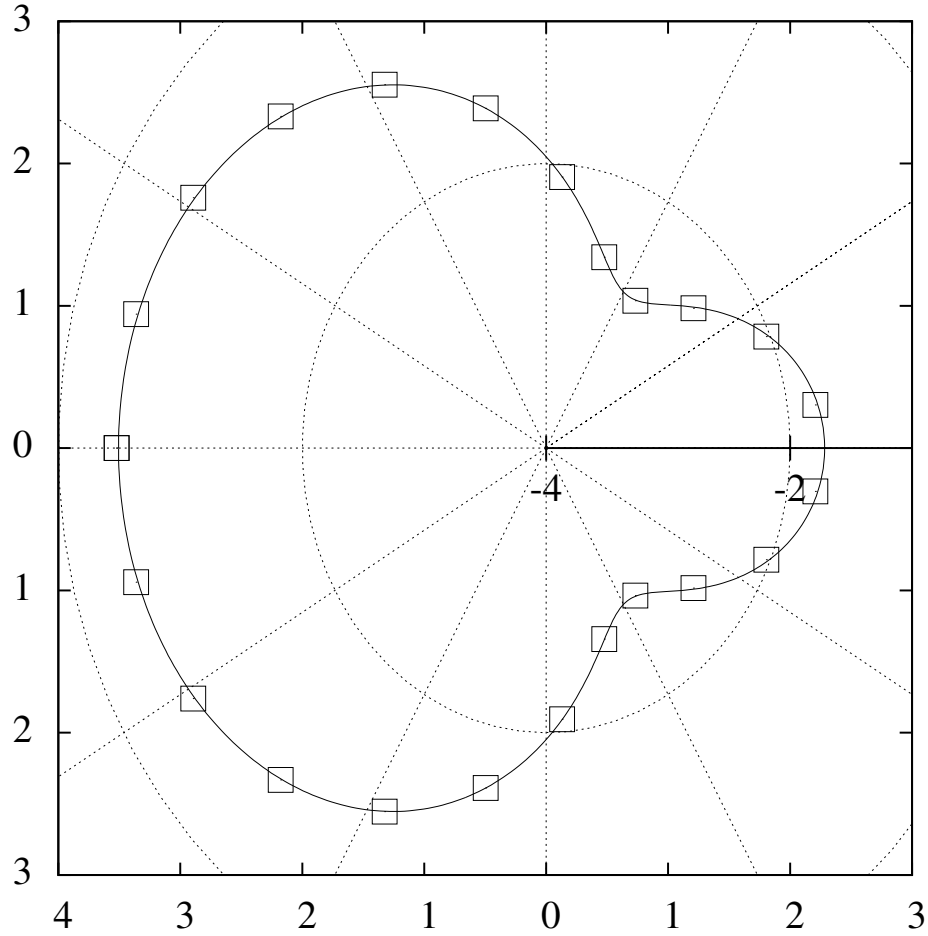

Figure 3.9: $2D$ Hermite Dual: Planar wave on a $2D$ cylinder, Total Scattering Solution at $R = 20r$, $f = 50$Hz, $N_{el} = 16$, ($\square$) BEM, ($-$) Analytical
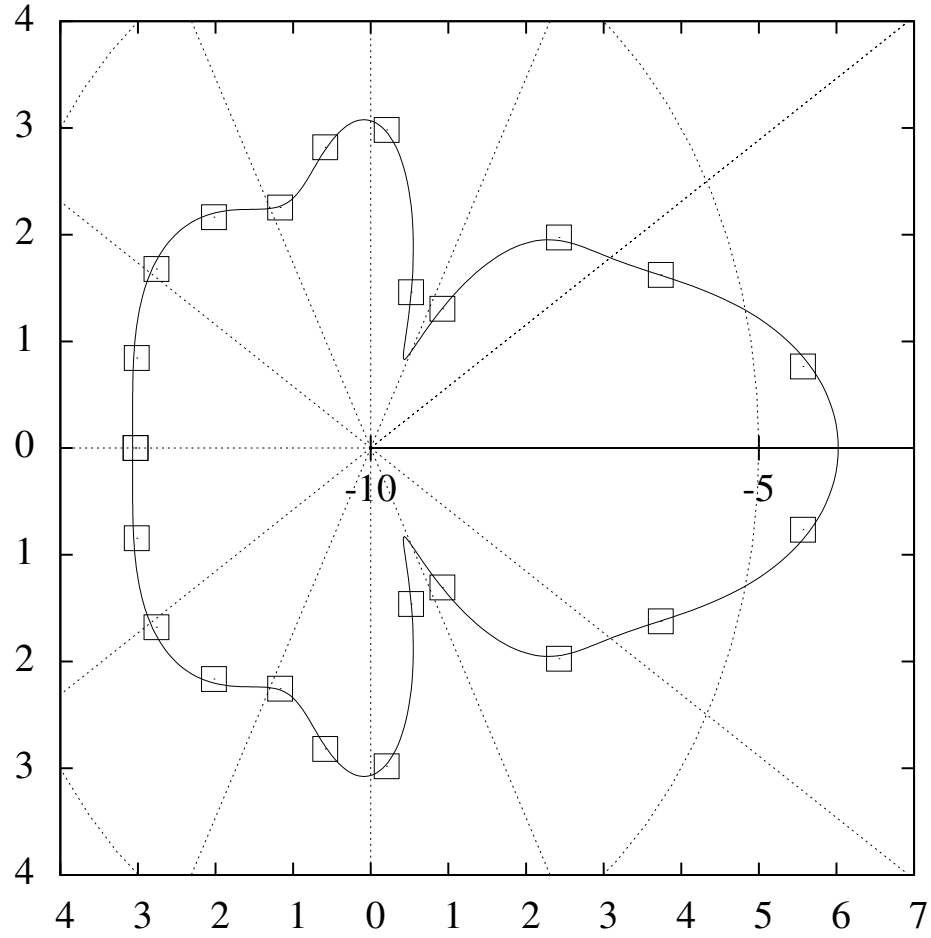
Figure 3.10: $2D$ Hermite Dual: Planar wave on a $2D$ cylinder, Total Scattering Solution at $R = 20r$, $f = 200$Hz, $N_{el} = 32$, ($\square$) BEM, ($-$) Analytical
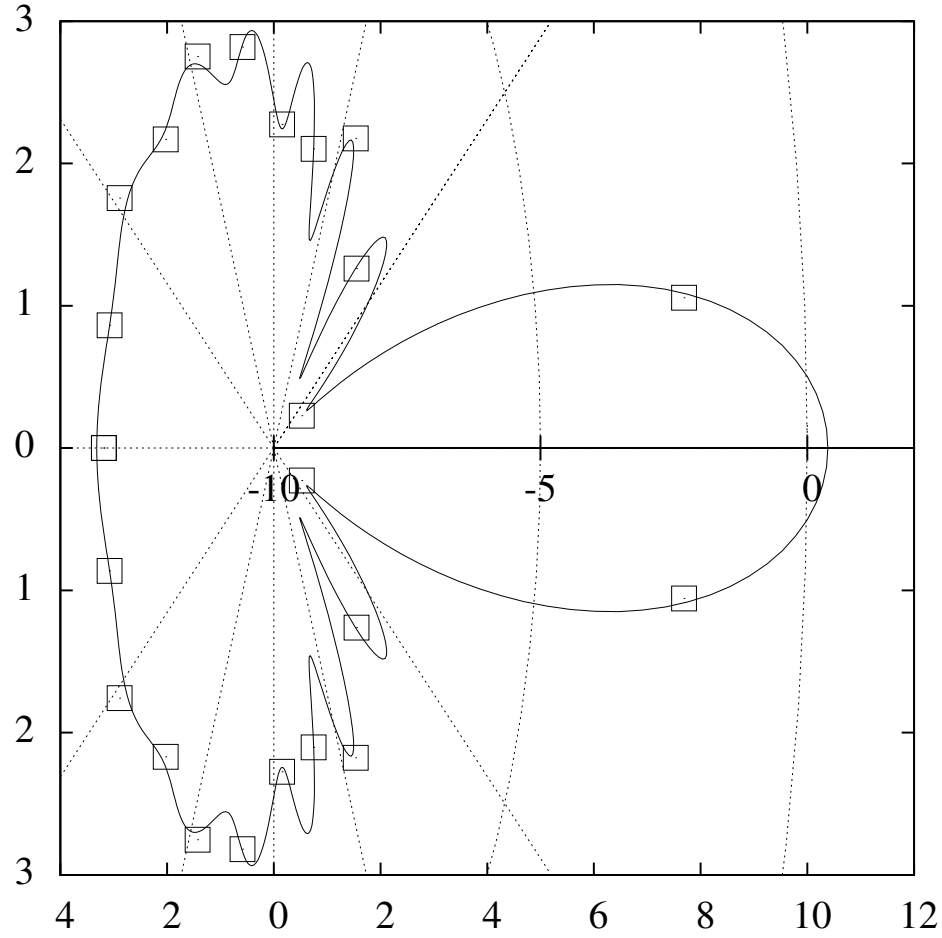
Figure 3.11: $2D$ Hermite Dual: Planar wave on a $2D$ cylinder, Total Scattering Solution at $R = 20r$, $f = 500$Hz, $N_{el} = 64$, ($\square$) BEM, (−) Analytical

3.1.3.1.2 Numerical convergence analysis The same numerical convergence analysis as in the previous approach has been performed here leading to even better convergence rates.
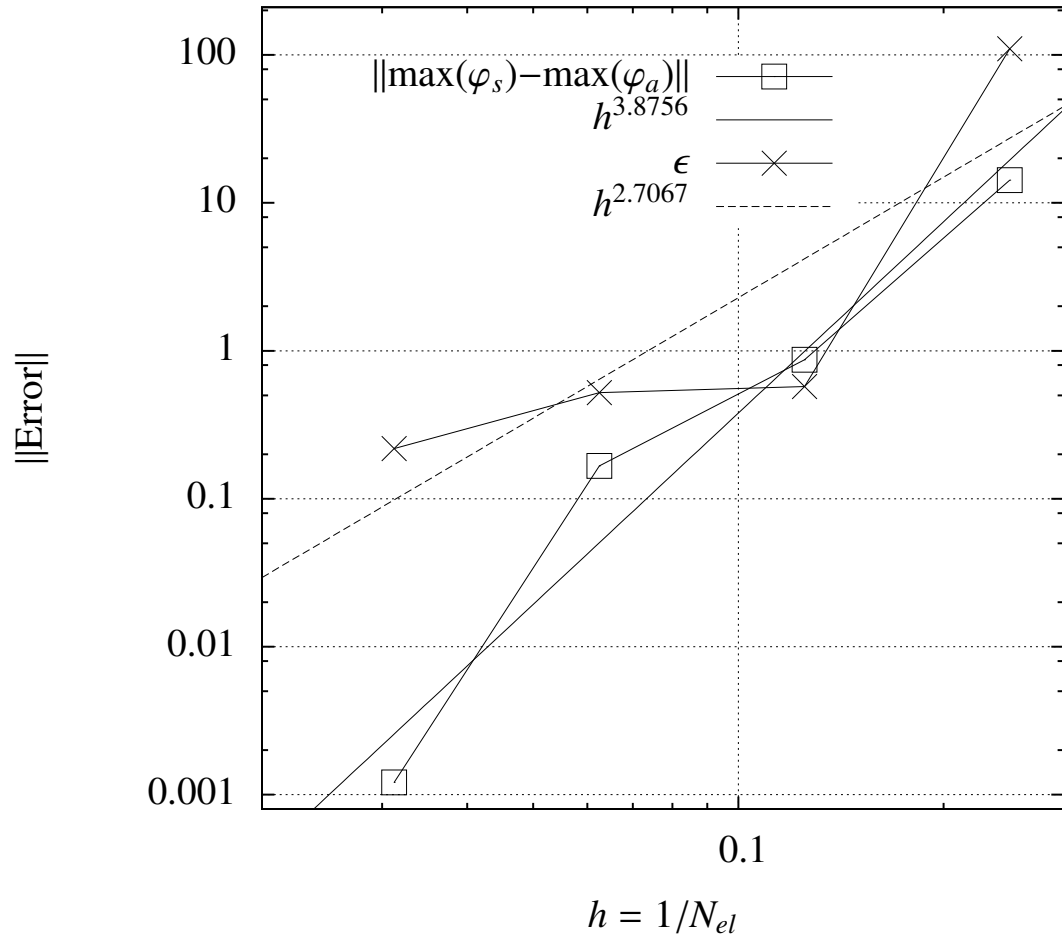
Figure 3.12: $2D$ Hermite Dual: Convergence analysis at $f = 50\text{Hz}$, ($\square$) $\|\max(\varphi_s) - \max(\varphi_a)\|$, (——) $x^{3.8756}$, ($\times$) ϵ , (- - -) $x^{2.7067}$

Figure 3.13: $2D$ Hermite Dual: Convergence analysis at $f = 200$Hz, $(\square)$ $\|\max(\varphi_s) - \max(\varphi_a)\|$, $(—)$ $x^{2.8298}$, $(\times)$ ϵ , (- - -) $x^{1.4565}$
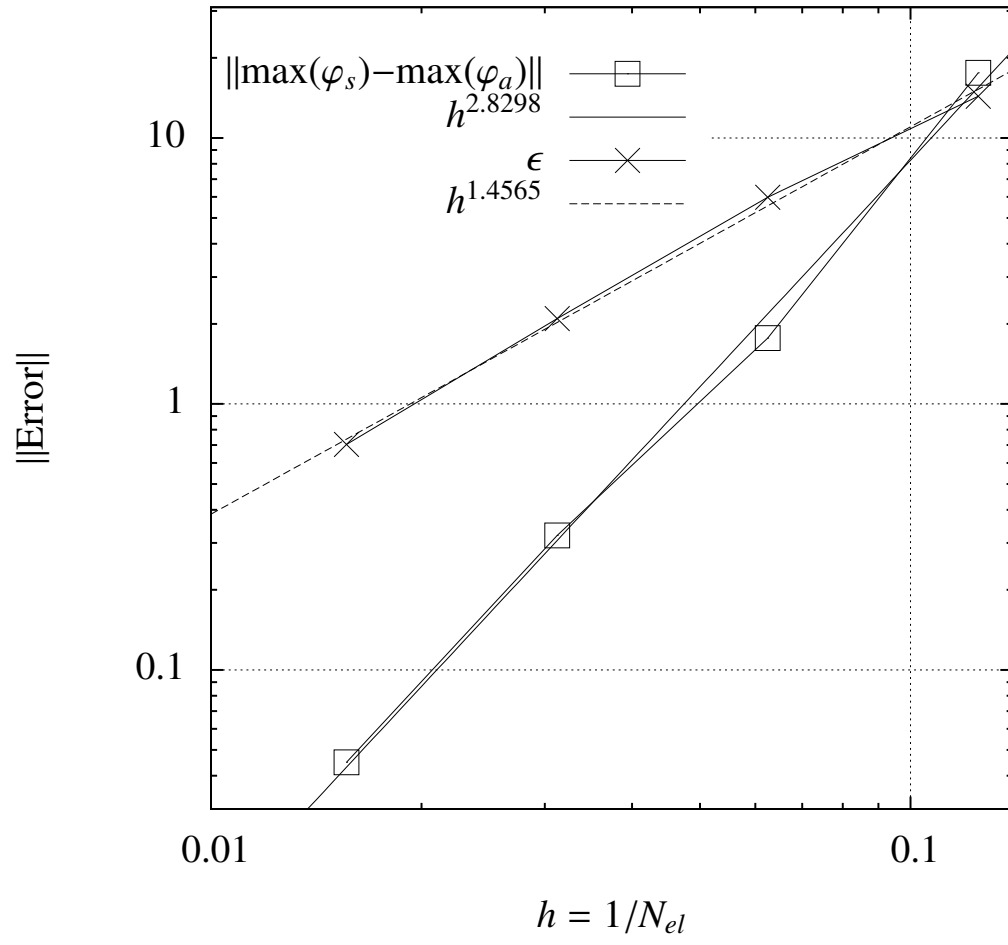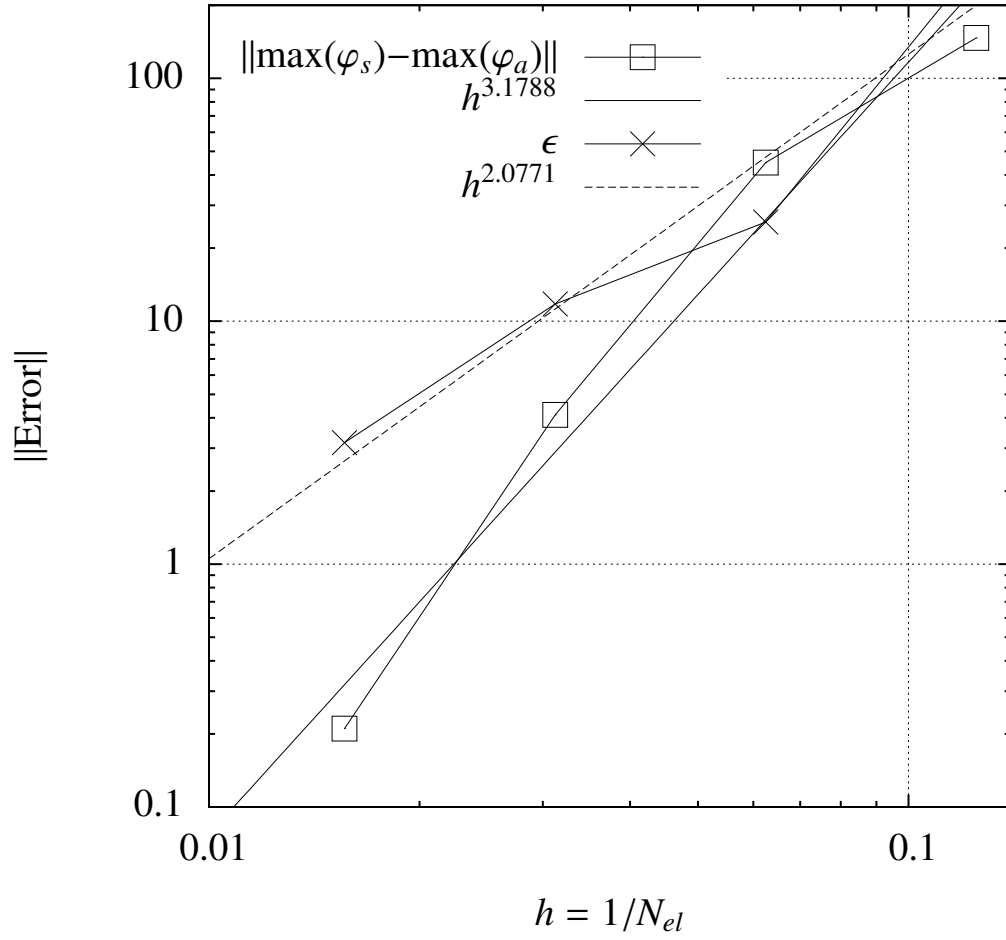
Figure 3.14: 2D Hermite Dual: Convergence analysis at $f = 500$Hz, ($\square$) $\|\max(\varphi_s) - \max(\varphi_a)\|$, (—) $x^{3.1788}$, ($\times$) ϵ , (- - -) $x^{2.0771}$

The convergence rates are reported in Table 3.2.

Table 3.2: 2D Hermite Dual: Convergence Rate at $f = 50$Hz, $f = 200$Hz and $f = 500$Hz

Method	$f = 50$Hz	$f = 200$Hz	$f = 500$Hz
$\|\max(\varphi_s) - \max(\varphi_a)\|$	4.296	2.8298	3.1788
ϵ	1.4565	2.0771	2.7067

29

3.2 Hermite Coons

The approach described in the previous chapter can easily be applied to 3D cases. The representation of a function $\mathbf{x}(\xi, \eta)$ in 3D, however, involves a bi–cubic interpolation which takes into account the mixed derivatives in $\xi\eta$ evaluated at the nodal points.

This introduces an additional complexity due to the second–order derivatives in the representation of the geometry and of the variables. In this chapter we will introduced an approach based on the work published by Steven Anton Coons in 1967[1] at MIT in which he described a methodology to describe generalised *surface patches* based on boundary curves and *blending functions* for the interpolation of the internal points. This kind of approach avoids the introduction of the nodal mixed derivatives while granting the freedom of choosing a suitable algorithm for the representation of the boundary curves.
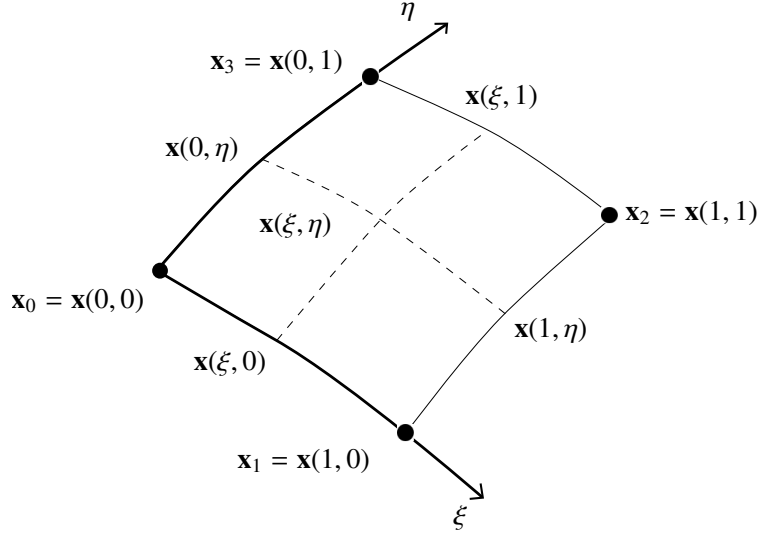
3.2.1 The Coons patch

Consider a two–dimensional manifold $\mathbf{x}(\xi, \eta)$, with $\mathbf{x} \in \mathbb{R}^3$, bounded by the four curves $\mathbf{x}_{0\eta} = \mathbf{x}(0, \eta)$, $\mathbf{x}_{1\eta} = \mathbf{x}(1, \eta)$, $\mathbf{x}_{\xi 0} = \mathbf{x}(\xi, 0)$, $\mathbf{x}_{\xi 1} = \mathbf{x}(\xi, 1)$ sharing the four corners $\mathbf{x}_0 = \mathbf{x}(0, 0)$, $\mathbf{x}_1 = \mathbf{x}(1, 0)$, $\mathbf{x}_2 = \mathbf{x}(1, 1)$, $\mathbf{x}_3 = \mathbf{x}(0, 1)$ (see Figure 3.15) we can build a patch interpolation considering the sum of the two lofting surfaces in ξ and η

$$
\begin{aligned}
\mathbf{s}_\eta(\xi, \eta) &= (1 - \eta)\, \mathbf{x}(\xi, 0) + \eta\, \mathbf{x}(\xi, 1) \\
\mathbf{s}_\xi(\xi, \eta) &= (1 - \xi)\, \mathbf{x}(0, \eta) + \xi\, \mathbf{x}(1, \eta)
\end{aligned}
\tag{3.21}
$$

If we consider the sum of $\mathbf{s}_\xi$ and $\mathbf{s}_\eta$ and we evaluate it at the boundaries, we note that, in order to get back the boundary curves, we must subtract a bilinear interpolation of the values of $\mathbf{x}$ at the four corners:

$$
\begin{aligned}
\mathbf{s}_{\xi\eta}(\xi, \eta) &= (1 - \xi)(1 - \eta)\, \mathbf{x}_0 \\
&+ \xi(1 - \eta)\, \mathbf{x}_1 \\
&+ \eta(1 - \xi)\, \mathbf{x}_3 \\
&+ \xi\eta\, \mathbf{x}_2
\end{aligned}
\tag{3.22}
$$

Figure 3.15: Quadrilateral patch in a curvilinear space $x(\xi, \eta)$

obtaining the interpolation introduced by Steven Coons[1] and known as Coons patch.

$$\mathbf{x}(\xi, \eta) \;=\; \mathbf{s}_\xi(\xi, \eta) + \mathbf{s}_\eta(\xi, \eta) - \mathbf{s}_{\xi\eta}(\xi, \eta) \tag{3.23}$$

Equation(3.23) is only dependent on the four boundary curves and on the values at the corners without the need of mixed derivatives in $\xi\eta$.

Adopting, for the representation along the boundaries, the cubic Hermite poly-

nomials in the span $\zeta \in [0, 1]$:

$$
\begin{aligned}
H_0(\zeta) &= \frac{1}{4}(1 - 3\zeta + \zeta^3) \\
H_1(\zeta) &= \frac{1}{4}(1 + 3\zeta - \zeta^3) \\
H_2(\zeta) &= \frac{1}{4}(1 - \zeta - \zeta^2 + \zeta^3) \\
H_3(\zeta) &= \frac{1}{4}(-1 - \zeta + \zeta^2 + \zeta^3)
\end{aligned}
\tag{3.24}
$$

and their derivatives

$$
\begin{aligned}
H_0'(\zeta) &= \frac{1}{4}(-3 + 3\zeta^2) \\
H_1'(\zeta) &= \frac{1}{4}(3 - 3\zeta^2) \\
H_2'(\zeta) &= \frac{1}{4}(-1 - 2\zeta + 3\zeta^2) \\
H_3'(\zeta) &= \frac{1}{4}(-1 + 2\zeta + 3\zeta^2)
\end{aligned}
\tag{3.25}
$$

we can substitute the boundary curves with their cubic Hermite approximation, indicated with the bar, having the form:

$$
\bar{\mathbf{x}}_{\xi 0} = \mathbf{x}_0 H_0(\xi) + \mathbf{x}_1 H_1(\xi) + \left.\frac{\partial \mathbf{x}_{\xi 0}}{\partial \xi}\right|_{\xi=0} H_2(\xi) + \left.\frac{\partial \mathbf{x}_{\xi 0}}{\partial \xi}\right|_{\xi=1} H_3(\xi)
\tag{3.26}
$$

$$
\bar{\mathbf{x}}_{\xi 1} = \mathbf{x}_3 H_0(\xi) + \mathbf{x}_2 H_1(\xi) + \left.\frac{\partial \mathbf{x}_{\xi 1}}{\partial \xi}\right|_{\xi=0} H_2(\xi) + \left.\frac{\partial \mathbf{x}_{\xi 1}}{\partial \xi}\right|_{\xi=1} H_3(\xi)
\tag{3.27}
$$

$$
\bar{\mathbf{x}}_{0\eta} = \mathbf{x}_0 H_0(\xi) + \mathbf{x}_3 H_1(\xi) + \left.\frac{\partial \mathbf{x}_{0\eta}}{\partial \eta}\right|_{\eta=0} H_2(\xi) + \left.\frac{\partial \mathbf{x}_{0\eta}}{\partial \eta}\right|_{\eta=1} H_3(\xi)
\tag{3.28}
$$

$$
\bar{\mathbf{x}}_{1\eta} = \mathbf{x}_1 H_0(\xi) + \mathbf{x}_2 H_1(\xi) + \left.\frac{\partial \mathbf{x}_{1\eta}}{\partial \eta}\right|_{\eta=0} H_2(\xi) + \left.\frac{\partial \mathbf{x}_{1\eta}}{\partial \eta}\right|_{\eta=1} H_3(\xi)
\tag{3.29}
$$

$$
\tag{3.30}
$$

in which the only needed quantities are the values at the boundary of the interval and the derivatives along the boundary curve. Combining the Coons patch representation in Eq.(3.23) with the cubic Hermite representation for the

boundary curves in Eq.(3.26), we obtain the following equation for the patch:

$$
\begin{aligned}
\mathbf{x}(\xi,\eta) \;=\; & \frac{1-\xi}{2}\left[\mathbf{x}_0 H_0(\eta) + \mathbf{x}_3 H_1(\eta) + \frac{\partial \mathbf{x}}{\partial \eta}\Big|_0 H_2(\eta) + \frac{\partial \mathbf{x}}{\partial \eta}\Big|_3 H_3(\eta)\right] \\
+ & \frac{1+\xi}{2}\left[\mathbf{x}_1 H_0(\eta) + \mathbf{x}_2 H_1(\eta) + \frac{\partial \mathbf{x}}{\partial \eta}\Big|_1 H_2(\eta) + \frac{\partial \mathbf{x}}{\partial \eta}\Big|_2 H_3(\eta)\right] \\
+ & \frac{1-\eta}{2}\left[\mathbf{x}_0 H_0(\xi) + \mathbf{x}_1 H_1(\xi) + \frac{\partial \mathbf{x}}{\partial \xi}\Big|_0 H_2(\xi) + \frac{\partial \mathbf{x}}{\partial \xi}\Big|_1 H_3(\xi)\right] \\
+ & \frac{1+\eta}{2}\left[\mathbf{x}_3 H_0(\xi) + \mathbf{x}_2 H_1(\xi) + \frac{\partial \mathbf{x}}{\partial \xi}\Big|_3 H_2(\xi) + \frac{\partial \mathbf{x}}{\partial \xi}\Big|_2 H_3(\xi)\right] \\
- & \left(\frac{1+\xi}{2}\frac{1+\eta}{2}\mathbf{x}_2 + \frac{1+\xi}{2}\frac{1-\eta}{2}\mathbf{x}_1\right) \\
+ & \left(\frac{1-\xi}{2}\frac{1+\eta}{2}\mathbf{x}_3 + \frac{1-\xi}{2}\frac{1-\eta}{2}\mathbf{x}_0\right) \qquad (3.31)
\end{aligned}
$$

and, for the derivatives in ξ and η

$$
\begin{aligned}
\frac{\partial \mathbf{x}(\xi,\eta)}{\partial \xi} \;=\; & -\frac{1}{2}\left[\mathbf{x}_0 H_0(\eta) + \mathbf{x}_3 h_1(\eta) + \frac{\partial \mathbf{x}}{\partial \eta}\Big|_0 H_2(\eta) + \frac{\partial \mathbf{x}}{\partial \eta}\Big|_3 H_3(\eta)\right] \\
+ & \frac{1}{2}\left[\mathbf{x}_1 H_0(\eta) + \mathbf{x}_2 H_1(\eta) + \frac{\partial \mathbf{x}}{\partial \eta}\Big|_1 H_2(\eta) + \frac{\partial \mathbf{x}}{\partial \eta}\Big|_2 H_3(\eta)\right] \\
+ & \frac{1-\eta}{2}\left[\mathbf{x}_0 H_0'(\xi) + \mathbf{x}_1 H_1'(\xi) + \frac{\partial \mathbf{x}}{\partial \xi}\Big|_0 H_2'(\xi) + \frac{\partial \mathbf{x}}{\partial \xi}\Big|_1 H_3'(\xi)\right] \\
+ & \frac{1+\eta}{2}\left[\mathbf{x}_3 H_0'(\xi) + \mathbf{x}_2 H_1'(\xi) + \frac{\partial \mathbf{x}}{\partial \xi}\Big|_3 H_2'(\xi) + \frac{\partial \mathbf{x}}{\partial \xi}\Big|_2 H_3'(\xi)\right] \\
- & \left(\frac{1+\eta}{4}\mathbf{x}_2 + \frac{1-\eta}{4}\mathbf{x}_1 - \frac{1+\eta}{4}\mathbf{x}_3 - \frac{1-\eta}{4}\mathbf{x}_0\right) \qquad (3.32)
\end{aligned}
$$

$$
\begin{aligned}
\frac{\partial \mathbf{x}(\xi,\eta)}{\partial \eta} \;=\; & \frac{1-\xi}{2}\left[\mathbf{x}_0 H_0'(\eta) + \mathbf{x}_3 H_1'(\eta) + \frac{\partial \mathbf{x}}{\partial \eta}\Big|_0 H_2'(\eta) + \frac{\partial \mathbf{x}}{\partial \eta}\Big|_3 H_3'(\eta)\right] \\
+ & \frac{1+\xi}{2}\left[\mathbf{x}_1 H_0'(\eta) + \mathbf{x}_2 H_1'(\eta) + \frac{\partial \mathbf{x}}{\partial \eta}\Big|_1 H_2'(\eta) + \frac{\partial \mathbf{x}}{\partial \eta}\Big|_2 H_3'(\eta)\right] \\
- & \frac{1}{2}\left[\mathbf{x}_0 H_0(\xi) + \mathbf{x}_1 H_1(\xi) + \frac{\partial \mathbf{x}}{\partial \xi}\Big|_0 H_2(\xi) + \frac{\partial \mathbf{x}}{\partial \xi}\Big|_1 H_3(\xi)\right] \\
+ & \frac{1}{2}\left[\mathbf{x}_3 H_0(\xi) + \mathbf{x}_2 H_1(\xi) + \frac{\partial \mathbf{x}}{\partial \xi}\Big|_3 H_2(\xi) + \frac{\partial \mathbf{x}}{\partial \xi}\Big|_2 H_3(\xi)\right] \\
- & \left(\frac{1+\xi}{4}\mathbf{x}_2 - \frac{1+\xi}{4}\mathbf{x}_1 + \frac{1-\xi}{4}\mathbf{x}_3 - \frac{1-\xi}{4}\mathbf{x}_0\right) \qquad (3.33)
\end{aligned}
$$

Collecting by nodal values, these equations can be written as:

$$
\mathbf{x}(\xi,\eta) = \sum_{i=0}^{3} \left[\mathbf{x}_i \mathcal{C}_i(\xi,\eta) + \frac{\partial \mathbf{x}}{\partial \xi}\Big|_i \mathcal{D}_i^{\xi}(\xi,\eta) + \frac{\partial \mathbf{x}}{\partial \eta}\Big|_i \mathcal{D}_i^{\eta}(\xi,\eta) \right]
$$

$$
\frac{\partial \mathbf{x}(\xi,\eta)}{\partial \xi} = \sum_{i=0}^{3} \left[\mathbf{x}_i \frac{\partial \mathcal{C}_i(\xi,\eta)}{\partial \xi} + \frac{\partial \mathbf{x}}{\partial \xi}\Big|_i \frac{\partial \mathcal{D}_i^{\xi}(\xi,\eta)}{\partial \xi} + \frac{\partial \mathbf{x}}{\partial \eta}\Big|_i \frac{\partial \mathcal{D}_i^{\eta}(\xi,\eta)}{\partial \xi} \right]
$$

$$
\frac{\partial \mathbf{x}(\xi,\eta)}{\partial \eta} = \sum_{i=0}^{3} \left[\mathbf{x}_i \frac{\partial \mathcal{C}_i(\xi,\eta)}{\partial \eta} + \frac{\partial \mathbf{x}}{\partial \xi}\Big|_i \frac{\partial \mathcal{D}_i^{\xi}(\xi,\eta)}{\partial \eta} + \frac{\partial \mathbf{x}}{\partial \eta}\Big|_i \frac{\partial \mathcal{D}_i^{\eta}(\xi,\eta)}{\partial \eta} \right] \quad (3.34)
$$

in which:

$$
\begin{aligned}
\mathcal{C}_0(\xi,\eta) &= 0.5\left[(1-\xi)H_0(\eta) + (1-\eta)H_0(\xi) - 0.5(1-\xi)(1-\eta)\right] \\
\mathcal{C}_1(\xi,\eta) &= 0.5\left[(1+\xi)H_0(\eta) + (1-\eta)H_1(\xi) - 0.5(1+\xi)(1-\eta)\right] \\
\mathcal{C}_2(\xi,\eta) &= 0.5\left[(1+\xi)H_1(\eta) + (1+\eta)H_1(\xi) - 0.5(1+\xi)(1+\eta)\right] \\
\mathcal{C}_3(\xi,\eta) &= 0.5\left[(1-\xi)H_1(\eta) + (1+\eta)H_0(\xi) - 0.5(1-\xi)(1+\eta)\right] \\
\mathcal{D}_0^{\xi}(\xi,\eta) &= 0.5(1-\eta)H_2(\xi) \\
\mathcal{D}_1^{\xi}(\xi,\eta) &= 0.5(1-\eta)H_3(\xi) \\
\mathcal{D}_2^{\xi}(\xi,\eta) &= 0.5(1+\eta)H_3(\xi) \\
\mathcal{D}_3^{\xi}(\xi,\eta) &= 0.5(1+\eta)H_2(\xi) \\
\mathcal{D}_0^{\eta}(\xi,\eta) &= 0.5(1-\xi)H_2(\eta) \\
\mathcal{D}_1^{\eta}(\xi,\eta) &= 0.5(1+\xi)H_2(\eta) \\
\mathcal{D}_2^{\eta}(\xi,\eta) &= 0.5(1+\xi)H_3(\eta) \\
\mathcal{D}_3^{\eta}(\xi,\eta) &= 0.5(1-\xi)H_3(\eta) \quad\quad\quad\quad\quad\quad\quad\quad\quad (3.35)
\end{aligned}
$$

$$
\begin{aligned}
\mathcal{C}_{0\xi}(\xi,\eta) &= 0.5\left[-H_0(\eta) + (1-\eta)H_0'(\xi) + 0.5(1-\eta)\right] \\
\mathcal{C}_{1\xi}(\xi,\eta) &= 0.5\left[+H_0(\eta) + (1-\eta)H_1'(\xi) - 0.5(1-\eta)\right] \\
\mathcal{C}_{2\xi}(\xi,\eta) &= 0.5\left[+H_1(\eta) + (1+\eta)H_1'(\xi) - 0.5(1+\eta)\right] \\
\mathcal{C}_{3\xi}(\xi,\eta) &= 0.5\left[-H_1(\eta) + (1+\eta)H_0'(\xi) + 0.5(1+\eta)\right] \\
\mathcal{D}_{0\xi}^{\xi}(\xi,\eta) &= 0.5(1-\eta)H_2'(\xi) \\
\mathcal{D}_{1\xi}^{\xi}(\xi,\eta) &= 0.5(1-\eta)H_3'(\xi) \\
\mathcal{D}_{2\xi}^{\xi}(\xi,\eta) &= 0.5(1+\eta)H_3'(\xi) \\
\mathcal{D}_{3\xi}^{\xi}(\xi,\eta) &= 0.5(1+\eta)H_2'(\xi) \\
\mathcal{D}_{0\xi}^{\eta}(\xi,\eta) &= -0.5H_2(\eta) \\
\mathcal{D}_{1\xi}^{\eta}(\xi,\eta) &= +0.5H_2(\eta) \\
\mathcal{D}_{2\xi}^{\eta}(\xi,\eta) &= +0.5H_3(\eta) \\
\mathcal{D}_{3\xi}^{\eta}(\xi,\eta) &= -0.5H_3(\eta)
\end{aligned}
\tag{3.36}
$$

$$
\begin{aligned}
\mathcal{C}_{0\eta}(\xi,\eta) &= 0.5\left[(1-\xi)H_0'(\eta) - H_0(\xi) + 0.5(1-\xi)\right] \\
\mathcal{C}_{1\eta}(\xi,\eta) &= 0.5\left[(1+\xi)H_0'(\eta) - H_1(\xi) + 0.5(1+\xi)\right] \\
\mathcal{C}_{2\eta}(\xi,\eta) &= 0.5\left[(1+\xi)H_1'(\eta) + H_1(\xi) - 0.5(1+\xi)\right] \\
\mathcal{C}_{3\eta}(\xi,\eta) &= 0.5\left[(1-\xi)H_1'(\eta) + H_0(\xi) - 0.5(1-\xi)\right] \\
\mathcal{D}_{0\eta}^{\xi}(\xi,\eta) &= -0.5H_2(\xi) \\
\mathcal{D}_{1\eta}^{\xi}(\xi,\eta) &= -0.5H_3(\xi) \\
\mathcal{D}_{2\eta}^{\xi}(\xi,\eta) &= +0.5H_3(\xi) \\
\mathcal{D}_{3\eta}^{\xi}(\xi,\eta) &= +0.5H_2(\xi) \\
\mathcal{D}_{0\eta}^{\eta}(\xi,\eta) &= 0.5(1-\xi)H_2'(\eta) \\
\mathcal{D}_{1\eta}^{\eta}(\xi,\eta) &= 0.5(1+\xi)H_2'(\eta) \\
\mathcal{D}_{2\eta}^{\eta}(\xi,\eta) &= 0.5(1+\xi)H_3'(\eta) \\
\mathcal{D}_{3\eta}^{\eta}(\xi,\eta) &= 0.5(1-\xi)H_3'(\eta)
\end{aligned}
\tag{3.37}
$$

3.2.2 The numerical solution

The boundary of the problem, Γ is then discretized in N_{el} patches. Using the representation in Eq.(3.34) for both the geometry and the unknowns $\tilde{\varphi}(\mathbf{y})$, and applying the collocation method on the nodal values of the discretized geometry, we can rewrite Eq.(2.10) as a linear combination of the four nodal values and of the eight nodal derivatives in ξ and η as:

$$
\begin{aligned}
E(\mathbf{y})\,\tilde{\varphi}(\mathbf{y}_j) \;=\; & \sum_{i=0}^{N_{el}} \int_{\Gamma_i} G_0(\xi,\eta)\Psi_i(\xi,\eta)J(\xi,\eta)e^{-s\theta}\mathrm{d}\Gamma \\
& - \sum_{i=0}^{N_{el}} \int_{\Gamma_i} \frac{\partial G_0(\xi,\eta)}{\partial n}\Phi_i(\xi,\eta)J(\xi,\eta)e^{-s\theta}\mathrm{d}\Gamma \\
& + s\sum_{i=0}^{N_{el}} \int_{\Gamma_i} G_0(\xi,\eta)\Phi_i(\xi,\eta)\frac{\partial\theta(\xi,\eta)}{\partial n}J(\xi,\eta)e^{-s\theta}\mathrm{d}\Gamma \quad (3.38)
\end{aligned}
$$

in which $\Psi_i(\xi,\eta)$ and $\Phi_i(\xi,\eta)$ are the Coons+Hermite interpolation expressions, given in Eq.(3.34), on the element i of $\frac{\partial\tilde{\varphi}}{\partial n}$ and $\tilde{\varphi}$ respectively and $J(\xi,\eta)$ is the jacobian of the transformation of coordinates.

3.2.3 Finite differences approach

In this approach the nodal derivatives have been evaluated, after the discretization of the boundary domain, with a finite difference algorithm, reducing the dependency of the system only to the nodal values. Eq.(3.38) can then be rewritten as:

$$
\begin{aligned}
E\,\tilde{\varphi}_j \;=\; & \sum_{i=0}^{N_{el}}\sum_{j=0}^{M} \chi_j \int_{\Gamma_i} G_0(\xi,\eta)J(\xi,\eta)e^{-s\theta}\mathrm{d}\Gamma \\
& - \sum_{i=0}^{N_{el}}\sum_{j=0}^{M} \tilde{\varphi}_j \int_{\Gamma_i} \frac{\partial G_0(\xi,\eta)}{\partial n}J(\xi,\eta)e^{-s\theta}\mathrm{d}\Gamma \\
& + s\sum_{i=0}^{N_{el}}\sum_{j=0}^{M} \tilde{\varphi}_j \int_{\Gamma_i} G_0(\xi,\eta)\frac{\partial\theta(\xi,\eta)}{\partial n}J(\xi,\eta)e^{-s\theta}\mathrm{d}\Gamma \\
\;=\; & \sum_{i=0}^{N_{el}}\sum_{j=0}^{M} (B_{ij}\chi_j - C_{ij}\tilde{\varphi}_j + sD_{ij}\tilde{\varphi}_j) \quad (3.39)
\end{aligned}
$$

or in a more compact form:

$$\frac{1}{2}\tilde{\varphi} = \mathbf{B}\chi + (s\mathbf{D} - \mathbf{C})\tilde{\varphi} \tag{3.40}$$

which is a linear system of equations in the unknowns $\tilde{\varphi}$.

It must be noted that, depending on the finite difference schema chosen for the nodal derivatives, the nodal value of the unknown appears in the representation as multiplier of the integral coefficients over adjacent patches of the discretization both for the nodal contribution, for Hermite polynomials $H_0(\xi)$ and $H_1(\xi)$, and for the contribution as a coefficient of the discrete derivative, for Hermite polynomials $H_2(\xi)$ and $H_3(\xi)$. In Fig.3.16 we reported the patches "influenced" by a nodal value when the nodal derivatives are evaluated with a centered finite difference schema:

$$f_\xi(\xi) = \frac{f(\xi + h) - f(\xi - h)}{2h} \tag{3.41}$$
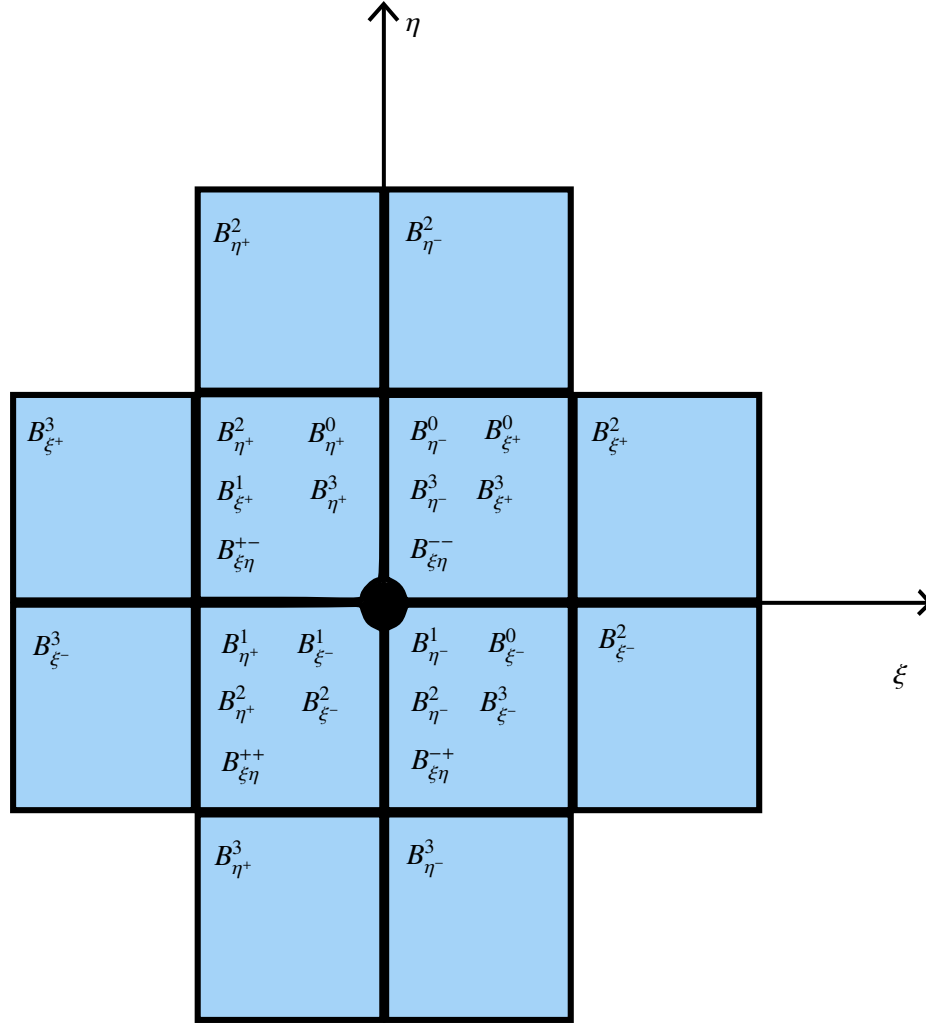
Figure 3.16: Influence of a nodal value over the patches when the nodal derivative is evaluated with a centered schema

3.2.3.1 Results and discussion

3.2.3.1.1 Planar wave on a sphere The formulation presented is applied to a simple acoustic case study for which the analytical solution is known (see *e.g.*, Morse and Ingard [17] or Appendix B). Specifically, we consider the simple case of a plane wave of amplitude $\tilde{\varphi}_0$ impinging on a unit sphere. Indicating with $\mathbf{k}$ the

wave vector, the incident field is given by $\tilde{\varphi}_p = \tilde{\varphi}_0 e^{i\,\mathbf{k}\cdot\mathbf{r}}$.
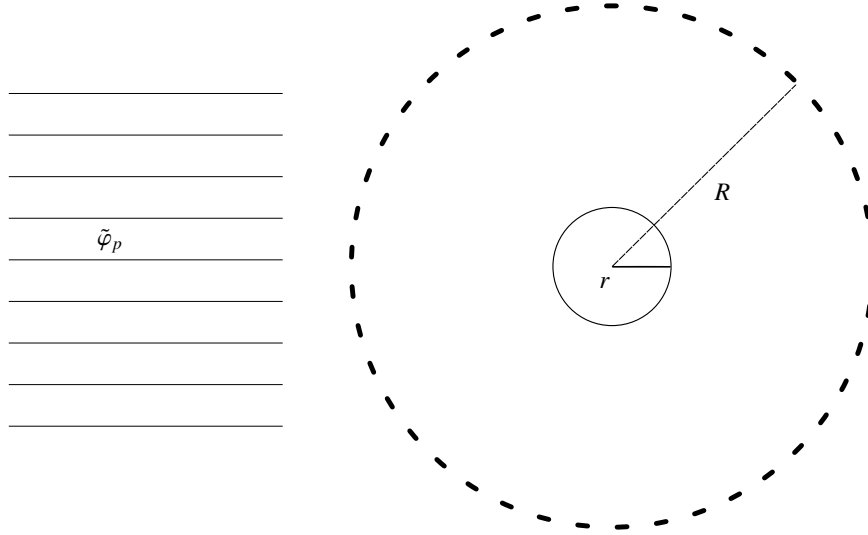
Figure 3.17: 3D Hermite Coons: Planar wave impinging on a unit sphere

In Figure 3.18 we reported the value of $|\tilde{\varphi}|$ at $R = 5r$ for $f = 200$Hz and in Figure 3.19 for $f = 500$Hz compared with the analytical solution.
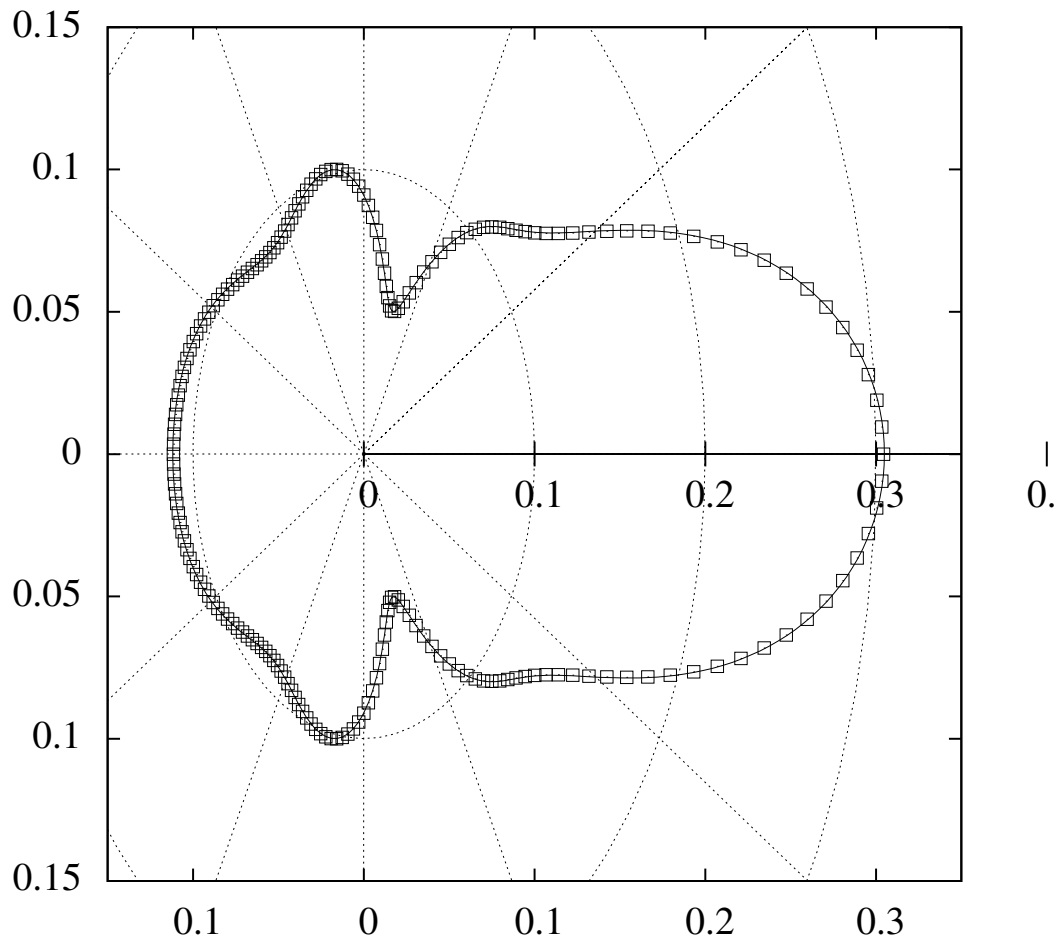
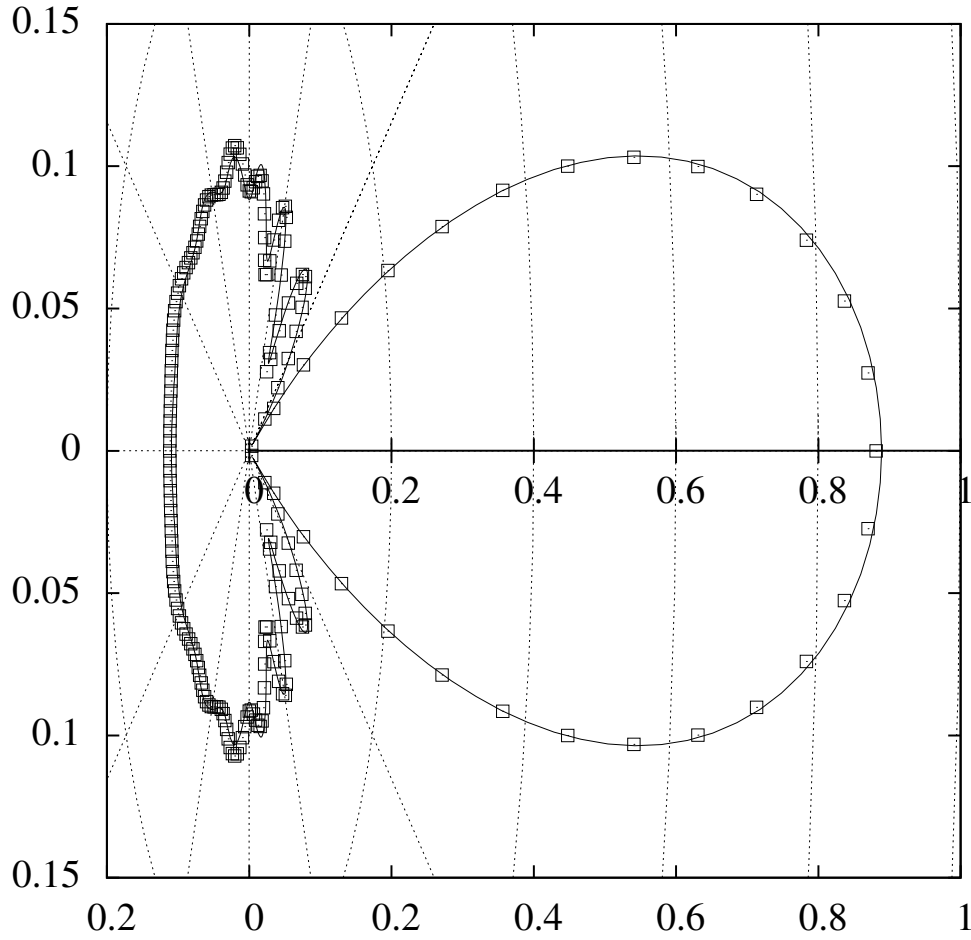Figure 3.18: *3D* Hermite Coons: Absolute scattering pressure, $f = 200$Hz, $(-)$ analytical, $(\square)$ BEM, $N_{el} = 32 \times 32$

Figure 3.19: $3D$ Hermite Coons: Absolute scattering pressure, $f = 500$Hz, $(-)$ analytical, $(\square)$ BEM, $N_{el} = 32 \times 32$

3.2.3.1.2 Numerical convergence analysis   In order to evaluate the rate of convergence of the proposed formulation we evaluated the Lebesgue norm of order 2 of the local relative difference $\|(\tilde{\varphi} - \tilde{\varphi}_a)/\tilde{\varphi}_a\|$:

$$\epsilon = \sqrt{\int_{\mathcal{S}} \left\| \frac{\tilde{\varphi} - \tilde{\varphi}_a}{\tilde{\varphi}_a} \right\|^2 d\mathcal{S}} \tag{3.42}$$

in which $\tilde{\varphi}_a$ is the analytical solution. We also evaluated the relative error of the maximum value of $\tilde{\varphi}$, $\|\max(\varphi_s) - \max(\varphi_a)\|$ evaluated on the surface of the sphere.
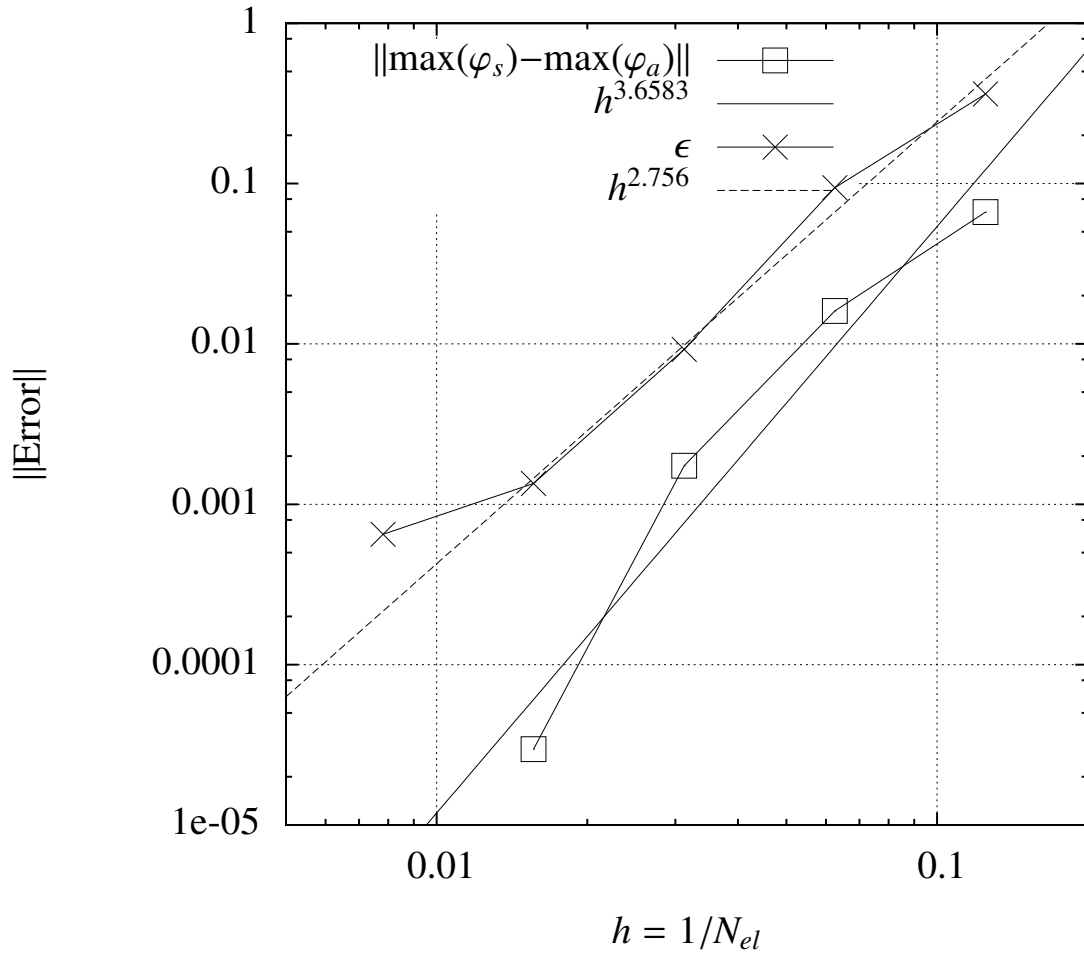
41

Figure 3.20: 3D Hermite Coons: Convergence analysis at $f = 200$Hz, ($\square$) $\|\max(\varphi_s) - \max(\varphi_a)\|$, ($-$) $x^{3.6583}$, ($\times$) ϵ, ($--$) $x^{2.756}$
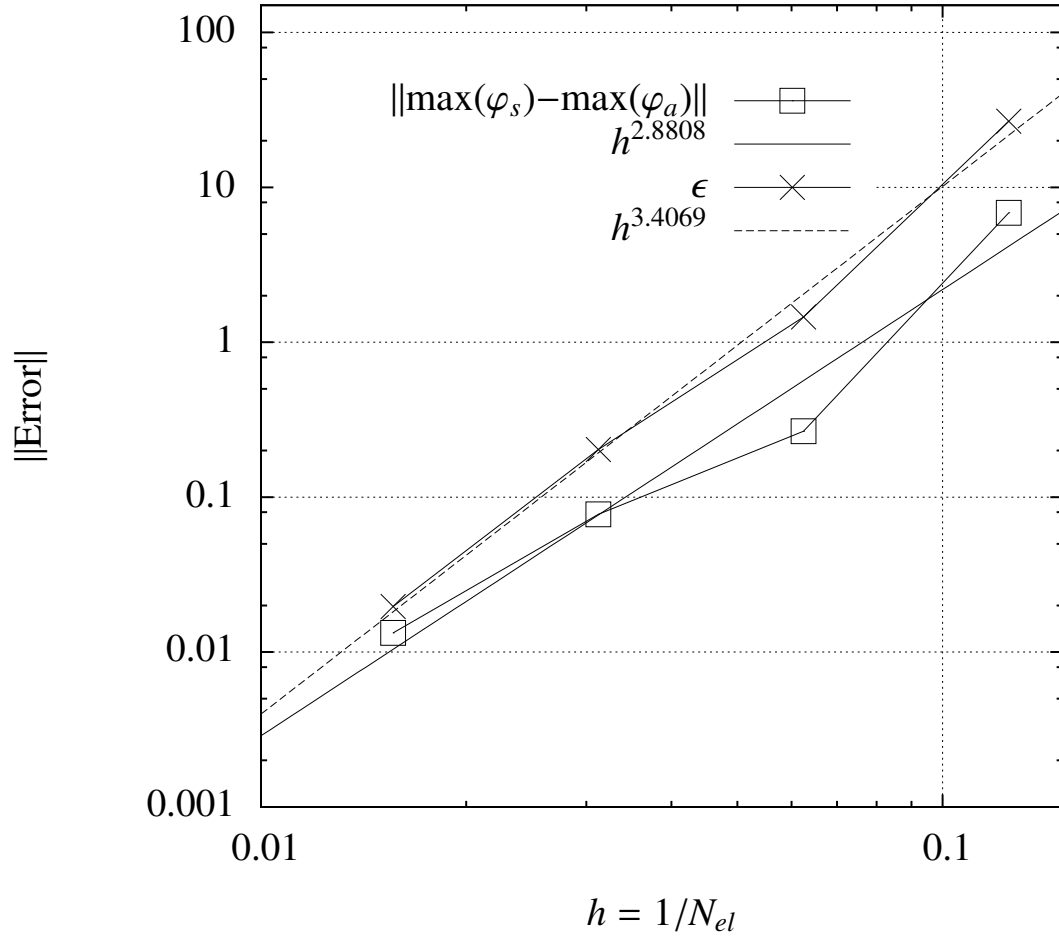
Figure 3.21: $3D$ Hermite Coons: Convergence analysis at $f = 500$Hz, $(\square)$ $\|\max(\varphi_s){-}\max(\varphi_a)\|$, $(-)$ $x^{2.8808}$, $(\times)$ ϵ, $(--)$ $x^{3.4069}$

The convergence rates are reported in Table 3.3.

Table 3.3: $3D$ Hermite Coons: Hermite Coons approach: Convergence Rate at $f = 200$Hz and $f = 500$Hz

Method	$f = 200$Hz	$f = 500$Hz
$\|\max(\varphi_s){-}\max(\varphi_a)\|$	3.6583	2.8808
ϵ	2.756	3.4069

3.2.4 Dual approach

In the previous approach the nodal derivatives in 3.34 are evaluated with a finite difference scheme, hence including in the vector of the unknowns only the nodal values. By applying the same technique used in Chapter 3.1 we can take into account the tangential gradient of the Kirchhoff–Helmholtz equation:

$$\nabla_t^{\mathbf{y}}\left[E(\mathbf{y})\varphi(\mathbf{y})\right] \;=\; \nabla_t^{\mathbf{y}} \oint_{\mathcal{S}}\left(G\frac{\partial\varphi}{\partial n} - \varphi\frac{\partial G}{\partial n}\right) d\mathcal{S}(\mathbf{x}) \tag{3.43}$$

where

$$\nabla_t \bullet = \nabla \bullet - \frac{\partial \bullet}{\partial n} \tag{3.44}$$

Following the procedure described in [8] we can rewrite equation 3.43 as:

$$E(\mathbf{y})\varphi(\mathbf{y}) \;=\; \oint_{\mathcal{S}}\left(G\frac{\partial\varphi}{\partial n} - \varphi\frac{\partial G}{\partial n}\right) d\mathcal{S} \tag{3.45}$$

$$E(\mathbf{y})\mathbf{v}_\alpha(\mathbf{y}) \;=\; \oint_{\mathcal{S}}\left(-\frac{\partial G}{\partial x^\alpha}\frac{\partial\varphi}{\partial n} - G[\nabla_t \mathbf{n}]\nabla_t\varphi \cdot \mathbf{g}_\alpha - \frac{\partial G}{\partial n}\frac{\partial\varphi}{\partial x^\alpha}\right) d\mathcal{S} \quad \alpha = 1,2$$

where

$$\mathbf{v}_\alpha = \frac{\partial\varphi}{\partial x^\alpha} \tag{3.46}$$

and $\mathbf{g}_\alpha$ is the covariant base in the chosen system of coordinates. By expressing the unknowns in equation 3.45 with a Hermite Coons representation and by collocating in the nodal point, we arrive at the system of equations:

$$\frac{1}{2}\mathbf{I}\Phi = \mathbf{B}\Psi + \mathbf{C}\Phi \tag{3.47}$$

in which:

$$\mathbf{B} = \begin{bmatrix} \mathbf{GC} & \mathbf{GD}^\xi & \mathbf{GD}^\eta \\ \overline{\mathbf{G}_\xi\mathbf{C}} & \overline{\mathbf{G}_\xi\mathbf{D}^\xi} & \overline{\mathbf{G}_\xi\mathbf{D}^\eta} \\ \overline{\mathbf{G}_\eta\mathbf{C}} & \overline{\mathbf{G}_\eta\mathbf{D}^\xi} & \overline{\mathbf{G}_\eta\mathbf{D}^\eta} \end{bmatrix} \tag{3.48}$$

$$\mathbf{C} = \begin{bmatrix} \mathbf{G_nC} & \mathbf{G_nD}^\xi & \mathbf{G_nD}^\eta \\ \overline{\mathbf{HC}_\xi + \mathbf{KC}\eta} & \overline{\mathbf{HD}_\eta^\xi + \mathbf{KD}_\eta^\xi} & \overline{\mathbf{HKD}_\xi^\eta + \mathbf{KD}_\eta^\eta} \\ \overline{\mathbf{MC}_\xi + \mathbf{NC}\eta} & \overline{\mathbf{MD}_\eta^\xi + \mathbf{ND}_\eta^\xi} & \overline{\mathbf{MD}_\xi^\eta + \mathbf{ND}_\eta^\eta} \end{bmatrix} \tag{3.49}$$

where the elements of the matrices are detailed in appendix E and

$$
\Psi = \begin{bmatrix} \chi_i \\[4pt] \dfrac{\partial \chi}{\partial \xi}\Big|_i \\[8pt] \dfrac{\partial \chi}{\partial \eta}\Big|_i \end{bmatrix}
\quad
\Phi = \begin{bmatrix} \varphi_i \\[4pt] \dfrac{\partial \varphi}{\partial \xi}\Big|_i \\[8pt] \dfrac{\partial \varphi}{\partial \eta}\Big|_i \end{bmatrix}
\tag{3.50}
$$

are the vectors containing the nodal values and their derivatives. The nodal derivatives of φ are, in this case considered as unknowns.

Chapter 4

Global Methods

> C: I'm a simple man, Hobbes.
> H: You?? Yesterday you wanted a nuclear powered car
> that could turn into a jet with laser-guided heat–seeking
> missiles!.
> C: I'm a simple man with complex tastes.
>
> C and H

4.1 NURBS introduction

The acronym NURBS stands for Non-Uniform Rational B-Splines and their general
form is:

$$f(u) = \sum_{i=1}^{N} \frac{N_{i,p}(u)W_i q_i}{N_{i,p}(u)W_i} \qquad u \in [0,1] \tag{4.1}$$

In which the Basis function $N_{a,p}(\xi)$, of order p, are defined in a recursive way as:

$$N_{i,p}(u) = \frac{u - u_i}{u_{i+p} - u_i} N_{i,p-1}(u) + \frac{u_{i+p+1} - u}{u_{i+p+1} - u_{i+1}} N_{i+1,p-1}(u) \tag{4.2}$$

with

$$N_{i,0}(u) = \begin{cases} 1 & \text{if} \quad u_i \leq u < u_{i+1} \\ 0 & \text{otherwise} \end{cases} \tag{4.3}$$

The points q_i are called *control points* and the quantities W_i are the weights of
the NURBS. The set of abscissae u_i needed to fully define the basis functions forms

the *knot vector*. If the knot vector has $p + 1$ elements repeated at its beginning and at its end, it is called an *open* knot vector. In general, for a NURBS curve the following two properties hold:

1. if a knot u_i is repeated k times, the continuity of the curve at that point is C^{p-k}.

2. if the curve is C^0 at a point, the control point belongs to the curve.

As a consequence, for a given open knot vector the resulting NURBS passes through the first and last control points. Eq.(4.1) can be written as

$$f(u) = \sum_{i=1}^{N} R_{i,p}(u)q_i \quad u \in [0,1] \tag{4.4}$$

with

$$R_{i,p}(u) = \frac{N_{i,p}(u)W_i q_i}{\sum_{i=1}^{n} N_{i,p}(u)W_i} \tag{4.5}$$

$$R_{i,p}(\xi) \quad i = 5$$
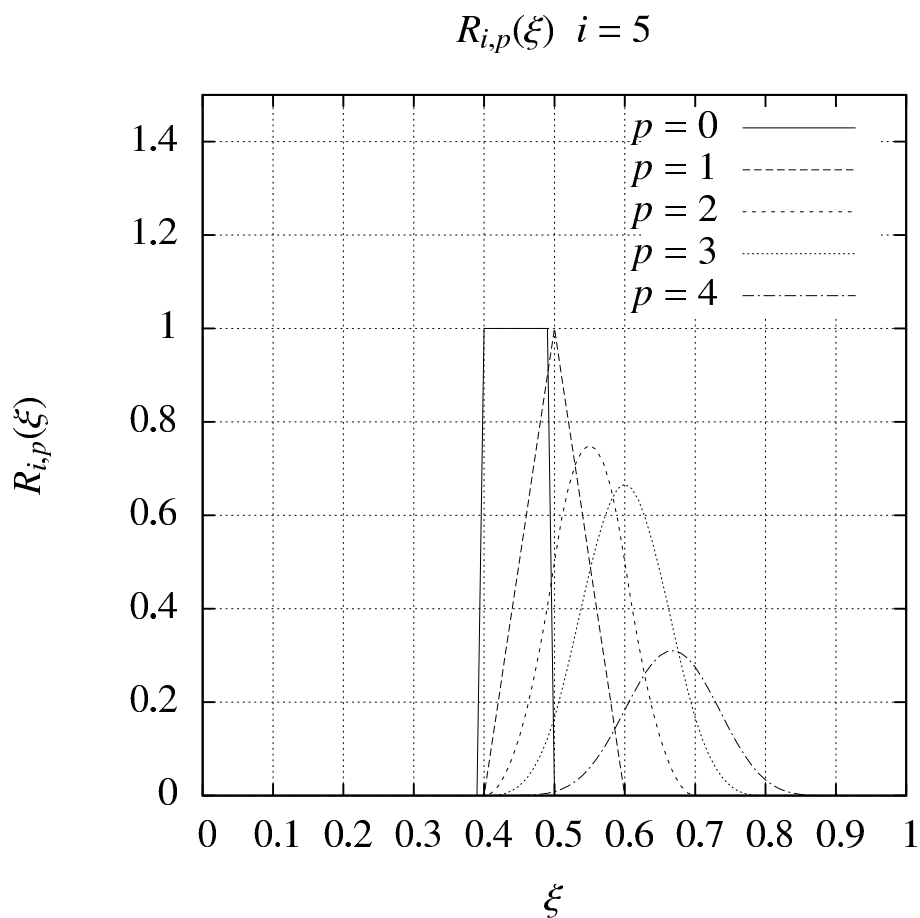
Figure 4.1: NURBS:Function $R_{i,p}(u)$ for $u_i = 0.5$ and $0 \leq p \leq 5$.

The function $R_{i,p}(u)$ for $u_i = 0.5$ and $0 \leq p \leq 5$ is depicted in Fig. 1, whereas Fig. 2 shows the complete basis in $u \in [0, 1]$, for $p = 2$.
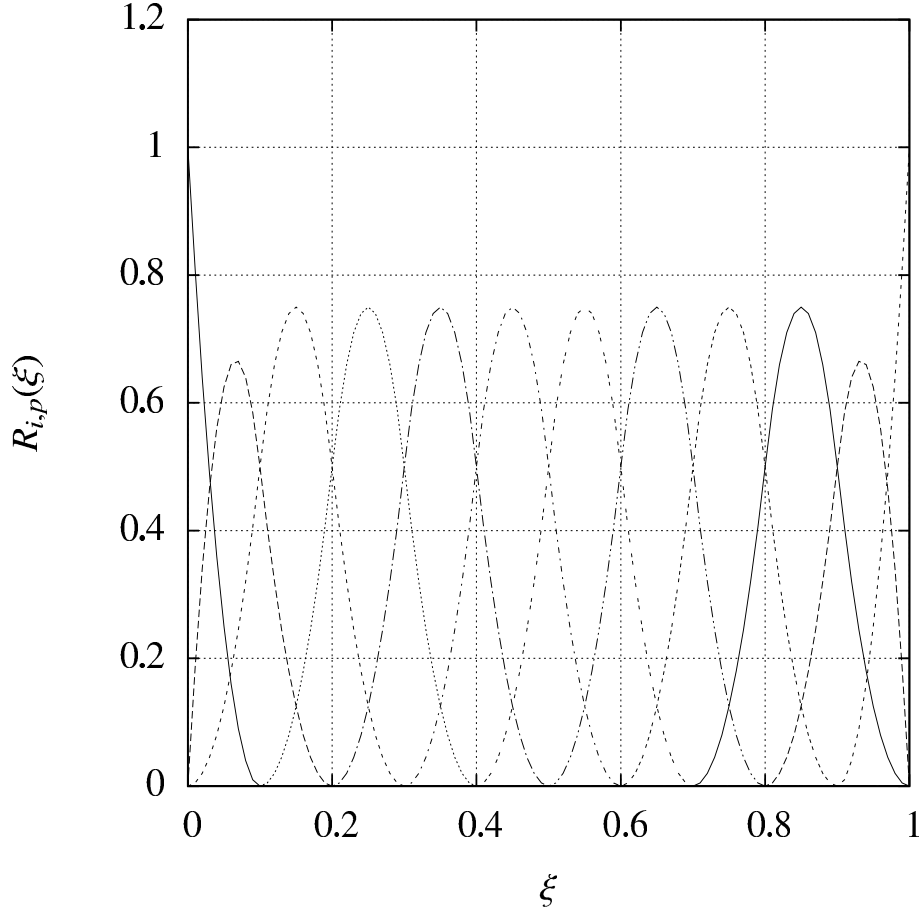
Figure 4.2: NURBS basis for $p = 2$.

On the basis of equation (4.1) to (4.5) the NURBS representation of $\tilde{\varphi}$ has the form

$$\tilde{\varphi}(u) = \sum_{i=1}^{N} R_{i,p}(u)q_i \tag{4.6}$$

with coefficients q_i and basis functions as reported in Eq.(4.5). Applying Eq.(4.6) to the RHS of Eq.(2.10), and limiting, for the sake of simplicity, the notation to the two–dimensional case, we obtain

$$E(\mathbf{y})\tilde{\varphi}(\mathbf{y}) = b(\mathbf{y}) - \sum_{i=1}^{N} q_i \oint_{\Gamma} \frac{\partial G(u, \mathbf{y})}{\partial n} R_{i,p}(u)J(u)du \tag{4.7}$$

where $J(u)$ is the Jacobian of the transformation from the physical space coordinate $\mathbf{x}$ to the NURBS parametric space one u. It is worth noting that the integrals

49

in Eq.(4.7) span the whole boundary. Indeed, the use of the global NURBS representation makes the concept of surface elements no longer required for the numerical solution of Eq.(4.7) and thus the partition of Γ is not strictly needed. On the other hand, the integrals in Eq.(4.7) must be accurately evaluated and, unless we have an analytical solution for them (and this could happen for very simple geometries and/or boundary conditions), a suitable numerical integration strategy must be identified. To this aim, a possible solution for complex geometries and/or boundary conditions could be the partition of the boundary into macro patches on which suitable quadrature formulas can be easily applied. However, it is important to notice that this partitioning, if needed, would have nothing to do with the number of unknowns of the solving linear system, but only with the proper evaluation of the integrals in Eq.(4.7). In Appendix D the effects of the partition of Γ on the convergence of the integrals in Eq.(4.7) is analyzed for two different geometries.

4.2 NURBS and BEM

In this case we will consider, as a starting point, the weight W_a to be unitary, i.e: $W_a = 1 \quad a = 1, \ldots n$. If we apply the representation (4.1) to Eq.(2.10), we arrive at Eq.(4.15) in which now we know the quantities $\tilde{\varphi}_a$ and $\tilde{\chi}_a$ to be the control points of the velocity potential and of the normal wash. In order to apply the representation (3.5) to be valid we need a set $\xi_k \quad k = 1, \ldots, n$ of abscissae to apply the collocation method on. We must choose the abscissae in such a way that the collocation point, i.e the values of:

$$\mathbf{x}(\xi_k) = \sum_{a=1}^{n} \frac{N_{a,p}(\xi_k) W_a \tilde{x}_a}{N_{a,p}(\xi_k) W_a} \tag{4.8}$$

lay exactly on the boundary $\partial \mathcal{S}$ of the domain. To ensure this we can adopt two different approaches that will be described in the following chapters.

4.3 Reconstructing abscissae from geometry discretisation

We discretise the domain $\partial \mathcal{S}$ in N_{el} elements and $n = N_{el}+1$ nodes $\{x_k, \quad k = \ldots, n\}$. The representation (4.13) applies for a set of abscissae $\{\xi_k \quad k = 1, \ldots, n\}$ and a set of control points $\{\tilde{x}_a \quad a = 1, \ldots, n\}$. In order to find the control points for the NURBS representation (4.13), we choose an initial set ξ_k' in the parameter space with a one of the common methodologies, described in Appendix (A). It must be noted that the abscissae ξ_k' do not give us the representation in the original nodal points but are used only to allow us to obtain the control points $\tilde{x}_a$. Evaluating (4.13) in the abscissae ξ_k', gives us the linear system:

$$\mathbf{x} = \mathbf{R}\tilde{\mathbf{x}} \tag{4.9}$$

in which $\mathbf{x}$ are the original collocation points, $\tilde{\mathbf{x}}$ are the control points of the NURBS representation and R is the matrix:

$$\mathbf{R} = \begin{pmatrix} R_{1,p}(\xi_0') & R_{2,p}(\xi_0') & \ldots & R_{n,p}(\xi_0') \\ R_{1,p}(\xi_1') & R_{2,p}(\xi_1') & \ldots & R_{n,p}(\xi_1') \\ \vdots & \vdots & \vdots & \vdots \\ R_{1,p}(\xi_n') & R_{2,p}(\xi_n') & \ldots & R_{n,p}(\xi_n') \end{pmatrix} \tag{4.10}$$

being

$$R_{a,p} = \frac{N_{a,p}(\xi_k)W_a}{\sum_{a=1}^{n} N_{a,p}(\xi_k)W_a} \tag{4.11}$$

for a given distribution of weights W_a, Eq.(4.9) solution gives us the desired control points of the geometry:

$$\tilde{\mathbf{x}} = R^{-1}\mathbf{x} \tag{4.12}$$

Knowing the control points, we can now apply a bisection method to obtain the values ξ_k in which the representation in Eq.(4.13) gives us the original collocation points.

4.4 The numerical solution

The numerical solution of Eq.(4.7) can be obtained using the collocation method, with collocation points lying on the boundary Γ. To this aim, it is necessary

to identify a set of collocation points $\mathbf{y}_k \in \Gamma$. In the present approach, this requires the identification of a set of abscissae u_k in the NURBS parametric space corresponding to points on Γ in the physical space through the relationship

$$\boldsymbol{y}(u_k) = \sum_{i=1}^{N} R_{i,p}(u_k)\boldsymbol{\eta}_i \tag{4.13}$$

where n is the number of the control points $\boldsymbol{\eta}_i$ used to build the NURBS reproducing the geometry of Γ. To ensure that $\mathbf{y}(u_k)$ is located on the boundary, the abscissa u_k must be chosen according to the Greville distribution [12, 21]

$$u'_k = \frac{u_{i+1} + u_{i+2} + \ldots + u_{i+p}}{p}, \quad i = 1, \ldots, n-1 \tag{4.14}$$

The abscissae u'_k satisfying Eq.(4.14) correspond to points in the physical space such that $\mathbf{y}(u') \in \Gamma$ (see Fig. 3). A key aspect in the numerical evaluation of the integrals in Eq.(4.7) is the management of the singularities of the kernels arising from the collocation of the observation point $\mathbf{y}$ on the boundary. In this respect, the meshless approach presents a significant advantage with respect to the classic BEM, being now the integration extended to the whole boundary or, for complex geometries, to a part of it significantly larger than a single boundary element. As a consequence, the check for singularity occurrence (not a straightforward task with NURBS) is less critical, or even not required at all, thus simplifying the numerical integration procedure. The asymptotic behavior of the integral appearing in Eq.(2.10) is briefly recalled in Appendix D for the sake of clarity and completeness. Once that the location of the collocation points is fixed using the Greville abscissae we can apply the same decomposition given in Eq.(4.6) to the left hand side of Eq.(4.7). For $\mathbf{y} \in \Gamma$ we obtain

$$\frac{1}{2}\mathsf{R}\,\mathsf{q} = \mathbf{B} - \mathbf{C}\,\mathsf{q} \tag{4.15}$$

where the elements of $\mathbf{B}$ and $\mathbf{C}$ have the form

$$B_j = \oint_\Gamma G(\mathbf{x}, \mathbf{y}_j)\frac{\partial \varphi}{\partial n}d\Gamma, \quad C_{ij} = \oint_\Gamma \frac{\partial G(u, \mathbf{y}_j)}{\partial n}R_{i,p}(u)J(u)du \tag{4.16}$$

where $u \in [0, 1]$. The entries of the $N \times N$ matrix R have the form $\mathsf{R}_{ij} = R_{i,p}(u'_j)$. The final form of the linear system is $(0.5\,\mathbf{R} + \mathbf{C})\,\mathsf{q} = \mathbf{B}$, which can be solved using the most appropriate solver.

4.4.1   Knots *h*-refinement

In the derivation performed so far we assumed, without loss of generality, unit weights in Eq.(4.5). This choice is certainly not optimal for the representation of complex functions, but is the only possible to easily represent the unknowns. Indeed, for a generic function $\tilde{\varphi}$ could be possible, in principle, identify an optimal set of weights and control points capable to achieve a high level of accuracy with a limited number of degrees of freedom. In actual applications, this can be easily done to represent regular geometries (for example, simple geometries of the boundary Γ). On the contrary, in complex phenomena, the optimal representation of the unknown $\tilde{\varphi}$ could not be an easy task. As an example, consider a domain bounded a circle. It can be represented exactly with the six control points depicted by squares in Fig.4.3, provided that the vectors of the corresponding weights and nodes are $\mathsf{W}_c^T = \{1\ 0.5\ 0.5\ 1\ 0.5\ 0.5\ 1\}$ and $\mathsf{u}_c^T = \{0\ 0\ 0\ 0.25\ 0.5\ 0.5\ 0.75\ 1\ 1\ 1\}$, respectively (see, *e.g.*, Piegl[18]).
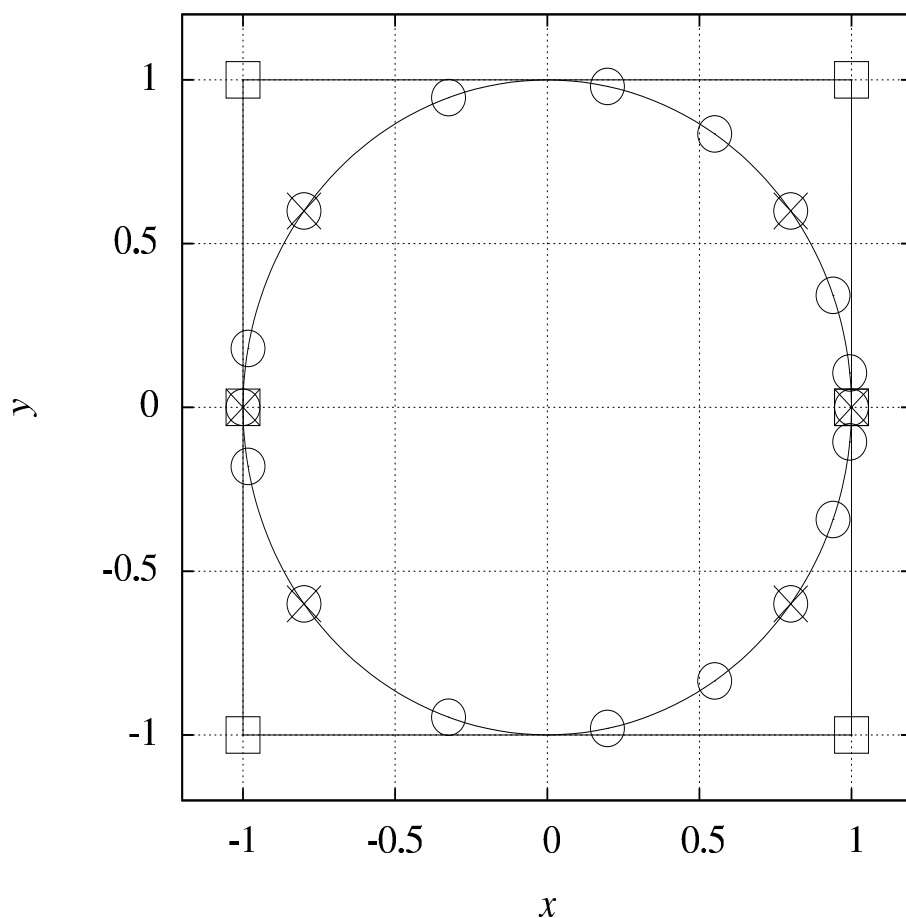
Figure 4.3: NURBS Circle, (□) Control points, (×) Greville's abscissae in the physical space, (○) refined Greville's abscissae in the physical space.

On the other hand, the physical phenomenon described by the function $\tilde{\varphi}$ can be extremely complex, even if the boundary of the domain is so simple. If, for example, we are dealing with the scattering of an acoustic wave impinging on the circle at medium–high frequencies, W_c and u_c are clearly not suitable to reproduce accurately the scattering pattern. In order to increase the number of collocation points for the numerical solution of the BIE, starting from the NURBS optimal representation of Γ, the h-refinement technique is used. With the h-refinement technique, the non-zero intervals between the components of the knot vector u_c are refined with equally spaced knots. The number of inserted knots doesn't need to be the same for each interval, and thus the NURBS representation can

be enriched only where needed. These new knots become the control points of the representation of the unknown $\tilde{\varphi}$. The refinement obtained using an uneven distribution of knots in the different intervals is depicted in Fig.4.3 ($\circ$), along with the original knot vector ($\times$).

4.5 Results and discussion

The formulation presented is applied to two different problems: the solution of an incompressible, two–dimensional potential flow around an impermeable, non–lifting body, and the scattering of a sound–hard circular cylinder impinged by a planar wave. The present section reports the results obtained and their validation against available analytical solutions. The convergence analysis of the numerical error with respect to the number N of degrees of freedom of the system is also included.

4.5.1 Incompressible potential aerodynamics

In the first application, the function $\tilde{\varphi}$ has the physical meaning of a velocity potential such that $\mathbf{v} = \nabla \tilde{\varphi}$, being $\mathbf{v}$ the velocity field associated with the irrotational flow of an inviscid fluid. Such a flow is governed by the Laplace equation $\nabla^2 \tilde{\varphi} = 0$. Consider an impermeable, blunt body immersed within a main flow at speed $\mathbf{v}_0$. The velocity field is given by the superposition of the main stream velocity and the perturbation $\mathbf{v}'$ induced by the obstacle. The fundamental solution of the problem and its normal derivative on Γ are

$$G(\mathbf{x}, \mathbf{y}) = -\frac{1}{2\pi} \ln r, \;\; \frac{\partial G}{\partial n} = -\frac{1}{2\pi} \frac{\mathbf{r} \cdot \mathbf{n}}{r^2} \qquad (4.17)$$

where $r = \|\mathbf{x} - \mathbf{y}\|$. The analytical solution $\tilde{\varphi}_a$ exists if the impermeable obstacle is a circular cylinder of radius R. In polar coordinates, it reads $\tilde{\varphi}_a = v_0 r \left(1 + R^2/r^2\right) cos(\theta)$. Figure 4.4 shows the comparison of the numerical solution of the present method, $\tilde{\varphi}$, with the analytical solution $\tilde{\varphi}_a$.
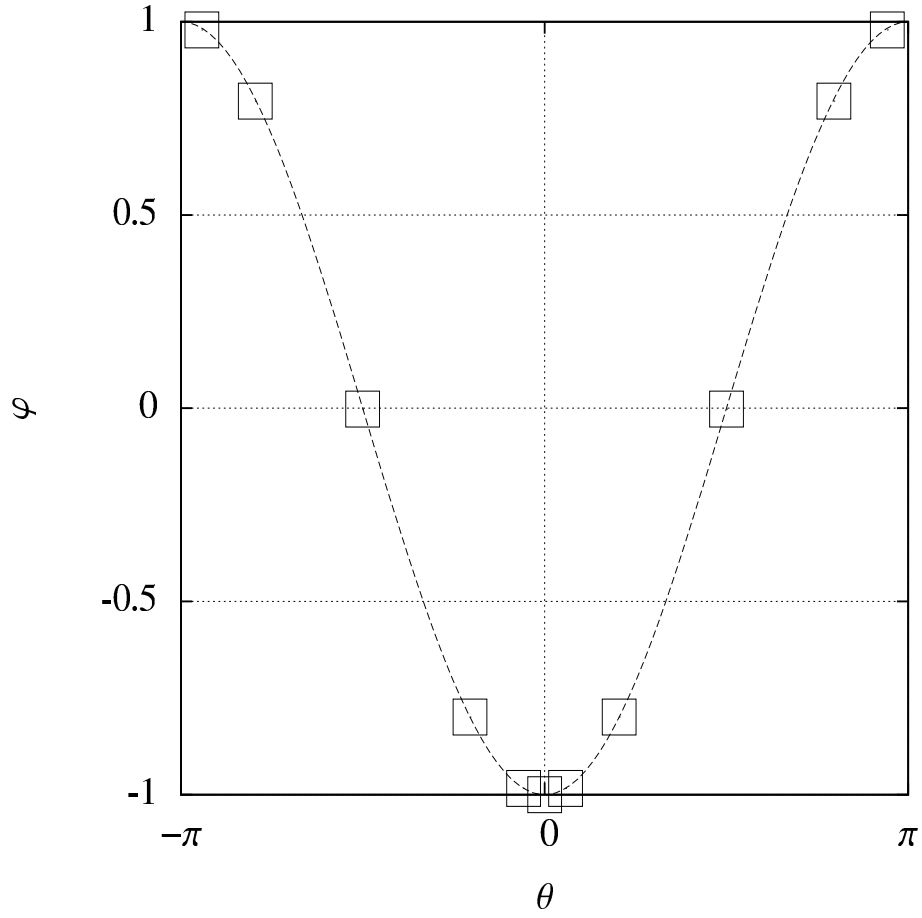
Figure 4.4: Velocity potential $\tilde{\varphi}$ for a uniform flow U_∞ in x-direction. $(-)$ Analytical solution. $(\square)$ BIE-NURBS. $p = 3$

The convergence of the global error ϵ, defined as

$$\epsilon = \sqrt{\int_\Gamma \left\| \frac{\tilde{\varphi} - \tilde{\varphi}_a}{\tilde{\varphi}_a} \right\|^2 d\Gamma} \tag{4.18}$$

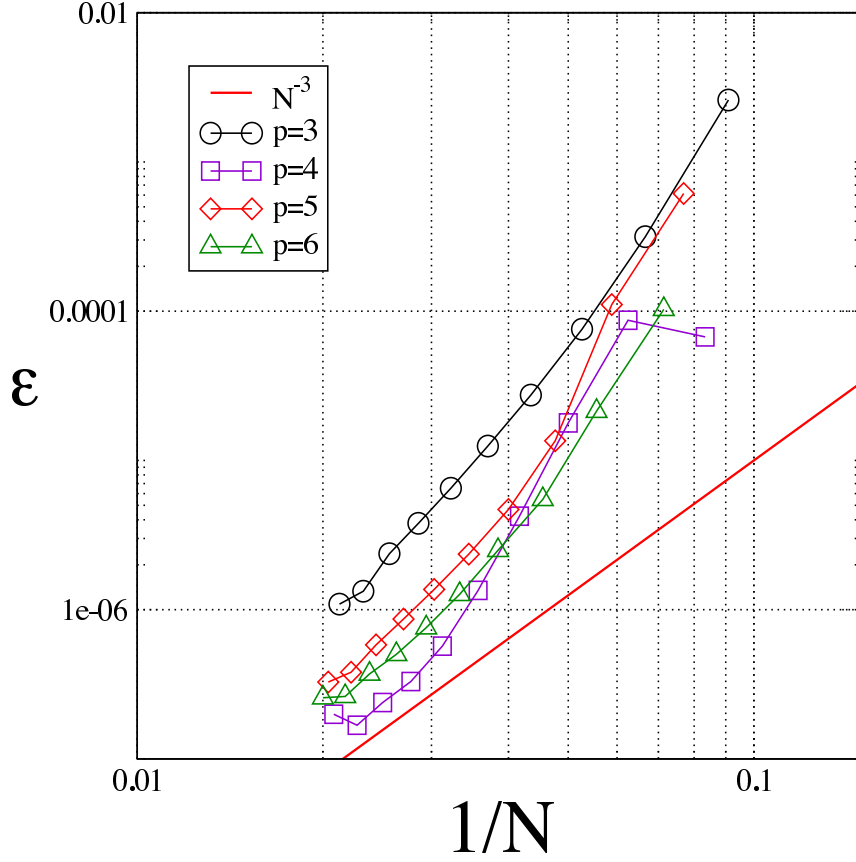is presented in Figure 4.5 as a function of $1/N$ for different values of the the degree of the NURBS representation.

Figure 4.5: Convergence of ϵ for the solution of potential incompressible aerodynamics.

What can be observed first, is that the convergence curves are non linear in the log/log plane, and, consistently with the use of a rational function basis, the rate of convergence cannot be inferred directly from the order p of the NURBS. The rate of convergence is slightly higher for lower N, gradually diminishes in finer simulations, and appears to be marginally dependent on the order p of the NURBS. Indeed, the average rate is between N^{-4} and N^{-5} for $3 \leq p \leq 6$. This phenomenon is not present in the acoustic simulations (see next section), and is currently under investigation. A possible reason could be related to the adoption of a uniform sampling in the NURBS parameter space which may produce unwanted oscillations of the higher–order functions.[18]

4.5.2   Acoustic scattering of a circular cylinder

In this case, the function $\tilde{\varphi}$ represents a physical quantity satisfying the wave equation in Ω. The equation governing the propagation of an acoustic perturbation of angular frequency ω at speed c_0 is the Helmholtz equation, $\nabla^2 \tilde{\varphi} + \kappa^2 \tilde{\varphi} = 0$, where $\kappa = \omega/c_0^2$. Adopting the $e^{i\omega t}$ time convention, the fundamental solution and its normal derivative on Γ are

$$G(\mathbf{x}, \mathbf{y}, \kappa) = \frac{i}{4} \mathcal{H}_0^{(2)}(\kappa\, r), \;\; \frac{\partial G}{\partial n} = -\frac{i\,\kappa}{4} \mathcal{H}_1^{(2)}(\kappa r) \frac{\mathbf{r} \cdot \mathbf{n}}{r} \tag{4.19}$$

where $r = \|\mathbf{x} - \mathbf{y}\|$ and $\mathcal{H}_m^{(2)}(\kappa\, r)$ is the second–kind Hankel function of order m. The case study at hand consists of a plane wave of unit amplitude impinging on a circular cylinder of infinite length, for which the analytical solution is known (see *e.g.*, Morse and Ingard [17] or Appendix B). Indicating with $\boldsymbol{\kappa}$ the wave vector, the incident field is given by $\tilde{\varphi}_i = e^{i\,\boldsymbol{\kappa}\cdot\boldsymbol{r}}$. Figure 4.6 shows the solution at $f = 50$Hz. The values of $|\tilde{\varphi}|$ at the solution points are indicated with squares, whereas the NURBS reconstruction of the solution along the whole boundary is depicted with the times sign. The agreement with the analytical solution is remarkable. The effect of the h-refinement can be observed in Figure 4.7, where four knots have been inserted in the first and last intervals and two knots in the second and third ones. The refined solution is substantially indistinguishable from the analytical one. This excellent behavior is preserved also at higher frequencies, as Figures 4.8, 4.9, and 4.10 show for $f = 200$Hz, $f = 500$Hz, and $f = 1000$Hz, respectively.

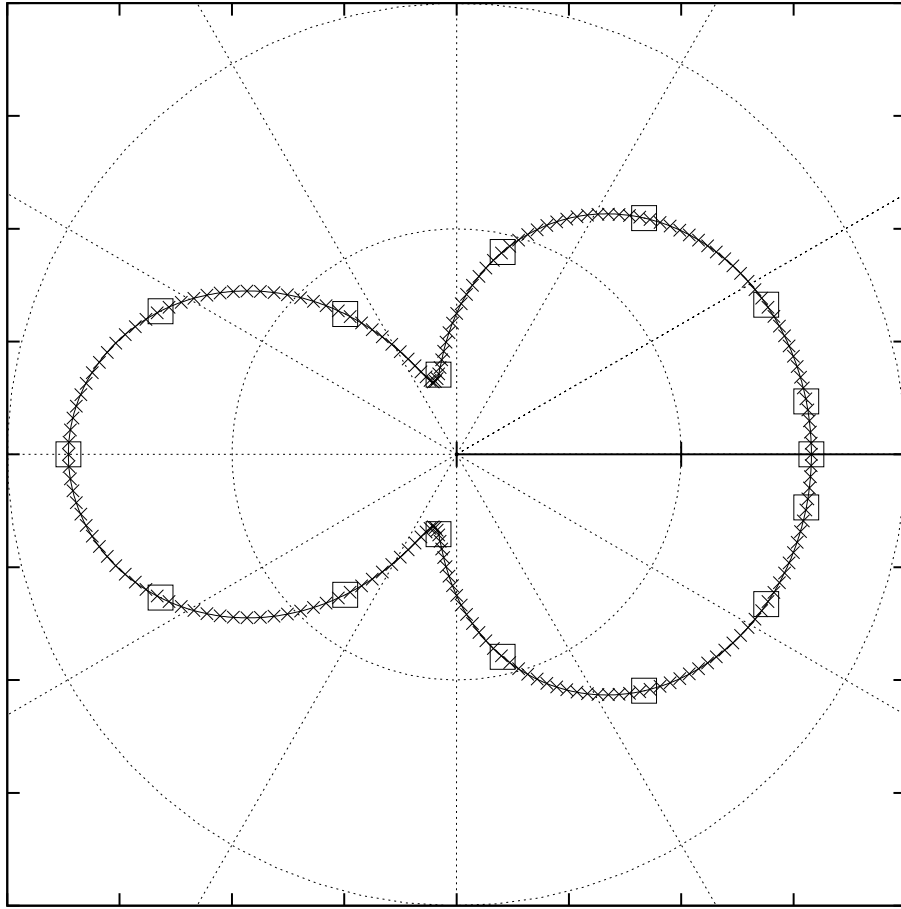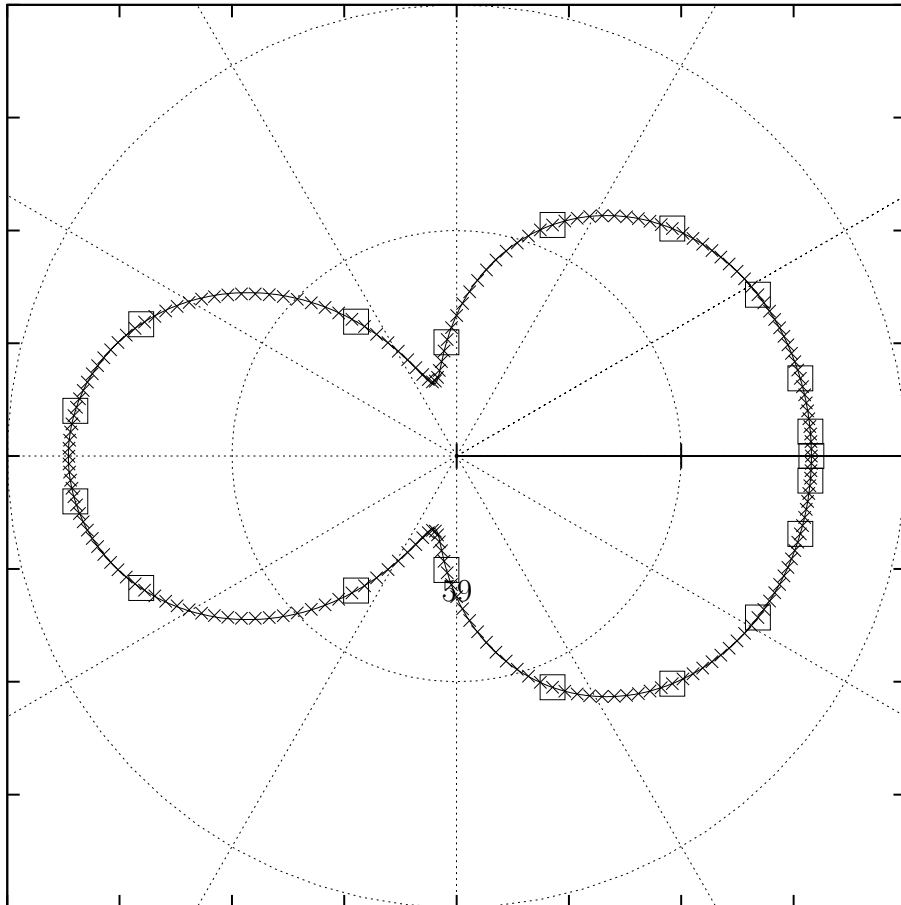Figure 4.6: Scattering field on the cylinder, $f = 50Hz$. $(-)$ Analytical, $(\times)$ BIE-NURBS, $(\square)$ BIE-NURBS at Greville's abscissae.
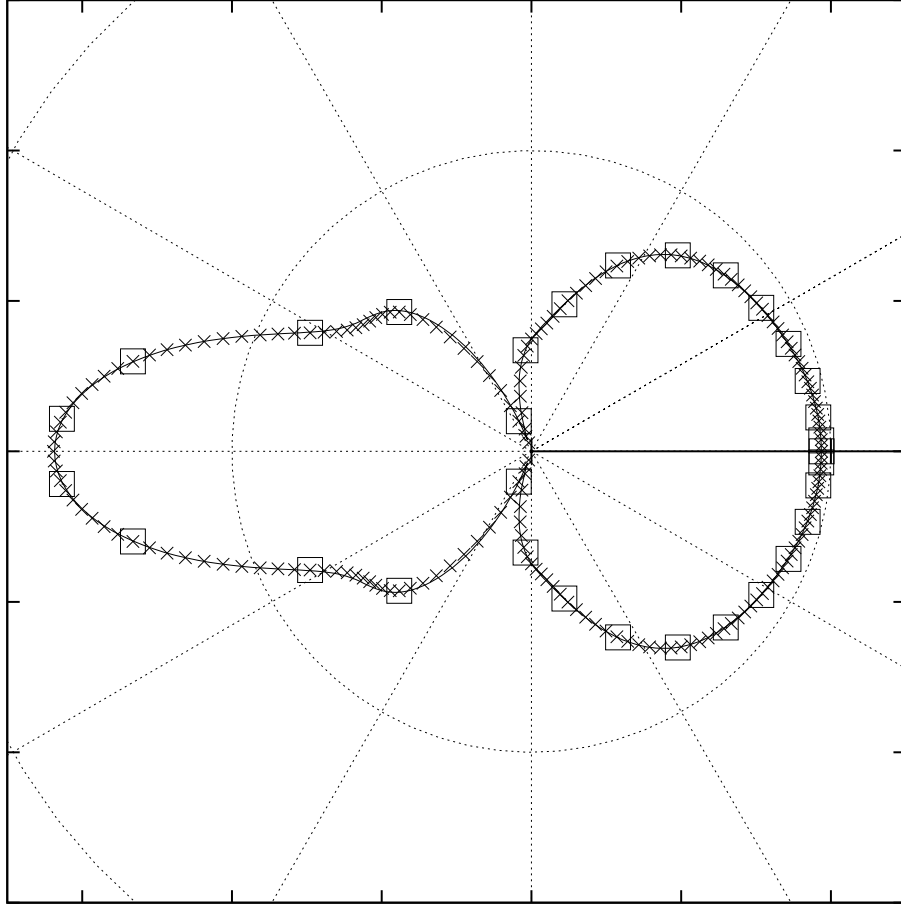
Figure 4.8: Scattering field at $f = 200$Hz, $(-)$ analytical, $(\times)$ BIE-NURBS, $(\square)$ BIE-NURBS at Greville's abscissae, $N = 32$, $p = 3$.
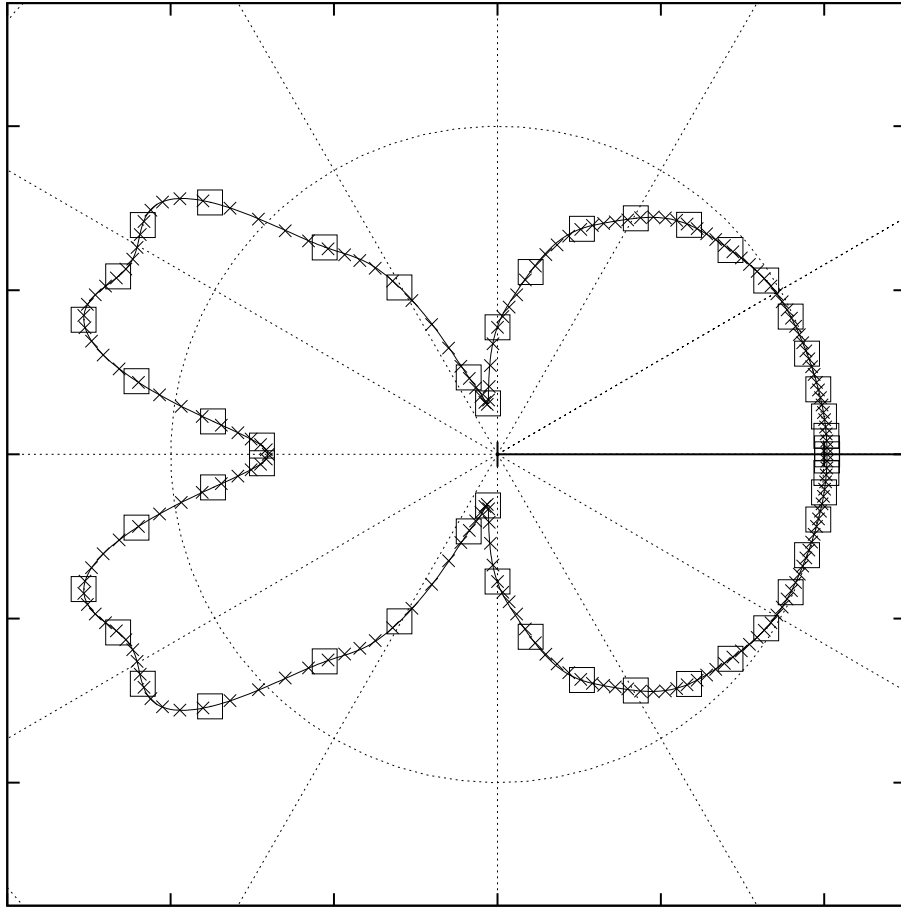
Figure 4.9: Scattering field at $f = 500$Hz, $(-)$ analytical, $(\times)$ BIE-NURBS, $(\square)$ BIE-NURBS at Greville's abscissae, $N = 50$, $p = 5$.
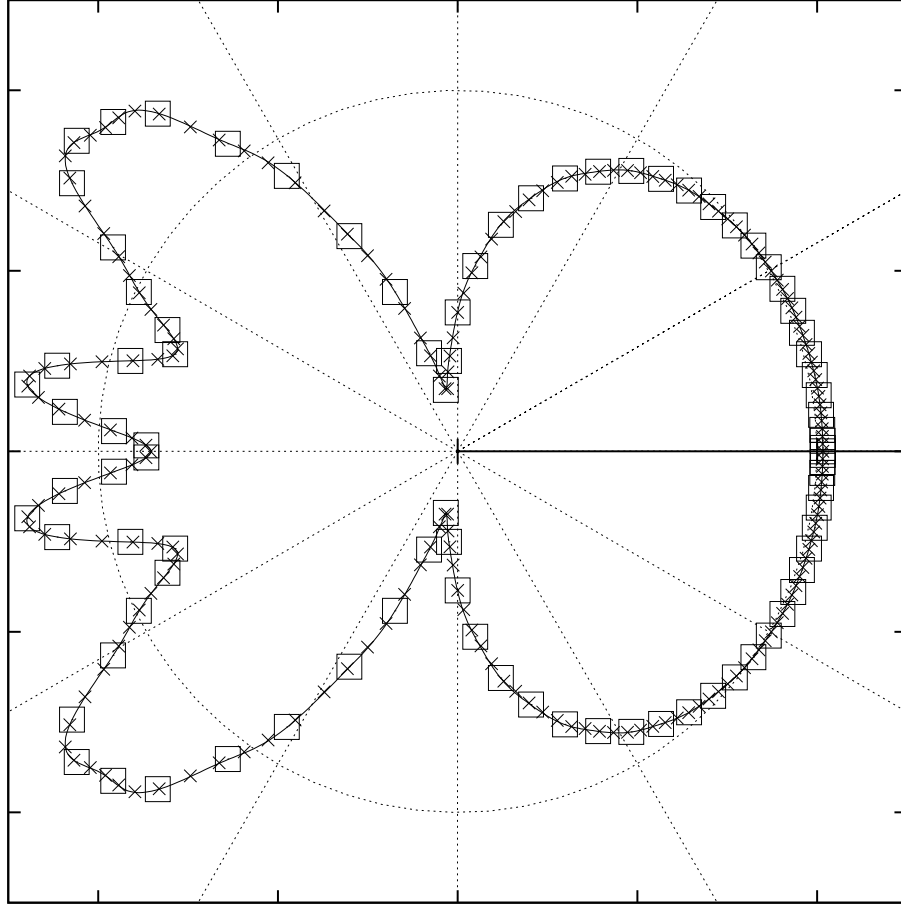
Figure 4.10: Scattering field at $f = 1$kHz, $(-)$ analytical, $(\times)$ BIE-NURBS, $(\square)$ BIE-NURBS at Greville's abscissae, $N = 90$, $p = 5$.

Also in this case, the convergence of the proposed formulation is evaluated using the global error ϵ defined in Equation 4.18. The convergence analysis is performed using the h-refinement by inserting equally spaced knots. The convergence of ϵ as a function of $1/N$ is presented in Figures 4.11 and 4.12 for p=2,3,4,5,6 at $f = 50$Hz and $f = 200$Hz, respectively. As in the aerodynamic application, the log-log plots show a non–linear behavior. The major difference in the present application is in the progressive enhancement of the accuracy and rate of convergence as p increases.
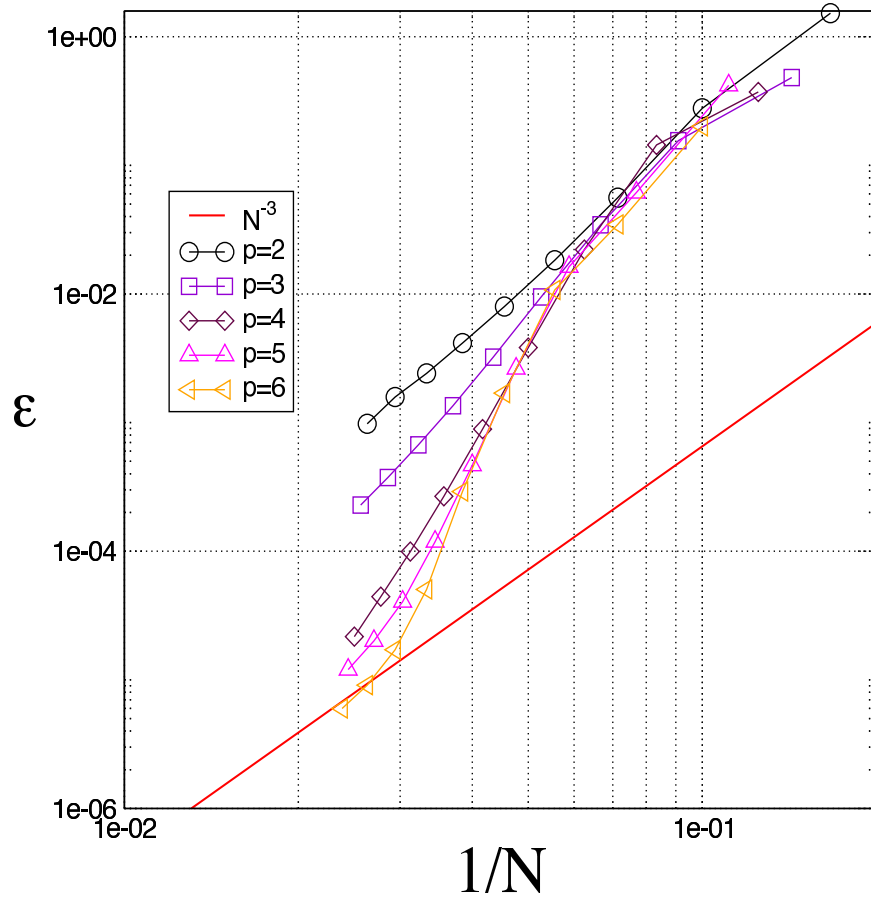
Figure 4.11: NURBS: Convergence of ϵ at $f = 50\text{Hz}$.
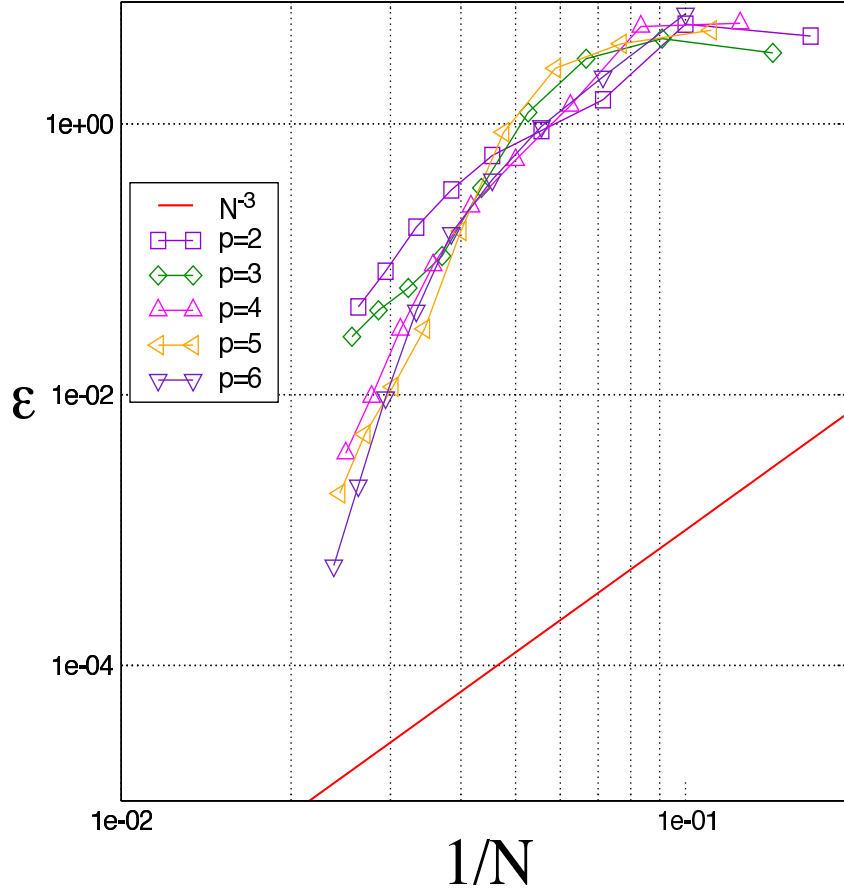
Figure 4.12: NURBS: Convergence of ϵ at $f = 200$Hz.

It can be observed that the rate of convergence is greater than p for all the degrees tested, reaching values close to $\mathcal{O}(N^{-9})$ for $p = 6$, confirming the remarkable level of accuracy achievable with the h- refinement.

Chapter 5

Application to Phononic Crystals

> Homework, I command thee, BE DONE!
>
> ———————————————————————————
>
> C and H

Phononic Crystals are acoustic metamaterials designed to direct the sound waves by exploiting the periodic variations of the acoustic properties of the used material. These metamaterials have the peculiar property of exhibiting a phononic bandgap *i.e.*, a zone in the transmission spectra where the propagation of acoustic waves is forbidden. By carefully designing the crystals it is hence possible to build acoustic wave-guides forcing the acoustic wave in a specific area of the crystal and also having it go around sharp corners. Both experimental and numerical simulations have been done on the subject (see for instance [25], [26]) but to our knowledge, no simulation of these kind of structures has been performed with a BEM methodology.

The level of accuracy needed for the simulation of these phenomena is not attainable with a 0_{th} order BEM formulation due to the many interactions between the structures composing the crystal and to the high frequencies involved.

5.1   Numerical simulation

In the present work we considered two different wave guides built by removing bodies from a matrix of 15×11 cylinders that have a radius of $r = 0.00125$, a

distance between their radius is $l = 0.003$ (Figure 5.1) and are immersed in water ($c = 1497.0 \ m/s$). The first guide is a straight one built by removing a single line
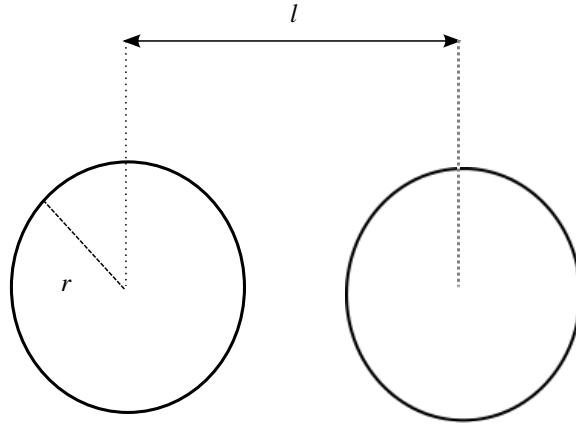

Figure 5.1: Phononic crystals configuration
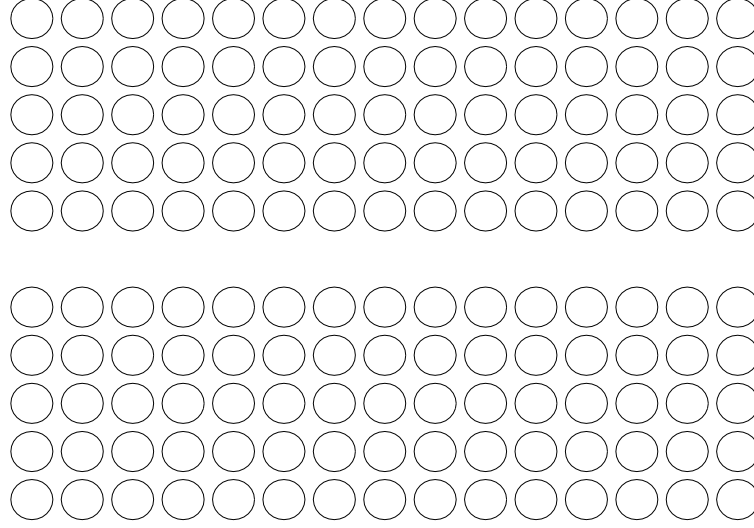
of cylinders (Fig.5.2).

Figure 5.2: Phononic crystals: Straight waveguide

The second one is a S–shaped guide as shown in Figure 5.3. We studied the behaviour of the these two wave guides under a planar wave impinging on the structure. The wave guides were simulated with the approach described in 3.1 in $2D$. In order to find the frequency at which the maximum transmission occurs we performed a frequency analysis evaluating the power transmission spectra defined as:

$$10 \log \left(\frac{\int_L \|P_{tot}\|^2}{\int_L \|P_{inc}\|^2} \right) \tag{5.1}$$

Where P_{tot} and P_{inc} are respectively the total and incident pressure evaluated on the line L at the exit of the guide.
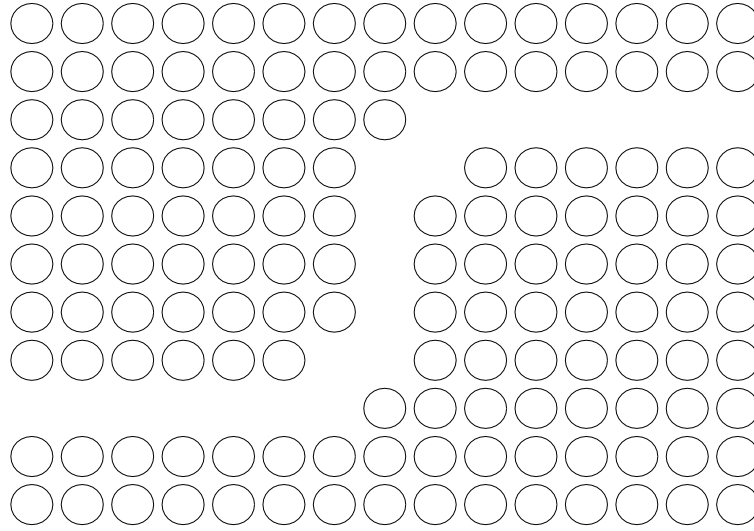
Figure 5.3: Phononic crystals: S–shaped waveguide

5.1.1   Straight guide

In Figure 5.4 we reported the Transmission spectra for the straight guideline. It is clear that the structure has a guiding band starting at $f = 260$kHz and ending at $f = 314$kHz.
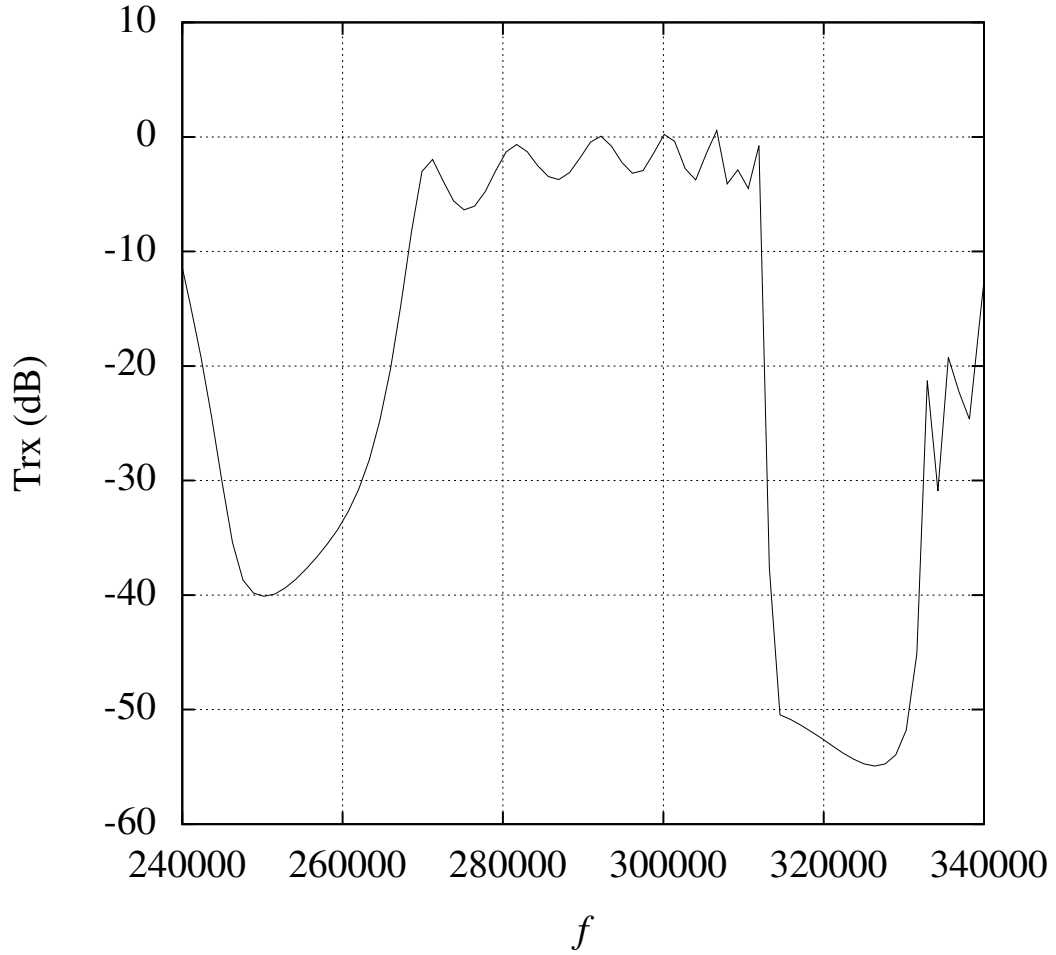
Figure 5.4: Phononic crystals: Straight guide, Power Transmission spectra

In Figure 5.5 and in Figure 5.6 we reported the total pressure field for $f = 292\text{kHz}$ and $f = 314.5\text{kHz}$ respectively to show how the structure behaves like a wave guide at the former frequency and acts like a filter at the latter.
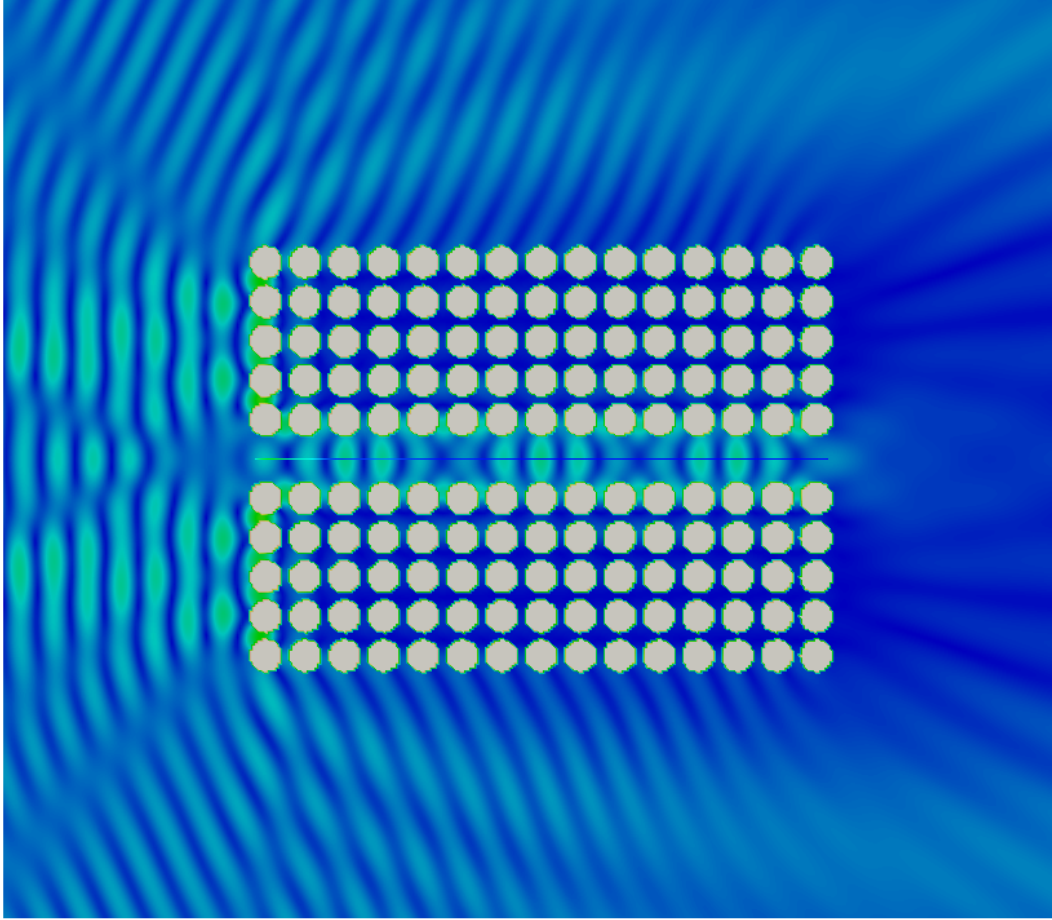
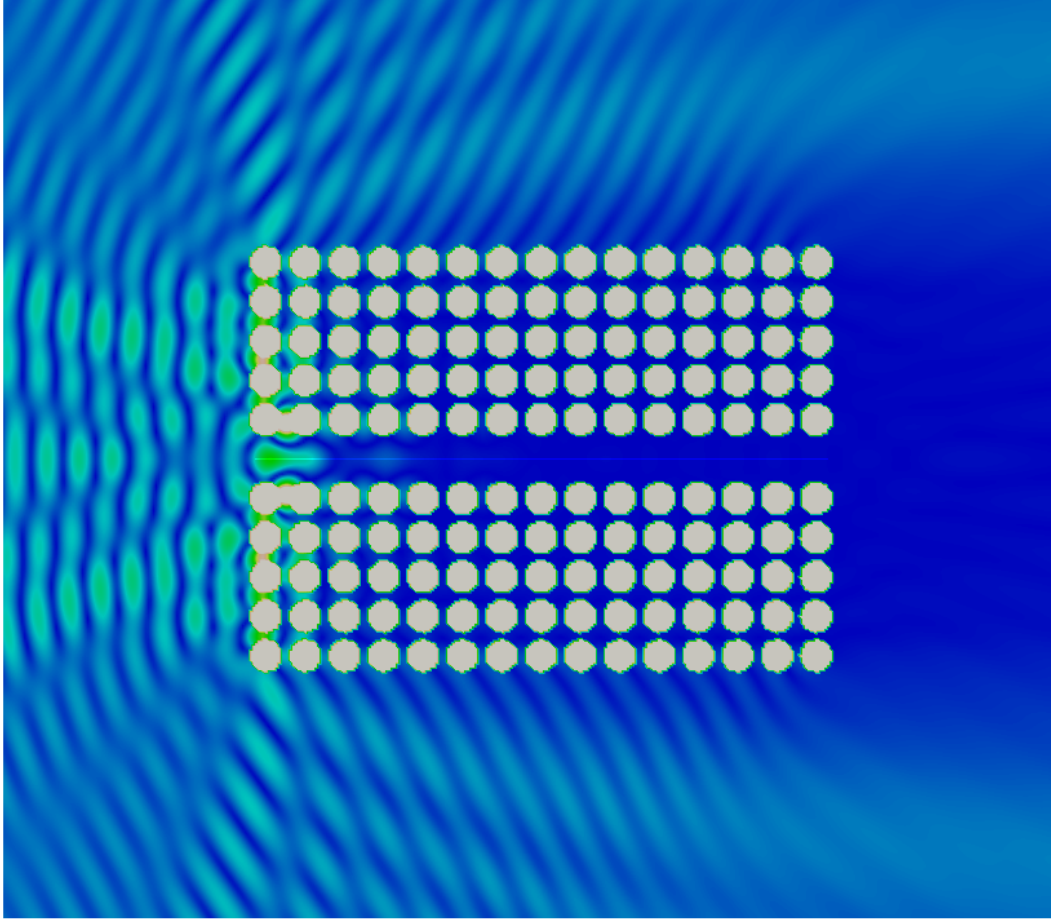Figure 5.5: Phononic crystals: Straight guide, Total Pressure at $f = 292$ kHz

Figure 5.6: Phononic crystals: Straight guide, Total Pressure at $f = 314.5$kHz

In Figure 5.7 we reported the total pressure for the two considered frequencies along a line in the middle of the guide. It is clear that at $f = 314.5$kHz there is a drop in total pressure while at $f = 292$kHz the acoustic pressure propagates almost undisturbed.
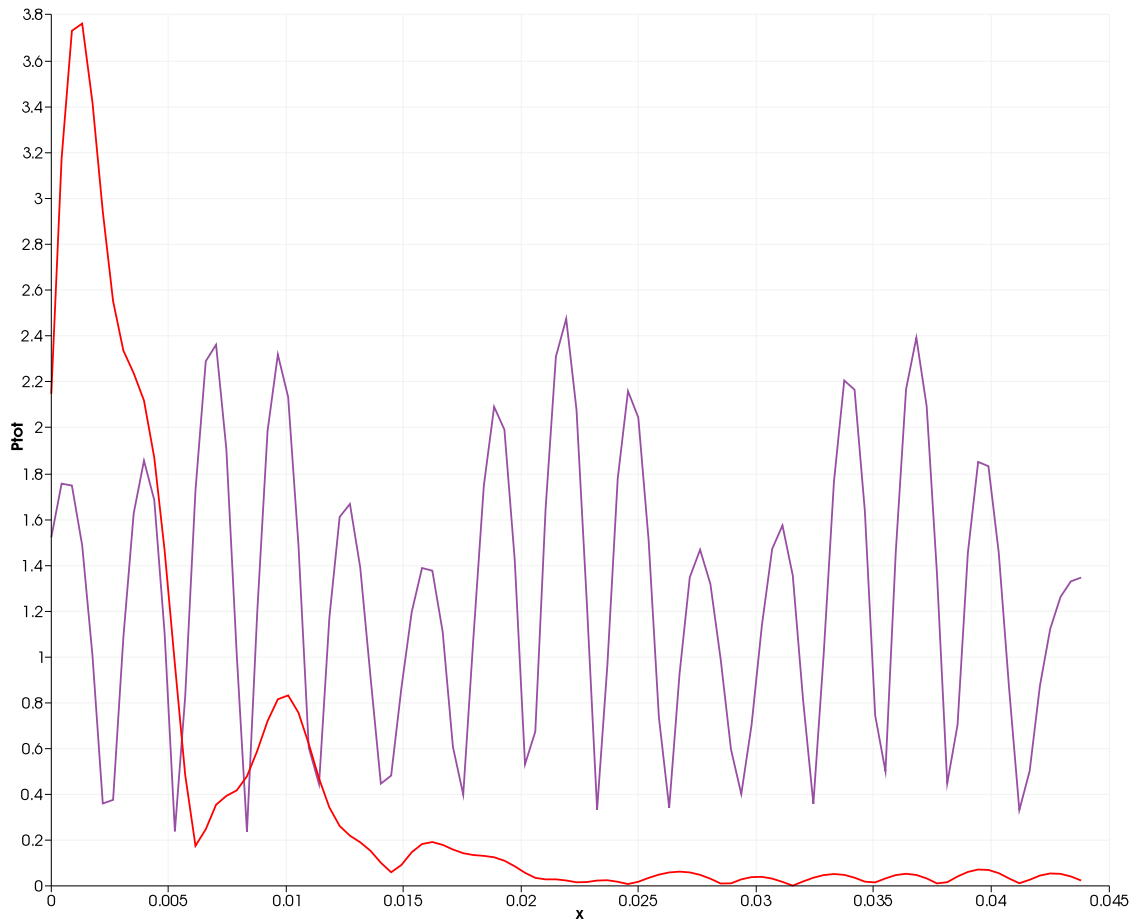
Figure 5.7: Phononic crystals:Total Pressure field along a line in the middle of the wave guide for $f = 292$kHz (purple line) and $f = 314.5$kHz (red line)

5.1.2 S–shaped guide

The same analysis has then been performed on the S–shaped guide. The power transmission spectra is depicted in Figure 5.8 showing a guiding behaviour between $f = 272$kHz and $f = 282$kHz.
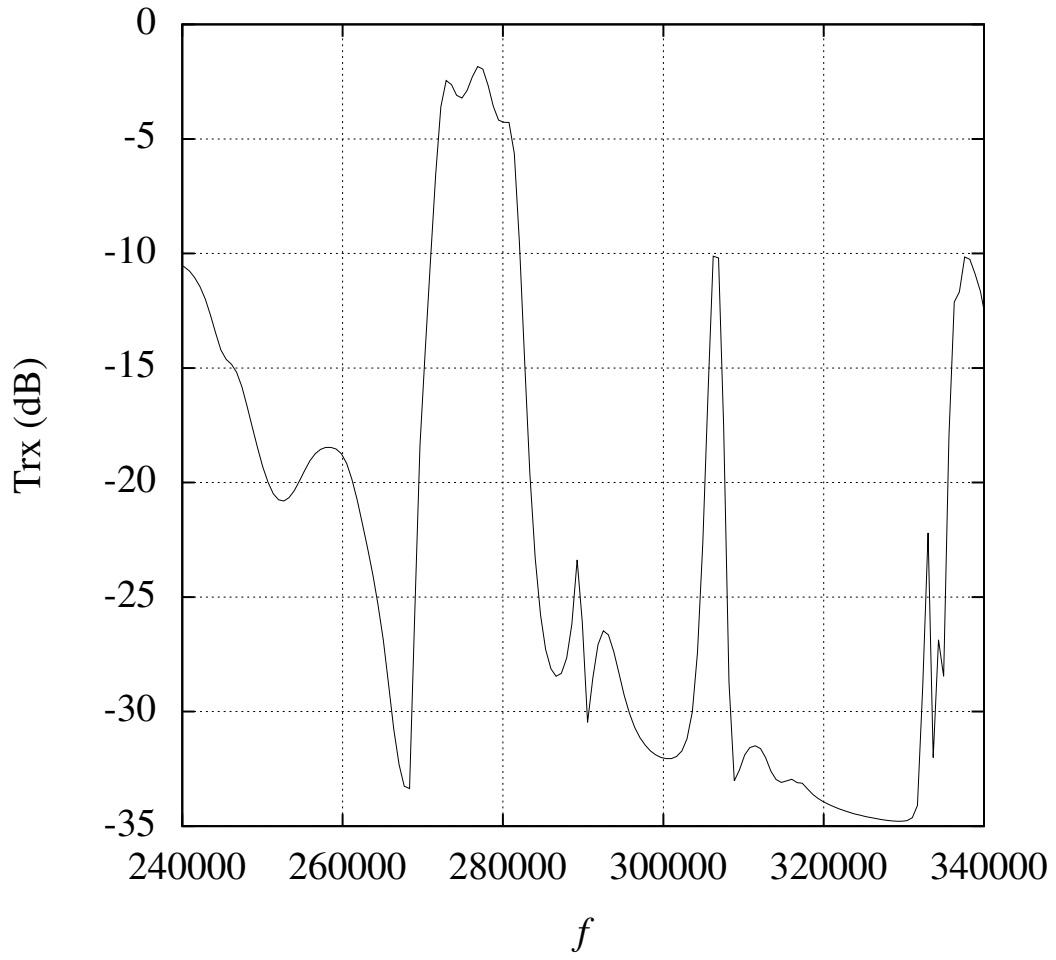
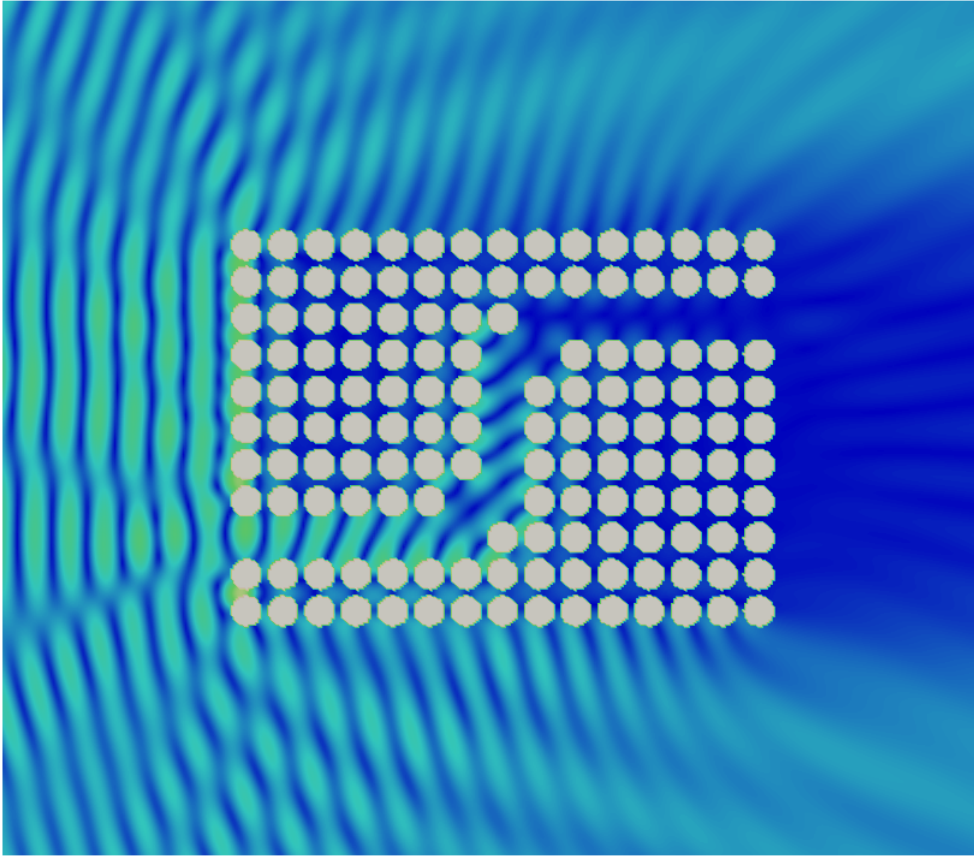Figure 5.8: Phononic crystals: S–guide, Power Transmission spectra

Figure 5.9: Phononic crystals: S–guide, Total Pressure at $f = 267.5$kHz
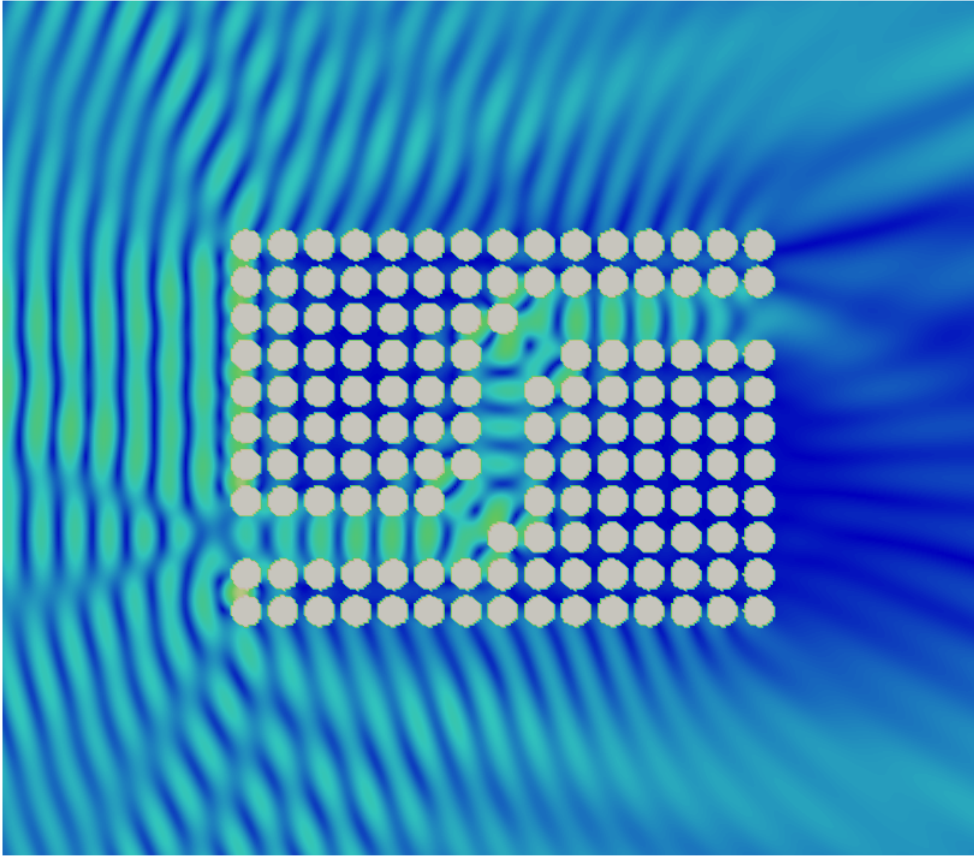
Figure 5.10: Phononic crystals: S–guide, Total Pressure at $f = 277$kHz
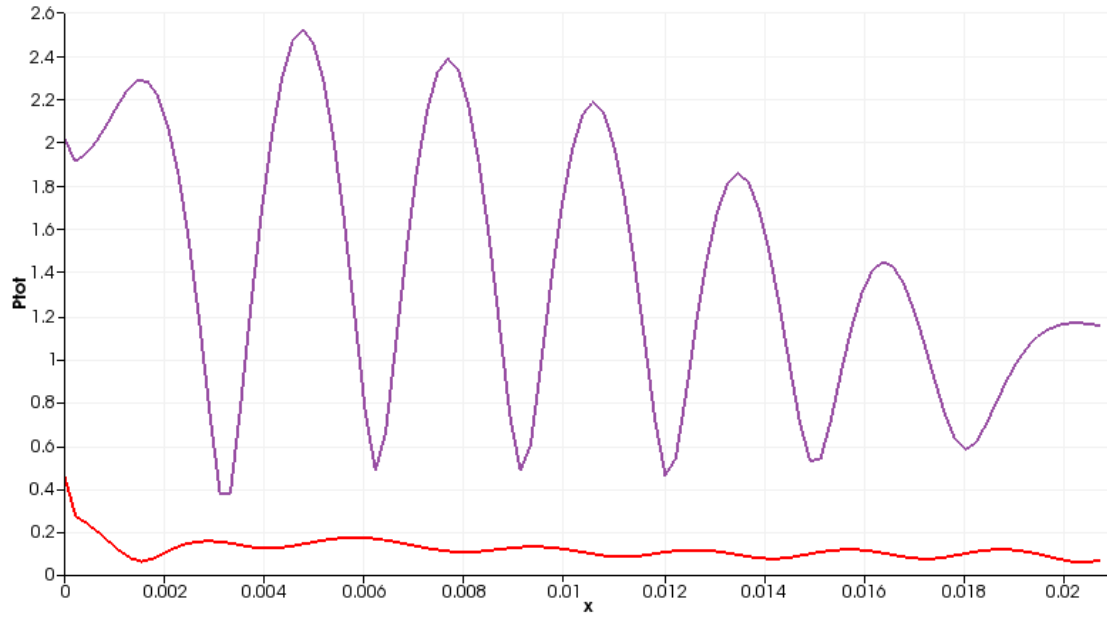
Figure 5.11: Phononic crystals: Total Pressure field along a line in the middle of the exit straight section of the guide for $f = 277\text{kHz}$ (purple line) and $f = 267.5\text{kHz}$ (red line)

The results for the band gap are in agreement with the experimental results reported in [25] confirming the accurateness of the BEM method for the design of these kind of structures.

Bibliography

[1] Coons, S.A. *Surfaces for computer-aided design of space forms MIT Technical Report*, (1967).

[2] Camp, C.V. and Gipson, G.S. Overhauser elements in boundary element analysis. *Mathematical and Computer Modelling*, **15** (3), 59–69, (1991).

[3] Galassi, M., Davies, J., Theiler, J., Gough, B., Jungman, G., Alken, P., Booth, M., and Rossi, F., *GNU Scientific Library – Reference Manual*. Version 1.15. 2011. http://www.gnu.org/software/gsl/, (Accessed August 13, 2013).

[4] http://www.mcs.anl.gov/research/projects/mpi/mpi-standard/mpi-report-2.0/mpi2-report.htm

[5] http://www.netlib.org/scalapack/

[6] Gennaretti, M., Giordani, A., Morino, L. A third-order boundary element method for exterior acoustics with applications to scattering by rigid and elastic shells. *Journal of sound and vibration*, **222**(5), 699–722, (1999).

[7] Hochstadt, H. *Integral Equations*. Wiley Classics Library. Wiley, (2011).

[8] Iemma, U., Burghignoli, L. A Hermite-Coons boundary element method. *Procs. 16th International Congress on Sound and Vibration, ICSV16, Krakow, Poland, July*, (2009).

[9] Walser R.M. Electromagnetic metamaterials *Proc. SPIE*,(2001)

[10] Ochmann M., Piscoya R. Applications of the Acoustical Boundary Element Method (BEM) and related Green's functions *Procs. 20th International Congress on Sound and Vibration, ICSV20, Bangkok, Thailand, July*, (2013).

[11] Iemma, U., Marchese, V., and Morino, L. High-order BEM for potential transonic flows. *Computational mechanics*, **21**(3), 243–252, (1998).

[12] Johnson, R.W., Higher order b-spline collocation at the Greville abscissae. *Appl. Numer. Math.*, **52**(1), 63–75, (2005).

[13] Johnston, P.R. Second order Overhauser elements for boundary element analysis. *Mathematical and computer modelling*, **23** (5), 61–74, (1996).

[14] Kim, B., and Shin, Y.S. A NURBS panel method for three-dimensional radiation and diffraction problems. *Journal of Ship Research*, **47**(2), 177–186, (2003).

[15] Kreyszig, E. *Advanced Engineering Mathematics.* John Wiley & Sons, (2010).

[16] Morino, L., Iemma, U., and Cetta, F. Combining Hermite, Coons and Guyan: a highly efficient high-frequency finite element. In *Procs. of 15th AIAA/CEAS Aeroacoustic Conference*, Miami, FL, USA (2009).

[17] Morse, P.C.M., Ingard, K.U. *Theoretical Acoustics.* International series in pure and applied physics. Princeton University Press (1968).

[18] Piegl, L. On NURBS: a survey. *IEEE Computer Graphics and Applications*, **11**(1), 55–71, (1991).

[19] Politis, C., Ginnis, A,I., Kaklis, P.D., Belibassakis, K., and Feurer, C. An isogeometric BEM for exterior potential-flow problems in the plane. *Procs. 2009 SIAM/ACM Joint Conference on Geometric and Physical Modeling*, 349–354, (2009).

[20] Rogers, D.F. *An Introduction to Nurbs: With Historical Perspective.* Morgan Kaufmann Series in Computer Graphics. Morgan Kaufmann Publishers, (2001).

[21] Simpson, R.N., Bordas, S.P.A., Trevelyan, J., and Rabczuk, T. A two-dimensional isogeometric boundary element method for elastostatic analysis. *Computer Methods in Applied Mechanics and Engineering*, **209-212**(0), 87–100, (2012).

[22] Tricomi, F.G. *Integrals Equations.* Dover Books on Mathematics Series. Dover Publications, Incorporated, (1957).

[23] Iemma, U., Marchese, V. http://acousto.sourceforge.net

[24] BEM Acoustics http://www.bemacoustics.com

[25] A. Khelif, A. Choujaa, S. Benchabane, B. Djafari-Rouhani, and V. Laude Guiding and bending of acoustic waves in highly confined phononic crystal waveguides *Appl. Phys. Lett.*, **84**(22), 4400–4402, (2004).

[26] Yan Pennec, Jérôme O. Vasseur , Bahram Djafari-Rouhani , Leonard Dobrzyński, Pierre A. Deymier Two-dimensional phononic crystals: Examples and applications *Surface Science Report*, **65**(8), 229–291, (2010).

[27] Xiang Xhang and Zhaowei Liu Negative refraction of acoustic waves in two–dimensional phononic crystals *App.Phys.Lett*, **85** (2004).

[28] J. Zhu et al A holey-structured metamaterial for acoustic deep-subwavelength imaging *Nature Physics*, **7**,52–55 (2011).

[29] Rokhlin, Vladimir. Rapid solution of integral equations of classical potential theory. *Journal of Computational Physics* **60**(2), 187-207 (1985).

Appendix A

NURBS Parameters and local coordinates

A.1 NURBS Parameters Distribution

In order to find a distribution of the parameter ξ_k, one can apply different default methods:

- Equally spaced
  The most simple distribution is a uniformly spaced one:

$$\xi_k = \frac{(k-1)}{n+1} \quad k = 1, \dots, n+1 \tag{A.1}$$

  with this kind of distribution the control points will be uniformly spaced too

- Chord length method
  In this case the parameters are computed as

$$d \;=\; \sum_{k=1}^{n} \|\mathbf{f}_k - \mathbf{f}_{k-1}\| \tag{A.2}$$

$$\xi_k \;=\; \frac{\|\mathbf{f}_k - \mathbf{f}_{k-1}\|}{d} \tag{A.3}$$

- Centripetal method

This method is similar to the previous one:

$$d = \sum_{k=1}^{n} \sqrt{\|\mathbf{f}_k - \mathbf{f}_{k-1}\|} \tag{A.4}$$

$$\xi_k = \frac{\sqrt{\|\mathbf{f}_k - \mathbf{f}_{k-1}\|}}{d} \tag{A.5}$$

A.2 Transformation of coordinate system

The integrals in (4.16) are evaluated in the interval $\hat{\xi} \in [-1, 1]$. Moreover the evaluation of the basis functions $N_{a,p}$ is made in the parameter space ξ hence we must compute the jacobian of the two coordinates transformation:

$$J = \frac{d\Gamma}{d\xi} \frac{d\hat{\xi}}{d\xi} \tag{A.6}$$

in which

$$\frac{d\Gamma}{d\xi} = \sqrt{\left(\frac{dx}{d\xi}\right)^2 + \left(\frac{dy}{d\xi}\right)^2} = \|\mathbf{g_1}\| \tag{A.7}$$

being $\|\mathbf{g}_\alpha\|$ the covariant base of the curvilinear coordinate system. The interval $\hat{\xi} \in [-1, 1]$ is then mapped to the parameter space interval $\xi \in [\xi_1, \xi_2]$ with the transformation of coordinates:

$$\xi = \frac{\left[(\xi_2 - \xi_1)\hat{\xi} + (\xi_2 + \xi_1)\right]}{2} \tag{A.8}$$

which allows to write:

$$\frac{d\hat{\xi}}{d\xi} = \frac{\xi_2 - \xi_1}{2} \tag{A.9}$$

and for the total jacobian:

$$J = \frac{\xi_2 - \xi_1}{2} \|\mathbf{g_1}\| \tag{A.10}$$

Appendix B

Analytical solutions

B.1 Planar wave on 2D cylinder

The analytical solution for the total surface pressure exerted by a planar wave of frequency f and amplitude P_0, impinging on a 2D cylinder of radius a is given by:

$$P_{tot}(\theta) = \frac{4P_0}{\pi ka} \sum_{m=1}^{\infty} \frac{\cos(m\theta)}{E(m)} e^{i(-\gamma(m)+1/2(\pi m))} \tag{B.1}$$

in which

$$E(m) = \begin{cases} 2\frac{j_1(ka)}{\sin(\gamma(0))} & \text{if } m = 0, \\[2mm] \frac{j_{m+1}(ka)-j_{m-1}(ka)}{2\sin(\gamma(0))} & \text{if } m \neq 0. \end{cases} \tag{B.2}$$

being $j_\alpha(x)$ the Bessel functions of the first kind and the angles $\gamma(m)$ are given by:

$$\gamma(m) = \begin{cases} \arctan\left(\frac{-j_1(ka)}{y_1(ka)}\right) & \text{if } m = 0, \\[2mm] \arctan\left(\frac{j_{m-1}(ka)-j_{m+1}(ka)}{y_{m+1}(ka)-y_{m-1}(ka)}\right) & \text{if } m \neq 0, \end{cases} \tag{B.3}$$

in which $y_\alpha(x)$ are the Bessel functions of the second kind.

B.2 Planar wave on 3D sphere

The analytical solution for the scattering surface pressure exerted by a planar wave of frequency f and amplitude P_0, impinging on a 3D sphere of radius a is given

by:

$$P_s(r, \theta) = -\sum_{m=0}^{\infty} D_m(2m + 1)i^m P_m(\cos \theta)h_m(kr) \tag{B.4}$$

where

$$D_m = \frac{mj_m(ka) - (m + 1)j_{m+1}(ka)}{mh_m(ka) - (m + 1)h_{m+1}(ka)} \tag{B.5}$$

and $P_\alpha(x)$ are the Legendre polynomials, $h_\alpha(x)$ are the spherical Hankel functions of the first kind and $j_\alpha(x)$ are the spherical Bessel functions of the first kind.

Appendix C

Parallel implementation

With exception of the NURBS–based approach illustrated in Chapter 4, all the algorithm adopted in the present work have been implemented on a HPC architecture exploiting the parallel characteristics of the Boundary Element Method. This has allowed the reduction of the computational effort in particular for the convergence analysis performed. A detailed testing of the parallel code developed in order to determine the efficiency of the implementation is beyond the scope of the present work but it is worth describing some of the choices made and some of the details in the implementation.

C.1   MPI–2 and ScalaPack

The implementations have been developed with the aid of two standard libraries in parallel computing, MPI–2 [4] for the message passing features and ScaLA-PACK [5] for the Linear Algebra operations. In particular, the structure of the implementation is the same for all the approaches considered and the parallel macro–operations are the ones shown in orange in Figure C.1.

Figure C.1: Structure of the algorithm

The solution of the linear system has been done both by using the PZGELS subroutine of the ScaLAPACK library that uses a QR or LQ factorization and with a parallel GMRES algorithm implemented from scratch. It is worth noting how the evaluation of the BEM coefficients for the matrices assembly can be considered "embarrassingly parallel".

The code has been written in the C language and tested on a cluster of Linux nodes with a Scientific Linux derived distribution.

C.2   Details on the implementation

C.2.1   Parallel Loops for 2D solution

The usual implementation for the evaluation of the coefficients (3.19) is a nested loop:

for $x_j = 1, \ldots N_{el} + 1$
  for element$_i = 1, \ldots, N_{el}$
   evaluate integral Bi_{ij}, Ci_{ij}
  end loop on element$_i$
end loop on x_j

being x_j the control point. The ranges $1, \ldots N_{el}+1$ for the control points is splitted on the q rows of the computational grid, whereas the range $1, \ldots N_{el}$ is splitted on the p columns. However, as we can see from Fig.(3.2) we cannot be sure that the evaluation of the integral on a single element contributes to the nodes that are on the same computational node.

In order to avoid data transfer between the nodes we can rewrite the loop as:

for $x_j = 1, \ldots, N_{el} + 1$
  for $x_i = 1, \ldots, N_{el} + 1$
   evaluate integral Bi_{ik}, Ci_{ik} for each element contributing to node x_i
  end loop on x_i
end loop on x_j

element	Coefficients
i+1	$-\frac{1}{2}B2$
i	$B0$, $-\frac{1}{2}B3$
i-1	$B2$, $B1$
i-2	$B3$

Table C.1: 2D Hermite Dual: Coefficients contributing to node k of element i

The partition on the computational grid is now both row-wise and column-wise in terms of geometry nodes. For each node x_i we must consider which elements contribute to that node and evaluate the respective integrals. For instance, considering Fig.(figure:element) and 2-points centered finite differences for the nodal derivatives, we have that for the node k the contributing integrals are the ones reported in Table (C.1) (the same applies for the coefficients C) i.e. the integral on panel $i+1$ will contribute with coefficients $B2$, the integral on panel i with coefficients $B0$ and $B3$ and so on.

C.2.2   Parallel Loops for 3D solution

The evaluation of the coefficients in Eq.(3.39) has been implemented on a cluster of parallel computing nodes by means of the MPI–2 library. The usual implementation for the evaluation of the integral coefficients is a nested loop:

for $x_j = 1, \ldots N_p + 1$
  for element$_i = 1, \ldots, N_{el}$
   evaluate integral B_{ij}, C_{ij} D_{ij}
  end loop on x_j
end loop on element$_i$

being N_p the number of collocation points. The ranges $1, \ldots N_p + 1$ for the collocation points is splitted on the q rows of the computational grid, whereas the range $1, \ldots N_{el}$ is splitted on the p columns. However, as we can see from Fig.(3.16) we cannot be sure that the evaluation of the integral on a single element contributes to the nodes that are on the same computational node. In order to avoid data transfer between the nodes we can rewrite the loop as:

for $x_j = 1, \ldots, N_p + 1$

 for $x_i = 1, \ldots, N_p + 1$

  evaluate integral B_{ij}, C_{ij} D_{ij}

  for each element contributing to node x_i

 end loop on x_j

end loop on element$_i$

The partition on the computational grid is now both row-wise and column-wise in terms of geometry nodes. For each node x_i we must consider which elements contribute to that node and evaluate the respective integrals. In Fig.3.16 we reported the integral coefficients to be evaluated on each element of the multi

patch when considering a nodal value contribution being:

$$\mathrm{B}^0\eta_{ij}\pm \;=\; \int_{\Gamma_i} \frac{(1\pm\xi)}{2} H_0(\eta)\mathcal{K}_j(\xi,\eta)J(\xi,\eta)d\Gamma$$

$$\mathrm{B}^1\eta_{ij}\pm \;=\; \int_{\Gamma_i} \frac{(1\pm\xi)}{2} H_1(\eta)\mathcal{K}_j(\xi,\eta)J(\xi,\eta)d\Gamma$$

$$\mathrm{B}^2\eta_{ij}\pm \;=\; \int_{\Gamma_i} \frac{(1\pm\xi)}{2} H_2(\eta)\mathcal{K}_j(\xi,\eta)J(\xi,\eta)d\Gamma$$

$$\mathrm{B}^4\eta_{ij}\pm \;=\; \int_{\Gamma_i} \frac{(1\pm\xi)}{2} H_3(\eta)\mathcal{K}_j(\xi,\eta)J(\xi,\eta)d\Gamma$$

$$\mathrm{B}^0\xi_{ij}\pm \;=\; \int_{\Gamma_i} \frac{(1\pm\eta)}{2} H_0(\xi)\mathcal{K}_j(\xi,\eta)J(\xi,\eta)d\Gamma$$

$$\mathrm{B}^1\xi_{ij}\pm \;=\; \int_{\Gamma_i} \frac{(1\pm\eta)}{2} H_1(\xi)\mathcal{K}_j(\xi,\eta)J(\xi,\eta)d\Gamma$$

$$\mathrm{B}^2\xi_{ij}\pm \;=\; \int_{\Gamma_i} \frac{(1\pm\eta)}{2} H_2(\xi)\mathcal{K}_j(\xi,\eta)J(\xi,\eta)d\Gamma$$

$$\mathrm{B}^4\xi_{ij}\pm \;=\; \int_{\Gamma_i} \frac{(1\pm\eta)}{2} H_3(\xi)\mathcal{K}_j(\xi,\eta)J(\xi,\eta)d\Gamma$$

$$\mathrm{B}^{++}\xi\eta_{ij} \;=\; \int_{\Gamma_i} \frac{(1+\xi)}{2}\frac{(1+\eta)}{2}\mathcal{K}_j(\xi,\eta)J(\xi,\eta)d\Gamma$$

$$\mathrm{B}^{-+}\xi\eta_{ij} \;=\; \int_{\Gamma_i} \frac{(1-\xi)}{2}\frac{(1+\eta)}{2}\mathcal{K}_j(\xi,\eta)J(\xi,\eta)d\Gamma$$

$$\mathrm{B}^{+-}\xi\eta_{ij} \;=\; \int_{\Gamma_i} \frac{(1+\xi)}{2}\frac{(1-\eta)}{2}\mathcal{K}_j(\xi,\eta)J(\xi,\eta)d\Gamma$$

$$\mathrm{B}^{--}\xi\eta_{ij} \;=\; \int_{\Gamma_i} \frac{(1-\xi)}{2}\frac{(1-\eta)}{2}\mathcal{K}_j(\xi,\eta)J(\xi,\eta)d\Gamma \qquad (C.1)$$

where $\mathcal{K}_j(\xi,\eta)$ is either $G(\xi,\eta)$ or $\frac{\partial G_0(\xi,\eta)}{\partial n}$ or $G_0(\xi,\eta)\frac{\partial\theta(\xi,\eta)}{\partial n}$, depending on the coefficient being evaluated.

Appendix D

Kernel singularities and numerical integration

Aim of the present section is the analysis of the asymptotic behavior of the kernel $\mathcal{K}$ of Eq. 4.7 for $\mathbf{y} \to \mathbf{y}_0 \in \Gamma$ and its relationship with the strategy used for the numerical integration. The analysis deals with the two specific applications covered. Assume that the observation point $\mathbf{y}$ approaches Γ from Ω (*i.e.*, from the positive side of the boundary) pointing to the boundary point $\mathbf{y}_o$ (see Figure 13). The integral on the right hand side of Equation 4.7 can be decomposed into two contributions: the integral over a straight segment Γ_ε centered in $\mathbf{y}_o$ of length 2ε, plus the integral over the remaining part of Γ

$$\mathcal{I}(\mathbf{y}) = \int_{\Gamma_\varepsilon} \tilde{\varphi}(\mathbf{x}) \frac{\partial G(\mathbf{y}, \mathbf{x})}{\partial n} \, \mathrm{d}\Gamma + \int_{\Gamma \backslash \Gamma_\varepsilon} \tilde{\varphi}(\mathbf{x}) \frac{\partial G(\mathbf{y}, \mathbf{x})}{\partial n} \, \mathrm{d}\Gamma \qquad (\mathrm{D.1})$$

Assuming ε sufficiently small, $\mathcal{I}$ can be approximated as

$$\mathcal{I}(\mathbf{y}) \simeq \tilde{\varphi}(\mathbf{y}_o) \, \mathcal{I}^\varepsilon + \int_{\Gamma \backslash \Gamma_\varepsilon} \tilde{\varphi}(\mathbf{x}) \frac{\partial G(\mathbf{y}, \mathbf{x})}{\partial n} \, \mathrm{d}\Gamma \qquad (\mathrm{D.2})$$

The kernels associated to the aerodynamic and the acoustic problems are

$$\mathcal{K}_{\mathsf{ae}}(\mathbf{x}, \mathbf{y}) = -\frac{1}{2\pi} \frac{\mathbf{r} \cdot \mathbf{n}}{r^2}, \quad \mathcal{K}_{\mathsf{ac}}(\mathbf{x}, \mathbf{y}) = -\frac{1}{4} \mathrm{i} \, \kappa \, \mathcal{H}_1^{(2)}(\kappa R) \, \frac{\mathbf{r} \cdot \mathbf{n}}{r} \qquad (\mathrm{D.3})$$

Recalling the asymptotic form of $\mathcal{H}_1^{(2)}$ for small values of its argument (see, *e.g.*, Kreyszig[15]), it can be easily seen that both $\mathcal{K}_{\mathsf{ae}}$ and $\mathcal{K}_{\mathsf{ac}}$ go to infinity as r^{-1}. Introducing the local coordinate (ξ, η), such that $\mathbf{y} \equiv (0, \eta)$ and $\mathbf{x} \equiv (\xi, 0)$ (see
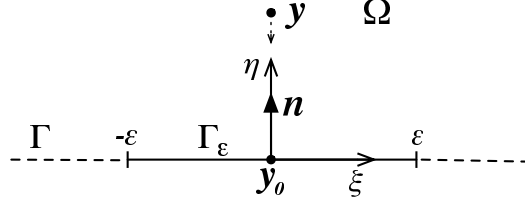
Figure D.1: Observation point $\mathbf{y}$ approaching the boundary at $\mathbf{y}_0$.

Figure D.1), it follows that

$$\mathcal{I}_{\mathsf{ac}}^{\varepsilon} = \int_{-\varepsilon}^{\varepsilon} \left[\frac{-\eta}{2\pi \left(\xi^2 + \eta^2 \right)} + \mathrm{i}\,\eta \frac{\kappa^2}{16} \right] \mathrm{d}\xi = \mathcal{I}_{\mathsf{ae}}^{\varepsilon} + \frac{\mathrm{i}\varepsilon\kappa^2}{8}\,\eta \tag{D.4}$$

It can be easily seen that

$$\mathcal{I}_{\mathsf{ae}}^{\varepsilon} = -\frac{1}{\pi} \arctan \frac{\varepsilon}{\eta} \tag{D.5}$$

Taking the limit for $\mathbf{y} \to \mathbf{y}_0$ yields $\lim_{\eta\to 0} \mathcal{I}_{\mathsf{ae}}^{\varepsilon} = \lim_{\eta\to 0} \mathcal{I}_{\mathsf{ac}}^{\varepsilon} = -0.5$. Now, substituting the result into Eq. D.2, it is possible to shrink indefinitely Γ_ε to obtain for both acoustic and aerodynamics

$$\lim_{\varepsilon\to 0} \mathcal{I}(\mathbf{y}_0) = -\frac{1}{2}\,\tilde{\varphi}(\mathbf{y}_o) + \int_{\Gamma} \tilde{\varphi}(\mathbf{x}) \frac{\partial G(\mathbf{y}, \mathbf{x})}{\partial n}\,\mathrm{d}\Gamma \tag{D.6}$$

Substituting Eq. D.6 into Eq. 4.7 follows that the domain function $E(\mathbf{y})$ equals 0.5 at a regular point $\mathbf{y}_0 \in \Gamma$. The remaining part of the integral (*i.e.*, the integral appearing in Eq. D.6) is a convergent improper integral and can be integrated using standard adaptive quadrature formulae capable to isolate the singularity of the integrand function.

In the present work, Gauss–Kronrod adaptive quadrature rules have been used, as implemented in the GNU Scientific Library.[3] The results obtained are presented in Table D.1, where the value of the real part of the integral in Equation D.6 is reported for different number of Gaussian integration points N_G. The influence of a partition of the boundary Γ into N_Γ parts has been also included. Two geometries have been analyzed: a circle and a flower–shaped geometry (Fig.D.2) represented by the parametric equations:

$$x(\theta) = [1 + 0.5\sin(5\theta)]\cos(\theta), \ y(\theta) = [1 + 0.5\sin(5\theta)]\sin(\theta). \tag{D.7}$$

Table D.1: Real part of the double-layer integrals ($\times 10^3$) as a function of number of Gaussian abscissae N_G and number of partition of the boundary N_Γ.

circle			
	N_G=15	N_G=30	N_G=60
N_Γ=1	5.13868867036	5.13868866829	5.13868867004
N_Γ=2	5.13868867036	5.13868866829	5.13868867004
N_Γ=4	5.13868867036	5.13868866829	5.13868867004
flower–like			
N_Γ=1	8.567698577476	8.567693658759	8.567712281749
N_Γ=2	8.567698577476	8.567693658759	8.567712281749
N_Γ=4	8.567698577476	8.567693658759	8.567712281749
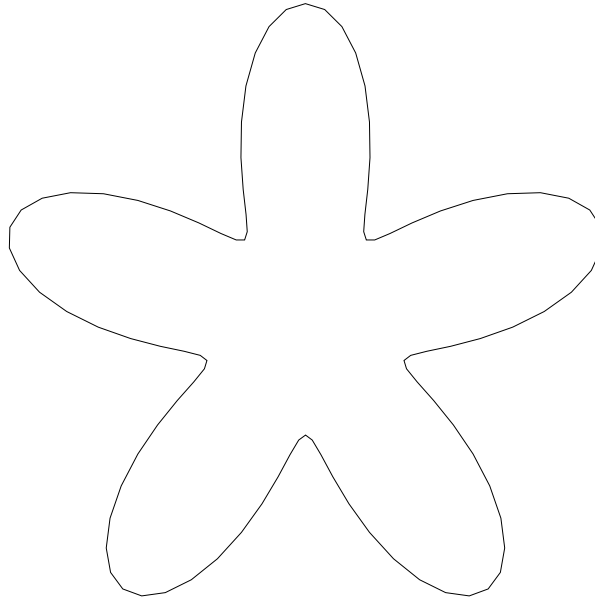
Figure D.2: Flower–shaped geometry

91

As can be seen, the convergence of the integration is extremely fast, giving values substantially converged even with the coarsest quadrature rule. In addition, the partition of Γ has no effects on the integral values, confirming the validity of the NURBS global representation for the meshless solution of the BIE. Needless to say, in presence of complex geometries, presenting slope and curvature discontinuities, the assumption of unit weights in Eq.4.5 makes the accurate approximation of the integrand impossible, thus causing the numerical convergence of the quadrature rule impossible to be achieved when extended to the whole boundary. Nevertheless, in those specific cases the geometry can be partitioned into macro patches having the desired level of smoothness and the integrals in Equations 4.7 and 4.16 can be split into their restrictions to each continuos patch.

Appendix E

Hermite Coons Dual

Starting from 3.45 we can write:

$$\nabla_t \mathbf{n} = \frac{\partial \mathbf{n}}{\partial x^i} \mathbf{g}^i \qquad i = 1, 2 \tag{E.1}$$

But the covariant derivative of $\mathbf{n}$ is:

$$\frac{\partial \mathbf{n}}{\partial x^j} = \left(\frac{\partial n^i}{\partial x^j} + \Gamma^i_{jk} n^k \right) \mathbf{g}_i \tag{E.2}$$

in which

$$\Gamma^i_{kj} = \frac{\partial \mathbf{g}_j}{\partial x^j} \cdot \mathbf{g}^i \tag{E.3}$$

are the Christoffel symbols of the second kind. We can then write:

$$\nabla_t \mathbf{n} = \left(\frac{\partial n^i}{\partial x^j} + \Gamma^i_{kj} n^k \right) \mathbf{g}_i \otimes \mathbf{g}^j = n^i_{,j} \mathbf{g}_i \otimes \mathbf{g}^j \qquad i = 1..3 \ \ j = 1, 2 \ \ k = 1..3 \tag{E.4}$$

Having defined the covariant derivative of a vector $\mathbf{u}$ as:

$$u^i_{,j} = \frac{\partial u^i}{\partial x^j} + \Gamma^i_{kj} u^k \tag{E.5}$$

It is worth mentioning that, since in the covariant basis $\mathbf{g}_i$, the components of $\mathbf{n}$ for $i = 1, 2$ are $= 0$, and $n^3 = 1$ being $\mathbf{n} = \mathbf{g}_3/\|\mathbf{g}_3\|$ the covariant derivatives of $\mathbf{n}$ become:

$$
\begin{aligned}
n^1_{,j} &= \Gamma^1_{3j} \\
n^2_{,j} &= \Gamma^2_{3j} \\
n^3_{,j} &= \frac{\partial n^3}{\partial x^j} + \Gamma^3_{3j}
\end{aligned}
\tag{E.6}
$$

Hence:

$$
\begin{aligned}
\nabla_t \mathbf{n} \quad = \quad & \Gamma^1_{3j} \mathbf{g}_1 \otimes \mathbf{g}^j \\
+ \quad & \Gamma^2_{3j} \mathbf{g}_2 \otimes \mathbf{g}^j \\
+ \quad & \left(\frac{\partial n^3}{\partial x^j} + \Gamma^3_{3j} \right) \mathbf{g}_3 \otimes \mathbf{g}^j \quad j = 1,2
\end{aligned} \tag{E.7}
$$

Since:

$$
\nabla_t \varphi = \frac{\partial \varphi}{\partial x^k} \mathbf{g}^k \quad k = 1,2 \tag{E.8}
$$

projecting 3.45 onto $\mathbf{g}_1$ and $\mathbf{g}_2$ and since $\mathbf{g}_3 \cdot \mathbf{g}_1 = 0$ and $\mathbf{g}_3 \cdot \mathbf{g}_2 = 0$, we can write:

$$
\begin{aligned}
\left[\nabla_t \mathbf{n} \right] \nabla_t \varphi \cdot \mathbf{g}_1 \quad = \quad & \\
+ \quad & \Gamma^1_{31} \left[\frac{\partial \varphi}{\partial x^1} (\mathbf{g}^1 \cdot \mathbf{g}^1) + \frac{\partial \varphi}{\partial x^2} (\mathbf{g}^2 \cdot \mathbf{g}^1) \right] (\mathbf{g}_1 \cdot \mathbf{g}_1) \\
+ \quad & \Gamma^2_{31} \left[\frac{\partial \varphi}{\partial x^1} (\mathbf{g}^1 \cdot \mathbf{g}^1) + \frac{\partial \varphi}{\partial x^2} (\mathbf{g}^2 \cdot \mathbf{g}^1) \right] (\mathbf{g}_2 \cdot \mathbf{g}_1) \\
+ \quad & \Gamma^1_{32} \left[\frac{\partial \varphi}{\partial x^1} (\mathbf{g}^1 \cdot \mathbf{g}^2) + \frac{\partial \varphi}{\partial x^2} (\mathbf{g}^2 \cdot \mathbf{g}^2) \right] (\mathbf{g}_1 \cdot \mathbf{g}_1) \\
+ \quad & \Gamma^2_{32} \left[\frac{\partial \varphi}{\partial x^1} (\mathbf{g}^1 \cdot \mathbf{g}^2) + \frac{\partial \varphi}{\partial x^2} (\mathbf{g}^2 \cdot \mathbf{g}^2) \right] (\mathbf{g}_2 \cdot \mathbf{g}_1) \\
= \quad & \Gamma^1_{31} \left[\frac{\partial \varphi}{\partial x^1} \|\mathbf{g}^1\|^2 + \frac{\partial \varphi}{\partial x^2} (\mathbf{g}^2 \cdot \mathbf{g}^1) \right] \|\mathbf{g}_1\|^2 \\
+ \quad & \Gamma^2_{31} \left[\frac{\partial \varphi}{\partial x^1} \|\mathbf{g}^1\|^2 + \frac{\partial \varphi}{\partial x^2} (\mathbf{g}^2 \cdot \mathbf{g}^1) \right] (\mathbf{g}_2 \cdot \mathbf{g}_1) \\
+ \quad & \Gamma^1_{32} \left[\frac{\partial \varphi}{\partial x^1} (\mathbf{g}^1 \cdot \mathbf{g}^2) + \frac{\partial \varphi}{\partial x^2} \|\mathbf{g}^2\|^2 \right] \|\mathbf{g}_1\|^2 \\
+ \quad & \Gamma^2_{32} \left[\frac{\partial \varphi}{\partial x^1} (\mathbf{g}^1 \cdot \mathbf{g}^2) + \frac{\partial \varphi}{\partial x^2} \|\mathbf{g}^2\|^2 \right] (\mathbf{g}_2 \cdot \mathbf{g}_1)
\end{aligned} \tag{E.9}
$$

$$\left[\nabla_t \mathbf{n}\right] \nabla_t \varphi \cdot \mathbf{g}_2 \quad =$$

$$+ \quad \Gamma_{31}^1 \left[\frac{\partial \varphi}{\partial x^1}(\mathbf{g}^1 \cdot \mathbf{g}^1) + \frac{\partial \varphi}{\partial x^2}(\mathbf{g}^2 \cdot \mathbf{g}^1) \right] (\mathbf{g}_1 \cdot \mathbf{g}_2)$$

$$+ \quad \Gamma_{31}^2 \left[\frac{\partial \varphi}{\partial x^1}(\mathbf{g}^1 \cdot \mathbf{g}^1) + \frac{\partial \varphi}{\partial x^2}(\mathbf{g}^2 \cdot \mathbf{g}^1) \right] (\mathbf{g}_2 \cdot \mathbf{g}_2)$$

$$+ \quad \Gamma_{32}^1 \left[\frac{\partial \varphi}{\partial x^1}(\mathbf{g}^1 \cdot \mathbf{g}^2) + \frac{\partial \varphi}{\partial x^2}(\mathbf{g}^2 \cdot \mathbf{g}^2) \right] (\mathbf{g}_1 \cdot \mathbf{g}_2)$$

$$+ \quad \Gamma_{32}^2 \left[\frac{\partial \varphi}{\partial x^1}(\mathbf{g}^1 \cdot \mathbf{g}^2) + \frac{\partial \varphi}{\partial x^2}(\mathbf{g}^2 \cdot \mathbf{g}^2) \right] (\mathbf{g}_2 \cdot \mathbf{g}_2)$$

$$= \quad \Gamma_{31}^1 \left[\frac{\partial \varphi}{\partial x^1}\|\mathbf{g}^1\|^2 + \frac{\partial \varphi}{\partial x^2}(\mathbf{g}^2 \cdot \mathbf{g}^1) \right] (\mathbf{g}_1 \cdot \mathbf{g}_2)$$

$$+ \quad \Gamma_{31}^2 \left[\frac{\partial \varphi}{\partial x^1}\|\mathbf{g}^1\|^2 + \frac{\partial \varphi}{\partial x^2}(\mathbf{g}^2 \cdot \mathbf{g}^1) \right] \|\mathbf{g}_2\|^2$$

$$+ \quad \Gamma_{32}^1 \left[\frac{\partial \varphi}{\partial x^1}(\mathbf{g}^1 \cdot \mathbf{g}^2) + \frac{\partial \varphi}{\partial x^2}\|\mathbf{g}^2\|^2 \right] (\mathbf{g}_1 \cdot \mathbf{g}_2)$$

$$+ \quad \Gamma_{32}^2 \left[\frac{\partial \varphi}{\partial x^1}(\mathbf{g}^1 \cdot \mathbf{g}^2) + \frac{\partial \varphi}{\partial x^2}\|\mathbf{g}^2\|^2 \right] \|\mathbf{g}_2\|^) \tag{E.10}$$

Substituting in 3.45 we arrive at:

$$E(\mathbf{y})\varphi(\mathbf{y}) \quad = \quad \sum_{k=1}^{N_{el}} \oint_{\mathcal{S}_k} \left(G\frac{\partial \varphi}{\partial n} - \varphi\frac{\partial G}{\partial n} \right) d\mathcal{S}$$

$$E(\mathbf{y})\frac{\partial \varphi(\mathbf{y})}{\partial x^1} \quad = \quad \sum_{k=1}^{N_{el}} \oint_{\mathcal{S}_k} \left(-\frac{\partial G}{\partial x^1}\frac{\partial \varphi}{\partial n} \right) d\mathcal{S}$$

$$- \quad \sum_{k=1}^{N_{el}} \oint_{\mathcal{S}_k} \left(\frac{\partial \varphi}{\partial x^1}\mathbf{H} + \frac{\partial \varphi}{\partial x^2}\mathbf{K} \right) d\mathcal{S}$$

$$E(\mathbf{y})\frac{\partial \varphi(\mathbf{y})}{\partial x^2} \quad = \quad \sum_{k=1}^{N_{el}} \oint_{\mathcal{S}_k} \left(-\frac{\partial G}{\partial x^2}\frac{\partial \varphi}{\partial n} \right) d\mathcal{S}$$

$$- \quad \sum_{k=1}^{N_{el}} \oint_{\mathcal{S}_k} \left(\frac{\partial \varphi}{\partial x^1}\mathbf{M} + \frac{\partial \varphi}{\partial x^2}\mathbf{N} \right) d\mathcal{S} \tag{E.11}$$

where

$$
\begin{aligned}
\mathbf{H} &= G\big[\big(\Gamma_{32}^1\|\mathbf{g}_1\|^2 + \Gamma_{32}^2(\mathbf{g}_1\cdot\mathbf{g}_2)\big)(\mathbf{g}^1\cdot\mathbf{g}^2) \\
&+ \big(\Gamma_{31}^1\|\mathbf{g}_1\|^2 + \Gamma_{31}^2(\mathbf{g}_1\cdot\mathbf{g}_2)\big)\|\mathbf{g}^1\|^2\big] + \frac{\partial G}{\partial n} \\
\mathbf{M} &= G\big[\big(\Gamma_{32}^2\|\mathbf{g}_2\|^2 + \Gamma_{32}^1(\mathbf{g}_1\cdot\mathbf{g}_2)\big)(\mathbf{g}^1\cdot\mathbf{g}^2) \\
&+ \big(\Gamma_{31}^2\|\mathbf{g}_2\|^2 + \Gamma_{31}^1(\mathbf{g}_1\cdot\mathbf{g}_2)\big)\|\mathbf{g}^1\|^2\big] \\
\mathbf{K} &= G\big[\big(\Gamma_{31}^1\|\mathbf{g}_1\|^2 + \Gamma_{31}^2(\mathbf{g}_1\cdot\mathbf{g}_2)\big)(\mathbf{g}^1\cdot\mathbf{g}^2) \\
&+ \big(\Gamma_{32}^1\|\mathbf{g}_1\|^2 + \Gamma_{32}^2(\mathbf{g}_1\cdot\mathbf{g}_2)\big)\|\mathbf{g}^2\|^2\big] \\
\mathbf{N} &= G\big[\big(\Gamma_{31}^2\|\mathbf{g}_2\|^2 + \Gamma_{31}^1(\mathbf{g}_1\cdot\mathbf{g}_2)\big)(\mathbf{g}^1\cdot\mathbf{g}^2) \\
&+ \big(\Gamma_{32}^2\|\mathbf{g}_2\|^2 + \Gamma_{32}^1(\mathbf{g}_1\cdot\mathbf{g}_2)\big)\|\mathbf{g}^2\|^2\big] + \frac{\partial G}{\partial n}
\end{aligned}
\tag{E.12}
$$

Introducing in E.11 the Hermite Coons representation of the variables φ and $\chi = \frac{\partial G}{\partial n}$ as in equation 3.34 we can write:

$$
\begin{aligned}
E(\mathbf{y})\varphi(\mathbf{y}) &= \sum_{k=1}^{N_{el}}\oint_{\mathcal{S}_k}\left[G\left(\chi_i\mathcal{C}_i(\xi,\eta) + \frac{\partial\chi}{\partial\xi}\Big|_i \mathcal{D}_i^\xi(\xi,\eta) + \frac{\partial\chi}{\partial\eta}\Big|_i \mathcal{D}_i^\eta(\xi,\eta)\right)\right]J(\xi,\eta)d\mathcal{S} \tag{E.13}
\end{aligned}
$$

$$
\begin{aligned}
&- \sum_{k=1}^{N_{el}}\oint_{\mathcal{S}_k}\left[\frac{\partial G}{\partial n}\left(\varphi_i\mathcal{C}_i(\xi,\eta) + \frac{\partial\varphi}{\partial\xi}\Big|_i \mathcal{D}_i^\xi(\xi,\eta) + \frac{\partial\varphi}{\partial\eta}\Big|_i \mathcal{D}_i^\eta(\xi,\eta)\right)\right]J(\xi,\eta)d\mathcal{S}
\end{aligned}
$$

$$
\begin{aligned}
E(\mathbf{y})\frac{\partial\varphi(\mathbf{y})}{\partial\xi} &= \sum_{k=1}^{N_{el}}\oint_{\mathcal{S}_k}\left[-\frac{\partial G}{\partial\xi}\left(\chi_i\mathcal{C}_i(\xi,\eta) + \frac{\partial\chi}{\partial\xi}\Big|_i \mathcal{D}_i^\xi(\xi,\eta) + \frac{\partial\chi}{\partial\eta}\Big|_i \mathcal{D}_i^\eta(\xi,\eta)\right)\right]J(\xi,\eta)d\mathcal{S}
\end{aligned}
$$

$$
\begin{aligned}
&- \sum_{k=1}^{N_{el}}\oint_{\mathcal{S}_k}\left[\mathbf{H}\left(\varphi_i\frac{\partial\mathcal{C}_i(\xi,\eta)}{\partial\xi} + \frac{\partial\varphi}{\partial\xi}\Big|_i \frac{\partial\mathcal{D}_i^\xi(\xi,\eta)}{\partial\xi} + \frac{\partial\varphi}{\partial\eta}\Big|_i \frac{\partial\mathcal{D}_i^\eta(\xi,\eta)}{\partial\xi}\right)\right]J(\xi,\eta)d\mathcal{S}
\end{aligned}
$$

$$
\begin{aligned}
&- \sum_{k=1}^{N_{el}}\oint_{\mathcal{S}_k}\left[\mathbf{K}\left(\varphi_i\frac{\partial\mathcal{C}_i(\xi,\eta)}{\partial\eta} + \frac{\partial\varphi}{\partial\xi}\Big|_i \frac{\partial\mathcal{D}_i^\xi(\xi,\eta)}{\partial\eta} + \frac{\partial\varphi}{\partial\eta}\Big|_i \frac{\partial\mathcal{D}_i^\eta(\xi,\eta)}{\partial\eta}\right)\right]J(\xi,\eta)d\mathcal{S}
\end{aligned}
$$

$$
\begin{aligned}
E(\mathbf{y})\frac{\partial\varphi(\mathbf{y})}{\partial\eta} &= \sum_{k=1}^{N_{el}}\oint_{\mathcal{S}_k}\left[-\frac{\partial G}{\partial\eta}\left(\chi_i\mathcal{C}_i(\xi,\eta) + \frac{\partial\chi}{\partial\xi}\Big|_i \mathcal{D}_i^\xi(\xi,\eta) + \frac{\partial\chi}{\partial\eta}\Big|_i \mathcal{D}_i^\eta(\xi,\eta)\right)\right]J(\xi,\eta)d\mathcal{S}
\end{aligned}
$$

$$
\begin{aligned}
&- \sum_{k=1}^{N_{el}}\oint_{\mathcal{S}_k}\left[\mathbf{M}\left(\varphi_i\frac{\partial\mathcal{C}_i(\xi,\eta)}{\partial\xi} + \frac{\partial\varphi}{\partial\xi}\Big|_i \frac{\partial\mathcal{D}_i^\xi(\xi,\eta)}{\partial\xi} + \frac{\partial\varphi}{\partial\eta}\Big|_i \frac{\partial\mathcal{D}_i^\eta(\xi,\eta)}{\partial\xi}\right)\right]J(\xi,\eta)d\mathcal{S}
\end{aligned}
$$

$$
\begin{aligned}
&- \sum_{k=1}^{N_{el}}\oint_{\mathcal{S}_k}\left[\mathbf{N}\left(\varphi_i\frac{\partial\mathcal{C}_i(\xi,\eta)}{\partial\eta} + \frac{\partial\varphi}{\partial\xi}\Big|_i \frac{\partial\mathcal{D}_i^\xi(\xi,\eta)}{\partial\eta} + \frac{\partial\varphi}{\partial\eta}\Big|_i \frac{\partial\mathcal{D}_i^\eta(\xi,\eta)}{\partial\eta}\right)\right]J(\xi,\eta)d\mathcal{S}
\end{aligned}
$$

where $J(\xi, \eta)$ is the Jacobian of the transformation in the system of coordinates ξ, η. Regrouping by the nodal values and the nodal derivatives, the previous equations become:

$$
\begin{aligned}
E(\mathbf{y})\varphi(\mathbf{y}) \; = \; & \sum_{k=1}^{N_{el}} \sum_{i=1}^{4} \chi_i \oint_{\mathcal{S}_k} \left(G \mathcal{C}_i(\xi, \eta) \right) J(\xi, \eta) d\mathcal{S} \\
& + \sum_{k=1}^{N_{el}} \sum_{i=1}^{4} \frac{\partial \chi}{\partial \xi} \Big|_i \oint_{\mathcal{S}_k} \left(G \mathcal{D}_i^{\xi}(\xi, \eta) \right) J(\xi, \eta) d\mathcal{S} \\
& + \sum_{k=1}^{N_{el}} \sum_{i=1}^{4} \frac{\partial \chi}{\partial \eta} \Big|_i \oint_{\mathcal{S}_k} \left(G \mathcal{D}_i^{\eta}(\xi, \eta) \right) J(\xi, \eta) d\mathcal{S} \\
& - \sum_{k=1}^{N_{el}} \sum_{i=1}^{4} \varphi_i \oint_{\mathcal{S}_k} \left(\frac{\partial G}{\partial n} \mathcal{C}_i(\xi, \eta) \right) J(\xi, \eta) d\mathcal{S} \\
& - \sum_{k=1}^{N_{el}} \sum_{i=1}^{4} \frac{\partial \varphi}{\partial \xi} \Big|_i \oint_{\mathcal{S}_k} \left(\frac{\partial G}{\partial n} \mathcal{D}_i^{\xi}(\xi, \eta) \right) J(\xi, \eta) d\mathcal{S} \\
& - \sum_{k=1}^{N_{el}} \sum_{i=1}^{4} \frac{\partial \varphi}{\partial \eta} \Big|_i \oint_{\mathcal{S}_k} \left(\frac{\partial G}{\partial n} \mathcal{D}_i^{\eta}(\xi, \eta) \right) J(\xi, \eta) d\mathcal{S} \quad \text{(E.14)}
\end{aligned}
$$

$$
\begin{aligned}
E(\mathbf{y})\frac{\partial \varphi(\mathbf{y})}{\partial \xi} \; = \; & \sum_{k=1}^{N_{el}} \sum_{i=1}^{4} \chi_i \oint_{\mathcal{S}_k} \left(-\frac{\partial G}{\partial \xi} \mathcal{C}_i(\xi, \eta) \right) J(\xi, \eta) d\mathcal{S} \quad \text{(E.15)} \\
& + \sum_{k=1}^{N_{el}} \sum_{i=1}^{4} \frac{\partial \chi}{\partial \xi} \Big|_i \oint_{\mathcal{S}_k} \left(-\frac{\partial G}{\partial \xi} \mathcal{D}_i^{\xi}(\xi, \eta) \right) J(\xi, \eta) d\mathcal{S} \\
& + \sum_{k=1}^{N_{el}} \sum_{i=1}^{4} \frac{\partial \chi}{\partial \eta} \Big|_i \oint_{\mathcal{S}_k} \left(-\frac{\partial G}{\partial \xi} \mathcal{D}_i^{\eta}(\xi, \eta) \right) J(\xi, \eta) d\mathcal{S} \\
& - \sum_{k=1}^{N_{el}} \sum_{i=1}^{4} \varphi_i \oint_{\mathcal{S}_k} \left(\mathbf{H} \frac{\partial \mathcal{C}_i(\xi, \eta)}{\partial \xi} + \mathbf{K} \frac{\partial \mathcal{C}_i(\xi, \eta)}{\partial \eta} \right) J(\xi, \eta) d\mathcal{S} \\
& - \sum_{k=1}^{N_{el}} \sum_{i=1}^{4} \frac{\partial \varphi}{\partial \xi} \Big|_i \oint_{\mathcal{S}_k} \left(\mathbf{H} \frac{\partial \mathcal{D}_i^{\xi}(\xi, \eta)}{\partial \xi} + \mathbf{K} \frac{\partial \mathcal{D}_i^{\xi}(\xi, \eta)}{\partial \eta} \right) J(\xi, \eta) d\mathcal{S} \\
& - \sum_{k=1}^{N_{el}} \sum_{i=1}^{4} \frac{\partial \varphi}{\partial \eta} \Big|_i \oint_{\mathcal{S}_k} \left(\mathbf{H} \frac{\partial \mathcal{D}_i^{\eta}(\xi, \eta)}{\partial \xi} + \mathbf{K} \frac{\partial \mathcal{D}_i^{\eta}(\xi, \eta)}{\partial \eta} \right) J(\xi, \eta) d\mathcal{S}
\end{aligned}
$$

$$
\begin{aligned}
E(\mathbf{y})\frac{\partial\varphi(\mathbf{y})}{\partial\eta} \;=\; & \sum_{k=1}^{N_{el}}\sum_{i=1}^{4}\chi_i\oint_{\mathcal{S}_k}\left(-\frac{\partial G}{\partial\eta}\mathcal{C}_i(\xi,\eta)\right)J(\xi,\eta)d\mathcal{S} && \text{(E.16)}\\
+ & \sum_{k=1}^{N_{el}}\sum_{i=1}^{4}\frac{\partial\chi}{\partial\xi}\Big|_i\oint_{\mathcal{S}_k}\left(-\frac{\partial G}{\partial\eta}\mathcal{D}_i^\xi(\xi,\eta)\right)J(\xi,\eta)d\mathcal{S}\\
+ & \sum_{k=1}^{N_{el}}\sum_{i=1}^{4}\frac{\partial\chi}{\partial\eta}\Big|_i\oint_{\mathcal{S}_k}\left(-\frac{\partial G}{\partial\eta}\mathcal{D}_i^\eta(\xi,\eta)\right)J(\xi,\eta)d\mathcal{S}\\
- & \sum_{k=1}^{N_{el}}\sum_{i=1}^{4}\varphi_i\oint_{\mathcal{S}_k}\left(\mathbf{M}\frac{\partial\mathcal{C}_i(\xi,\eta)}{\partial\xi}+\mathbf{N}\frac{\partial\mathcal{C}_i(\xi,\eta)}{\partial\eta}\right)J(\xi,\eta)d\mathcal{S}\\
- & \sum_{k=1}^{N_{el}}\sum_{i=1}^{4}\frac{\partial\varphi}{\partial\xi}\Big|_i\oint_{\mathcal{S}_k}\left(\mathbf{M}\frac{\partial\mathcal{D}_i^\xi(\xi,\eta)}{\partial\xi}+\mathbf{N}\frac{\partial\mathcal{D}_i^\xi(\xi,\eta)}{\partial\eta}\right)J(\xi,\eta)d\mathcal{S}\\
- & \sum_{k=1}^{N_{el}}\sum_{i=1}^{4}\frac{\partial\varphi}{\partial\eta}\Big|_i\oint_{\mathcal{S}_k}\left(\mathbf{M}\frac{\partial\mathcal{D}_i^\eta(\xi,\eta)}{\partial\xi}+\mathbf{N}\frac{\partial\mathcal{D}_i^\eta(\xi,\eta)}{\partial\eta}\right)J(\xi,\eta)d\mathcal{S}
\end{aligned}
$$

or, in matricial form:

$$
\frac{1}{2}\mathbf{I}\Phi = \mathbf{B}\Psi + \mathbf{C}\Phi \tag{E.17}
$$

where

$$
\Psi = \begin{bmatrix} \chi_i \\ \hline \frac{\partial\chi}{\partial\xi}\Big|_i \\ \hline \frac{\partial\chi}{\partial\eta}\Big|_i \end{bmatrix} \quad \Phi = \begin{bmatrix} \varphi_i \\ \hline \frac{\partial\varphi}{\partial\xi}\Big|_i \\ \hline \frac{\partial\varphi}{\partial\eta}\Big|_i \end{bmatrix} \tag{E.18}
$$

$$
\mathbf{B} = \begin{bmatrix} \mathbf{GC} & \mathbf{GD}^\xi & \mathbf{GD}^\eta \\ \hline \mathbf{G}_\xi\mathbf{C} & \mathbf{G}_\xi\mathbf{D}^\xi & \mathbf{G}_\xi\mathbf{D}^\eta \\ \hline \mathbf{G}_\eta\mathbf{C} & \mathbf{G}_\eta\mathbf{D}^\xi & \mathbf{G}_\eta\mathbf{D}^\eta \end{bmatrix} \tag{E.19}
$$

$$
\mathbf{C} = \begin{bmatrix} \mathbf{G_n C} & \mathbf{G_n D}^\xi & \mathbf{G_n D}^\eta \\ \hline \mathbf{HC}_\xi+\mathbf{KC}\eta & \mathbf{HD}_\xi^\xi+\mathbf{KD}_\eta^\xi & \mathbf{HKD}_\xi^\eta+\mathbf{KD}_\eta^\eta \\ \hline \mathbf{MC}_\xi+\mathbf{NC}\eta & \mathbf{MD}_\xi^\xi+\mathbf{ND}_\eta^\xi & \mathbf{MD}_\xi^\eta+\mathbf{ND}_\eta^\eta \end{bmatrix} \tag{E.20}
$$

List of Figures

List of Tables